Precipitates on Dislocations

Mathematical Modelling of Nucleating and Growing Precipitates on Dislocations

S.M. Vonk

Precipitates on Dislocations

Mathematical Modelling of Nucleating and Growing Precipitates on Dislocations

by

S.M. Vonk

A thesis submitted to the
Delft Institute of Applied Mathematics
at the faculty EEMCS of the TU Delft
in partial fulfilment of the requirements

for the degree

MASTER OF SCIENCE
in
APPLIED MATHEMATICS

in the specialisation of Computational Science and Engineering,
to be defended publicly on 15th September 2016.

Precipitates on Dislocations

Mathematical Modelling of Nucleating and Growing Precipitates on Dislocations

by

S.M. Vonk

Abstract: Many models for nucleating and growing precipitates have been developed. Each model with their own advantages and disadvantages. Only few of those models are made for heterogeneous nucleation (on dislocations) and most of them are based on the mean radius approach. In the literature study by Vonk (2016) one of these models (by Zurob et al. (2002)) was explained, analysed and tested for different values of the model parameters and different initial values. The model showed to be flexible, but still had some drawbacks, of which the mean radius aspect was the most limiting. A new distribution model is developed in this master thesis, based on the KWN model by Robson (2014) and Den Ouden et al. (2013). Even though the approach has changed, the nucleation and growth rate were adopted from the model by Zurob et al. (2002), which still included some drawbacks. Some of these drawbacks are eliminated by extending the model and some are recommended for future work. The two main drawbacks that were eliminated, were the lack of influence of all elements in the system and the competition between nucleation sites and different precipitate compositions. All elements in the system influence the nucleation and growth of the precipitates, even when the elements do not participate in the precipitate. A multi-component model is the extension to capture this complexity (Den Ouden et al. (2013)). Because most steel alloys contain many alloying elements, different precipitates can occur simultaneously (for instance, $Nb(C,N)$, AlN and MnS) and complex precipitates may exist, like $(Nb,Ti)(C,N)$. Also precipitates may nucleate at various nucleation sites. A multi-precipitate model is the extension to capture this complexity. The results of the simulations using the distribution model and its extensions are analysed and compared, showing the flexibility of the model. The implementation includes the multi-component and multi-precipitate extension, but no model for complex precipitates yet.

Keywords: Model by Zurob et al., precipitation, dislocations, grain boundaries, homogeneous, nucleation, growth, $NbCN$, AlN, MnS, distribution, KWN model, precipitate, backward euler.

Student number	4085299	
Project duration	December 7, 2015 - September 15, 2016	
Daily supervisors	Dr. ir. D. den Ouden	TU Delft
	Dr. W. Kranendonk	Tata Steel Europe IJmuiden
Thesis advisor	Dr. ir. F.J. Vermolen	TU Delft
Responsible professor	Prof.dr.ir. C. Vuik	TU Delft
Other thesis committee members	Dr. ir. W.T. van Horssen	TU Delft
	Dr. ir. S.E. Offerman	TU Delft

TU Delft Delft University of Technology TATA STEEL

Preface

This document is the result of my study carried out at the University of Technology at Delft, The Netherlands in cooperation with Tata Steel at IJmuiden, The Netherlands. This Master Thesis is done at the chair of Numerical Analysis, in partial fulfilment of the requirements for the degree Master of Science in Applied Mathematics.

I wish to sincerely thank all people involved in this project, with a special thanks to the people proposing and supervising the project. First, I would like to thank Dennis den Ouden, who has been there throughout the entire project, always available and willing to help out, sometimes leading to hours of discussing. Second, I would like to thank Winfried Kranendonk from Tata Steel, who has also been there throughout the whole project with his support. Especially his critical eye helped me to raise the project and report to a higher level. It was a tough job to understand and become an expert in a completely new working field, but Dennis and Winfried really helped me to through it, thank you for this, and remember:

'If you're not part of the solution, you're part of the precipitate.'

S.M. Vonk
September 15, 2016

Contents

List of Figures

List of Tables

List of Algorithms

1 Introduction

Precipitates play a very important role in the process of steel making and the final product steel. They can increase the strength of steel and decrease the growth of grains. Precipitation strengthening and small ferrite grains form the basis for the strength in High-Strength Low-Alloy (HSLA) steel, also named microalloying steels. This product group finds wide applications in the automotive, construction and energy (pipelines) industries. The main alloying elements for precipitates in HSLA steel are niobium, titanium and vanadium. Moreover, precipitation strengthening is also increasingly being used as an additional strengthening mechanism in Advanced High Strength Steels (AHSS). Controlling and optimization of precipitation for both the hot rolling process as well as the annealing process is, therefore, essential.

Experiments on precipitation kinetics are time consuming, laborious and demand very special equipment. Models which describe the precipitation kinetics are therefore an essential addition to the experimental tools. Such models should (and can) reduce the development time for new steel grades, support the solution of production problems, support the optimisation of processes and improve the design of experimental tests. It would therefore be profitable to develop and improve new and existing models for (niobium) precipitation in steel.

Precipitates can nucleate at different sites in steel: in grains, on grain boundaries, on dislocations, amongst others. The nucleation of precipitates in grains is called homogeneous nucleation, and the nucleation of precipitates on dislocations and other defects in the steel is called heterogeneous nucleation. Several models for the evolution of precipitates on different (nucleation) sites have been developed, but most of them return the mean diameter and the density of the precipitates. This is a reasonable approximation as long as the radius distribution is unimodal. Due to the complexity of the production process (i.e. multiple deformations) it is very difficult to make an assumption about the form of the radius distribution. It even might be multimodal under certain conditions. In that case, the mean radius approximation could return incorrect results and an explicit evolution description of the radius distribution is desirable.

Den Ouden et al. (2013) constructed a model with distributions for the diameter of the precipitates, but primarily for homogeneous nucleation. Since, heterogeneous nucleation seems to play a key role during plastic deformation of steel, which occurs, for example, during the hot rolling process, the goal of this Master Thesis is to make a new model with distributions for the radius of the precipitates, but now for heterogeneous nucleation.

To understand the process of nucleating and growing precipitates on dislocations, a model by Zurob et al. (2002) was implemented and analysed in Vonk (2016). This model is limited to the mean diameter and density of the precipitates and describes only niobiumcarbonitride precipitates, but it gives a good indication of how the precipitates nucleate and grow and also describes the interaction with recovery and recrystallisation (of dislocations). In this Master thesis the recommended improvements from Vonk (2016) are implemented and the results are compared to the results obtained using the model based on Zurob et al. (2002).

The thesis exists of two main parts. The first part includes the model description and background information of the problem. The model description is developed on the basis of Zurob's model. In Zurob's model, precipitation was only considered on dislocations, and, therefore, the first part of the theory will be explained for this type of precipitation. In Chapter 2 preliminaries of metallurgy are introduced, like information on thermodynamics, phase diagrams and Gibbs free energy, but also information on dislocations and metalworking techniques is given to fully understand the process of steel making and the processes where precipitation plays a big role. Using this knowledge, a mathematical model is introduced in Chapter 3 describing the nucleating and growing precipitates on dislocations. This mathematical model uses the distribution approach as described by Robson (2014) and Den Ouden et al. (2013).

This model mathematical model was extended with a multi-component version in Chapter 4. Multi-component, meaning that, all elements in the system are taken into account when describing the evolution of precipitates. After the development of the mathematical model for nucleation on dislocations, the model was extended to other nucleation sites in Chapter 5. The theory for the evolution of precipitates on these sites is similar to the one for precipitates on dislocations, and the extension of the model can be considered as a generalisation of Zurob's model. Furthermore in Chapter 5, the model is extended to a multi-precipitate version, meaning that, contrary to some models, multiple types of precipitates ($Nb(C,N)$, AlN, MnS, etc.) and multiple nucleation sites (dislocations, grain boundaries, grains, etc.) can be involved and analysed at the same time. Chapters 6 and 7 complete the first part with the numerical methods for finding a solution to the developed model and the computational issues that came along.

The second part of this thesis includes the simulation and numerical results and is structured as follows. In Chapter 8 the results of the simulation with the basic mathematical model from Chapter 3 are given and analysed. And in Chapters 9 and 10 the results of the simulation using the extensions from respectively Chapters 4 and 5 are given and analysed. The second part is completed with the conclusions in Chapter 11 and recommendations for future work in Chapter 12.

I

Model description

2

Preliminaries in metallurgy

To model the nucleating and growing of precipitates on dislocations, one needs some preliminaries in metallurgy. This chapter starts with an introduction to the crystal structure of metals. Thereafter a discussion is presented on thermodynamics and the phase diagram of steel. Then the diffusional concepts related to alloys are explained, followed by a short explanation of precipitation reactions and how their kinetics is determined by diffusion. These precipitation reactions can take place in two different ways: homogeneous and heterogeneous, which will be explained for the case of precipitation on dislocations. Finally the process of steel making is presented and it is shown where the precipitation reactions we focus on occur during this process. The information presented in this chapter mostly originates from Porter and Easterling (1981) (especially Chapters 1, 2 and 5). Also some of the information originates from Den Ouden (2015) and the more detailed information about dislocations comes from Hull and Bacon (2001).

2.1. Crystal Structure

Metals can have different crystal structures, of which the body-centred and face-centred cubic crystal structure (shown in Figure 2.1) are the most common.

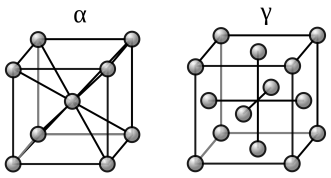

Figure 2.1: A part of a metal with a body-centred cubic (bcc) crystal structure (left) and a face-centred cubic (fcc) crystal structure (right). Image from Wikipedia (2016c).

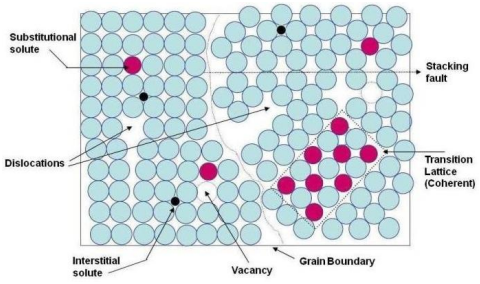

Figure 2.2: Crystal structure with several different defects.
Image from Shah (2012).

When a metal solidifies from the liquid state, such crystals start to grow in the metal. The longer the metal takes to cool the larger the crystals grow in the metal. These crystals form the grains in the solid metal. Each grain is a distinct crystal with its own orientation. The areas between the grains are known as grain boundaries and are illustrated in Figure 2.2 (cross-section of the grains).

2.2. Thermodynamics and Phase Diagrams

To understand the concept of steel making and the process that takes place during the nucleating and growing of precipitates in steel, we first need to understand the thermodynamics of these processes. The keywords during this process are 'free energy' and 'equilibrium'. However, for this we need four important definitions to start with:

Definition 2.1. *A **phase** is a region of space where the physical properties and composition are homogeneous and which is physically distinct from other parts of the system.*

Definition 2.2. *A **system** is an alloy that can exist as one phase or a mixture of phases.*

Definition 2.3. *A **component of the system** is one of the different elements or chemical compounds that make up the system.*

A system can have two types of thermodynamic properties:

1. Intensive properties, which are independent of size of the system, like the absolute temperature (T) and the pressure (P).
2. Extensive properties, which are directly proportional to the quantity of material in the system (number of moles in the system), like volume (V), internal energy (E), enthalpy (H), entropy (S) and free energy (G).

Definition 2.4. *A **phase transformation** is how one or more phases in an alloy (a system) change into a new phase or mixture of phases.*

In phase transformations we are always concerned with changes towards thermodynamic equilibrium, where we mean equilibrium in the sense of the lowest free energy. For phase transformations that occur at constant temperature and pressure, the relative stability of a system is determined by its Gibbs free energy (G), measured in Joules (J), and defined by

$$G = H - TS,$$

where H is the enthalpy, T the absolute temperature in Kelvin (K) and S the entropy of the system. The enthalpy H is the sum of the internal energy E and the mechanical energy PV:

$$H = E + PV,$$

where E is the internal energy of the system in Joules (J), both kinetic and potential, P is the pressure in the system in Joules per cubic meter (J/m^3) and V is the volume of the system in cubic meters (m^3). It is good to notice, that in condensed phases like solid and liquid, the value of PV is much smaller than the internal energy E and the heat content of the system H is therefore close to this internal energy. When we plot the Gibbs free energy for a spontaneous change in the state of a system (with constant T and P), we get a graph like in Figure 2.3.

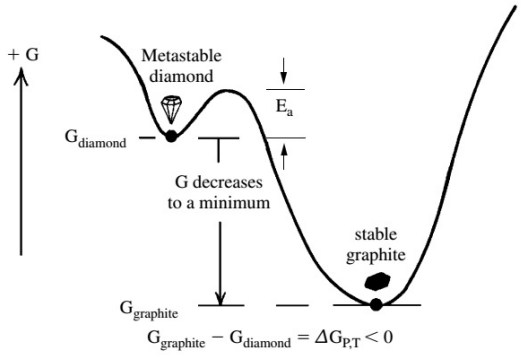

Figure 2.3: Illustration of a spontaneous change in the state of a system and the associated states. Image from Learning Geology (2015).

The driving force behind a phase transformation is the difference between the Gibbs free energy in a certain (non-)equilibrium state of the system and the equilibrium state, where the state is in equilibrium when the free energy of the system is at minimum, i.e.:

$$dG = 0.$$

The intermediate states $dG \neq 0$ are unstable. From mathematics we know that when $dG = 0$, we have found a minimum or maximum, however we are only interested in the minimum free energy. Also, we can have

a purely local minimum or a global minimum, which correspond to a metastable or a stable equilibrium respectively. Given time, systems in a metastable state will transform to a stable state. However, the system then first has to overcome the energy maximum between the metastable and stable state, which is called the activation energy (Figure 2.3: E_a) and this energy barrier will determine the rate of the transformation.
Using the Gibbs free energy plots for different temperatures, a phase diagram for alloys can be constructed. This derivation will not be given in this literature study, but an example can be found in Porter and Easterling (1981).

Since the focus of this thesis will be on steel, the phase diagram for iron-carbon is given in Figure 2.4. In this figure different phases of the system are shown for different temperatures (vertical axis) and different weight percentages of carbon (horizontal)[1]. Examples of these phases are Austenite and Ferrite, which also correspond to a crystal structure as described in Section 2.1 (Austenite $\leftrightarrow \gamma \leftrightarrow$ fcc, Ferrite $\leftrightarrow \alpha \leftrightarrow$ bcc). However, the probability that one has a system that is in such an equilibrium state is small. For a system to reach such a state or for us to model it, we need to introduce the concept of diffusion. Some of these phase transformations are not diffusion driven, but during this thesis we will only focus on diffusional phase transformations.

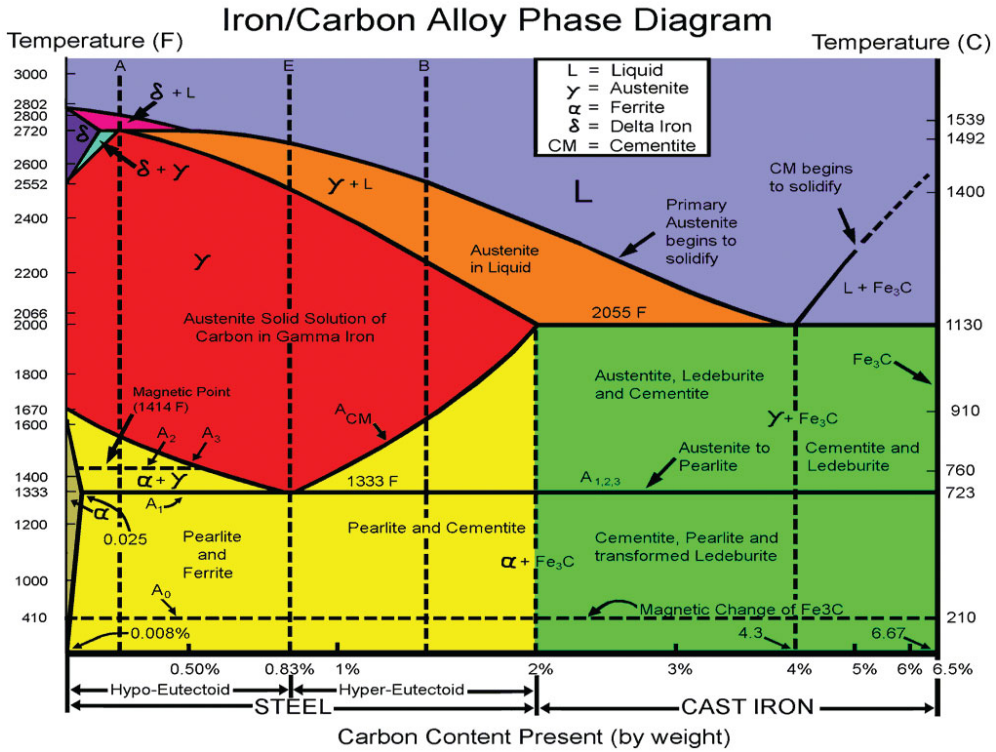

Figure 2.4: Phase diagram of iron-carbon (steel). Image from Nair (2015).

2.3. Diffusion

The concept of diffusion is based on the principle of the system wanting to reach the state with the lowest Gibbs free energy. Diffusion is basically the random movement of atoms. Two types of diffusion can be distinguished: interstitial and substitutional diffusion. For this we need to understand the concept of interstitial and substitutional atoms. Interstitial atoms are significantly smaller than the atoms of the solvent, and can thereby move between the solvent atoms. Substitutional atoms are larger or of approximate equal size as the solvent atoms and can thereby not move between the solvent atoms, but need vacancies to move around. Both types of atoms are shown in Figure 2.5. Since the interstitial atoms are smaller, they force their way between the solvent atoms, as shown in Figure 2.5a. This is called interstitial diffusion. The movement of substitutional atoms is called substitutional diffusion and is illustrated in Figure 2.5b. Here a solute or solvent atom will move to a vacant place in the solvent matrix. In this case a solute or solvent atom and a vacancy

[1] Some phase diagrams use a weight or molar fraction to measure the composition of the system.

will interchange in position. Since substitutional diffusion needs vacancies which only appear in small numbers, whereas interstitial diffusion occurs without vacancies, substitutional diffusion rates are much lower than interstitial diffusion rates in general.
For both types of diffusion we can assume that Fick's second law can be used to model how diffusion causes the concentration to change with time:

$$\frac{\partial C}{\partial t} = \nabla \cdot (D \nabla C),$$

where C is the concentration of the solute atoms and D the diffusion constant of the solute atoms in m^2/s. If the diffusion constant has no variations with concentration of space, we find

$$\frac{\partial C}{\partial t} = D \Delta C.$$

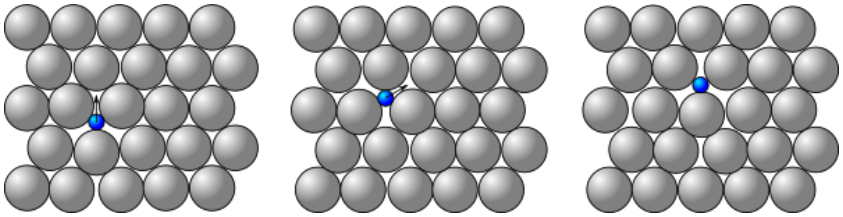

(a) Illustration of interstitial diffusion.

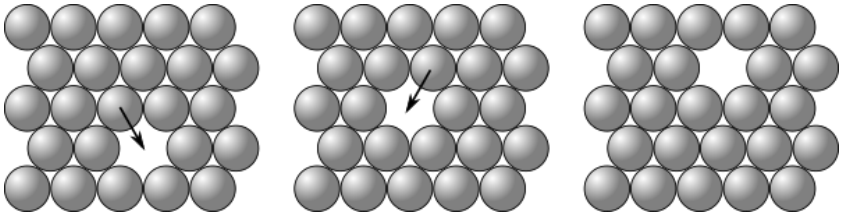

(b) Illustration of substitutional diffusion.

Figure 2.5: Different types of diffusion. Images from Cdan (2015).

2.4. Precipitation

In multi-component systems, like steel, many different phases can occur, which depends on the temperature. Five types of phase transformations can occur between different phases, of which almost all of them take place by diffusional nucleation and growth. However, we are primarily interested in the phase transformation due to precipitation reactions, which can be described by

$$\alpha \rightarrow \alpha^* + \beta,$$

where α is the phase before the transformation, and α^* and β are the phases after the transformation. When starting with a system in a supersaturated metastable solid phase α and a precipitation reaction occurs, the resulting system will consist of the α^* and β phases. Here α^* is a solid phase with lower Gibbs energy than α but with the same crystal structure and β is a (meta)stable precipitate phase. Looking back at the phase diagram in Figure 2.4, an example of this could be the phase transformation from austenite to austenite with ferrite ($\gamma \rightarrow \gamma + \alpha$).

The evolution of precipitation can be divided in three general stages:

1. Nucleation: the appearance of precipitates from a supersaturated matrix.

2. Growth: the growing of precipitates. During this process the precipitates take atoms from the matrix to grow until equilibrium between the precipitates and the matrix has been reached. The concentrations of the precipitate-forming solutes will significantly decrease in the matrix.

3. Coarsening: the growth of large precipitates at the expense of small precipitates, also known as Ostwald ripening. At this stage the concentrations of the precipitate-forming solute atoms will remain almost constant in the matrix. The driving force for coarsening is the reduction of the interfacial energy and thereby the total free energy. By the growth of large precipitates and the disappearance of small ones the total interfacial area is reduced, which reduces the free energy. This mostly happens if the concentrations (of the precipitates compounds) in the matrix are near the equilibrium concentration.

A fourth stage, (partial) dissolving, happens only in special occasions, for example when the volume fraction of the precipitate increases above the equilibrium volume fraction. Some of these stages can take place at the same time (for example nucleation and growth), so for the final model we also need the interaction between these four stages.

2.5. Dislocations

The precipitation reaction, as described before, takes place by nucleation and growth. Two types of nucleation can take place, namely homogeneous and heterogeneous (on defects) nucleation. The different types of heterogeneous nucleation (on dislocations, on grain boundaries, on other precipitates and inclusions, etc.) have lower activation energies than homogeneous nucleation, and, therefore, heterogeneous nucleation is the main mechanism in solids and liquids. Therefore we will focus on heterogeneous nucleation in this thesis.

As described in Section 2.1, metal alloys have a crystal structure, however, all real crystals contain some sort of imperfections which can have different shapes: point, line, surface or volume defects. These defects locally disturb the arrangement of the atoms in the crystal structure and in this way have an important effect on the properties of the metal alloys. These defects are the locations for heterogeneous nucleation. Some of the defects like vacancies, dislocations, stacking faults and grain boundaries are shown in Figure 2.2. In this thesis, the main focus will be on the nucleation and growth of precipitates on dislocations.

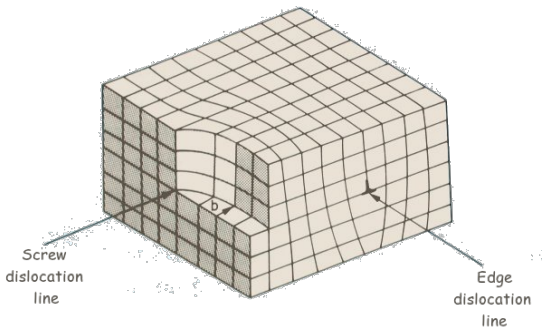

Figure 2.6: Combination of two types of dislocations.
Image from Rey (2015).

All these defects increase the free energy of the material, which is an unwanted effect. Each defect has his own type of free energy contribution, for example a dislocation is associated with an increased elastic energy and a grain boundary with an increased interface energy. The combination of a precipitate and the defect results in a lower free energy (for a dislocation a lower elastic energy) and thereby reducing the total free energy of the material. The equation for the energy change due to a heterogeneous reaction therefore becomes

$$\Delta G = V\Delta g_v + A\gamma + \Delta G_{dis}, \tag{2.1}$$

where Δg_v is the chemical free energy, $A\gamma$ the increase of free energy due to interfacial energy [1] and ΔG_{dis} the free energy release due to the reduction of the elastic energy associated with precipitation on dislocations. The sign of Δg_v is dependent on the saturation of the matrix. It has a negative sign for an over-saturated matrix and a positive sign for an under-saturated matrix. Further, we will assume in this thesis, that we deal with incoherent particles and any misfit strain energy can be approximated by zero.

[1] The creation of a nucleus with area A will give a free energy increase of $A\gamma$, assuming that the α-β interfacial energy is isotropic.

To fully understand the energy changes due to nucleation on dislocations, we need more information about dislocations and their geometry. Starting with the existing types of dislocations, Figure 2.6 shows both of them:

1. An edge dislocation, *and*
2. a screw dislocation.

The edge dislocation can be simulated as follows: separate a crystal in two parts, along one of the lattice planes, such that that the faces of the crystal are separated. Now an additional half-plane of atoms can be inserted in this opening, which results in an edge dislocation. Both positive and negative edge dislocations can exist, respectively meaning an additional half-plane from above the broken surface, illustrated with a '$\perp$' or an additional half-plane from below the broken surface, illustrated with a '$\top$'. It is good to point out, that after an edge dislocation has formed, edge dislocations can move to the side of the crystal under a shearing deformation of the crystal, as shown in Figure 2.7.

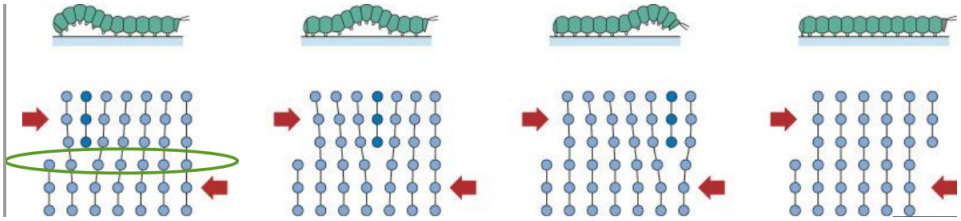

Figure 2.7: Illustration of the movement of an edge dislocation.
Image from Academic Resource Center (2015).

The screw dislocation can be seen as a simple displacement of part of the crystal structure, relative to the other part of the crystal structure. As with edge dislocations, two directions of the dislocation can be distinguished. Contrary to the edge dislocations, however, screw dislocations are distinguished between left-handed and right-handed, meaning the direction of the dislocation when looking down the dislocation line. When a clockwise circuit is made round it, it is referred to as a right-handed screw dislocation and when a counter-clockwise circuit is made round it, it is referred to as a left-handed screw dislocation. Mixtures of both edge and screw dislocations also exist, as shown in Figure 2.6. To formally describe the dislocation, we introduce the definition of the *Burgers circuit*.

Definition 2.5. *The **Burgers circuit** is any atom-to-atom path, a closed loop, containing the dislocations in the crystal structure (Figure 2.8).*

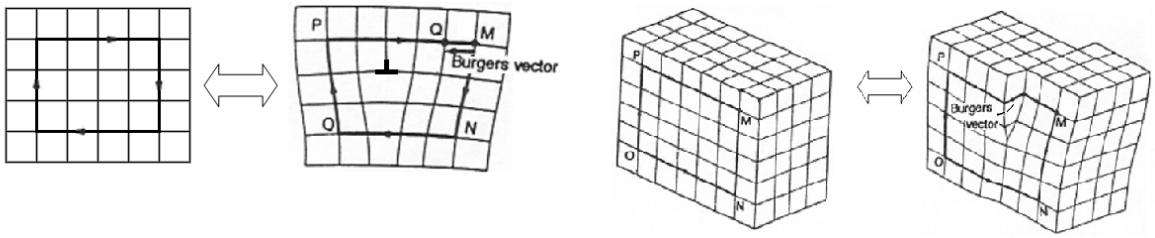

Figure 2.8: Illustration of the Burgers vector for both type of dislocations. Left we see the edge dislocation and right the screw dislocation. Image from Wikipedia (2016a).

Another important concept is that of the *Burgers vector*, which together with the Burgers circuit defines the dislocation. The Burgers vector's magnitude and direction is best understood when the dislocation-bearing crystal structure is first visualised without the dislocation, that is, the perfect crystal structure. For this we use Figure 2.8 as an illustration. In this perfect crystal structure, a rectangle is drawn surrounding the site of the original dislocation's origin. The lengths and widths of this rectangle are integer multiples of the unit-cell-edge length. Once the surrounding rectangle (*MNOP*) is drawn, the dislocation can be introduced. This dislocation will have the effect of deforming, not only the perfect crystal structure, but the rectangle as well.

The *MNOP*-rectangle could have one of its sides disjointed from the perpendicular side, severing the connection of the length and width line segments of the rectangle at one of the rectangle's corners, and displacing each line segment from each other. What was once a rectangle before the dislocation was introduced, is now an open geometric figure whose opening defines the direction and magnitude of the Burgers vector.

The Burgers vector is closely related to the dislocation density, since the dislocation density is defined as the total length of dislocation line per unit volume of crystal. It is a parameter of interest, since it influences both the nucleation and growth of precipitates on dislocations.

2.6. Metalworking Techniques

In the process of steel making, a series of metalworking techniques is used wherein precipitation reactions play a role. The process will be explained in general and the parts which include these precipitation reactions will be explained more thoroughly.

1. Reduction of iron oxides (ore) to iron metal

   - Installation/process: blast furnace (around 2000 °C),
   - Metallurgical processes: reduction reactions.

   The process of steel making starts with iron ore. This represents a chemical composition consisting of iron oxides (Fe_xO_y). At high temperatures the carbon level in these oxides is reduced, resulting in pig iron (liquid iron, containing around 4.4 wt% carbon) and CO_2.

2. Lowering of carbon concentration and adding alloying elements

   - Installation/process: basic oxygen steel plant (1550 °C),
   - Metallurgical processes: oxidation, dissolution (of alloying elements).

   The pig iron is transported to a steel mill, at which the carbon level in the iron is reduced. When the pig iron arrives at the steel mill it is carbon-rich (around 4.4 wt-%), but for the pig iron to be called steel, it has to be carbon-low (less than 2 wt-% carbon). To reduce the carbon in the mixture, we use the following reaction

   $$C + O_2 \rightarrow CO_2.$$

   In Figure 2.9 the process of blowing oxygen into the pig iron to get the reaction, is illustrated. During this process also several alloying elements like Ti (Titanium), Nb (Niobium) or V (Vanadium) are added, to change the mechanical properties of the resulting steel. This is an important part to point out, since especially these allloying elements are the ones that will form precipitates later on in the process. The result of the so called *Basic oxygen steelmaking* (Wikipedia (2015c)) are then cast into big slabs of around 230 mm thick and 10-20 ton. The structure of the resulting strips has large grains and can already contain precipitates.

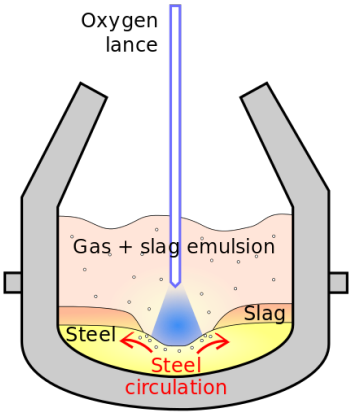

Figure 2.9: Principle of a LD (Linz-Donawitz) converter. Image from Wikipedia (2016e).

3. Rolling of strip from 230 mm to 2-25 mm

   - Installation/process: hot strip mill (850-1250 °C),
   - Metallurgical processes: deformation, recrystallisation, recovery, **precipitation**, transformation (oxidation).

   The thick slabs will then arrive at the hot strip mill, where the slabs are heated to 1100-1250 °C and rolled in a roughing and finishing mill to the final thickness between 2 and 25 mm. The deforming of the steel is an application of elastic and/or inelastic deformation and can therefore be described with a stress-strain relation.

   Between the rolls, recrystallisation and recovery can take place. Recrystallisation is the process of reducing dislocations (created by plastic deformation) by nucleation and growing of new, dislocation free, grains whereas recovery is reducing the dislocation density by annihilation and redistribution. An illustration of part of this process is shown in Figure 2.10. The last process of hot rolling, transformation, is the process where the steel transforms from the austenite to the ferrite phase, and takes place at the end of the hot strip rolling, when the strip is cooled down to around 600-700 °C.

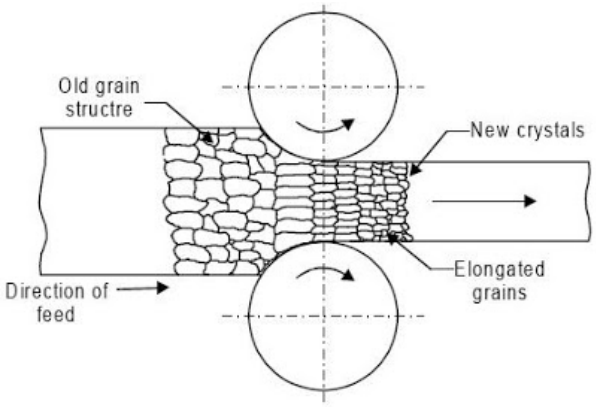

Figure 2.10: Illustration of the hot rolling and the processes that take place during this process. Image from Rendy Yusman (2011).

4. Rolling of strip from 2-25 mm to 0.2-1.5 mm (optional)

   - Installation/process: cold strip mill and annealing line (20-150 °C),
   - Metallurgical processes: deformation (cold strip mill), recrystallisation, recovery, **precipitation**, transformation (annealing line).

   The goal of this part of the process is to control the shape, size and thickness of the steel. The thickness is reduced by cold rolling, which results in a hard and difficultly deformable strip. To recover the formability again, the rolled strip is annealed (600-750°C) where recovery, recrystallisation, precipitation and, depending on the temperature, transformation will take place. Contrary to the metallurgical process that took place at the hot strip mill, this process mainly takes place in the ferrite phase instead of the austenite phase.

5. Coating and painting (optional)

   - Installation: coating and painting line,
   - Metallurgical processes: tempering (coating), hydrogen embrittlement (coating).

   This part of the steel making process only concerns the protection and/or outlook of the strip and is not relevant for the subject of this thesis.

3

KWN model

In Vonk (2016) the precipitation model by Zurob et al. (2002) was implemented and analysed. The model distinguishes two stages in the precipitation process: in the first stage precipitates nucleate and grow, while the total volume fraction increases, whereas, in the second stage, named coarsening, the volume fraction remains almost constant and large precipitates grow at the cost of small precipitates. A coarsening function is used to describe the switch between the two stages. Even though the results we found using this precipitation model seemed to be realistic and predicted the experimental data quite well after fitting, for applications to modern steel grades like the simulation of the production process of HSLA steels, the assumptions in the Zurob model needed a number of improvements and extensions:

- Because most steel alloys contain many alloying elements, different precipitates can occur simultaneously (for instance, $Nb(C,N)$[1], AlN and MnS) and complex precipitates may exist, like $(Nb,Ti)(C,N)$. Also precipitates may nucleate at various nucleation sites. However, in the Zurob model, only one type of precipitate is considered at the time. To correctly simulate the nucleation and growth of precipitates it is necessary to extend the precipitate evolution model in three different ways:

  1. All elements in the system influence the nucleation and growth of the precipitates, even when the elements do not participate in the precipitate. The growth rate for example is influenced by the diffusion coefficients and concentrations of all elements in the system. A multi-component model is the extension to capture this complexity (Den Ouden et al. (2013)).
  2. Describing more than one type of precipitate simultaneously (for instance $Nb(C,N)$, AlN and MnS), and at different nucleation sites (for instance grain boundaries, dislocations and on grains), which we call the multi-precipitate model.
  3. Complex precipitates may exist, like $(Nb,Ti)(C,N)$. The model should be capable of dealing with complex precipitates in a general matter, but the thermodynamical models belonging to individual complex precipitates will not be implemented, except for the $NbCN$ precipitate, since it was used in the models by Zurob et al. (2002), Kranendonk (2005) and Vonk (2016) as well. Thermodynamic models for other complex precipitates are a nice extension for further work.

- The evolution of precipitates in the Zurob model is based on the mean radius approximation. This is a reasonable approximation as long as the radius distribution is unimodal. Due to the complexity of the production process (i.e. multiple deformations) it is very difficult to make an assumption about the form of the radius distribution. It even might be multimodal under certain conditions. In that case, the mean radius approximation could return incorrect results and an explicit evolution description of the distribution is desirable. We therefore develop a model using distributions for the radius of the precipitates (for homogeneous nucleation such an implementation has already been given by Den Ouden et al. (2013)). This model will incorporate the extensions of the precipitate evolution model described above and is described for austenite simulations.

[1] In this thesis abbreviated by $NbCN$.

Taking these considerations into account, the following steps are performed in this thesis:

C.1 Make a new model, based on the approximations in the nucleation rate made by Zurob et al. (2002), in which the evolution of the mean radius will be replaced by the distributions of the radii. (Chapter 3)

C.2 Extend the new model with a multi-component version. (Chapter 4)

C.3 Extend the new model with a multi-precipitate version, meaning multiple precipitates with varying composition and nucleation at multiple nucleation sites. (Chapter 5)

In this chapter a new model with distributions is introduced for alloys with one type of precipitate. For this we choose the $NbCN$ precipitate, since this type of precipitate was also used in the model by Zurob et al. (2002). To accomplish the first step (item C.1), we start by introducing a new model: the KWN (Kampmann and Wagner (1991)) model in the form as used by Robson (2014). This model describes the evolution of the distribution during nucleation, growth and coarsening of precipitates. For this we introduce a function $\phi(R,t)$ which denotes the number density distribution of precipitates with radius R and at time t. Based on the KWN model, but using the approximations for the nucleation and growth rate from Zurob et al. (2002), we construct a model which includes this function $\phi(R,t)$. The main physical features of the KWN model are:

- All particles are spherical and classified by their radii in meters (m).
- The time evolution in seconds (s) of the model is described by the partial differential equation

$$\frac{\partial \phi}{\partial t} = -\frac{\partial [v\phi]}{\partial R} + S, \tag{3.1}$$

  in which $\phi \equiv \phi(R,t)$ in m^{-4} denotes the number density distribution of precipitates with radius R and at time t. Note that this is not a probability density function and will not always integrate to one, but to the precipitate number density at time t. $v \equiv v(R,t)$ in ms^{-1} represents the growth rate of precipitates with radius R and at time t and $S \equiv S(R,t)$ in $\mathrm{m}^{-4}\mathrm{s}^{-1}$ is a source function representing nucleation for the number density distribution of newly appearing precipitates with radius R at time t. By using this formulation of the evolution of the distribution of the precipitate radius, coarsening is implicitly incorporated and therefore no coarsening function is needed.
- The value of the source function S is based on the nucleation rate and a function indicating the radius at which nucleation takes place. The source function is given by (Den Ouden et al. (2013))

$$S(R,t) = I(t)\delta(R - R^*(t)), \tag{3.2}$$

  in which $I(t)$ denotes the nucleation rate of the precipitates following from Zurob et al. (2002) and Vonk (2016) and will be explained later on. $R^*(t)$ is the critical radius following from Vonk (2016) and δ is the Dirac delta function.

3.1. Nucleation

Following Vonk (2016), we assume that the time-dependent nucleation rate $I(t)$ for precipitates, as used in Equation (3.2), is given by

$$I(t) = (N_{total} - N) Z \beta^* \exp\left(\frac{-\Delta G^*}{k_B T}\right), \tag{3.3}$$

with the following properties:

- $(N_{total} - N)$ is the number of nucleation sites that is currently available. In this equation N_{total} is the total number of nucleation sites that is available and is approximated by

$$N_{total} = \frac{F\rho}{b}, \tag{3.4}$$

  where b is the length of the Burgers vector, F a fitting parameter and ρ the dislocation density. $N(t)$ is the precipitate number density and can be retrieved from the number density distribution ϕ using

$$N(t) = \int_0^\infty \phi(R,t)\, dR. \tag{3.5}$$

The precipitate mean radius $\bar{R}(t)$ can be retrieved in a similar fashion. We use the bar over the R to emphasise we refer to the mean radius at time t.

$$\bar{R}(t) = \frac{1}{N(t)} \int_0^\infty R\phi(R,t)dR, \tag{3.6}$$

- ΔG^* is the free energy barrier needed for the nucleation to take place, also known as the activation energy and will be explained later. The term $\exp\left(\frac{-\Delta G^*}{k_B T}\right)$ is thereby the probability that a nucleus with critical size will appear.
- Z is the Zeldovich non-equilibrium factor and β^* is the rate of atomic attachment to the critical nucleus. The Zeldovich factor describes the probability that a nucleus of critical size (at the maximum of the energy barrier) will continue to grow and not dissolve. β^* is the rate at which elements attach to the nucleus causing it to grow, giving an indication of the rate of nucleation. Due to the assumption that the precipitates are spherical, the approximation for $Z\beta^*$ (for $NbCN$ precipitates) is given by (Zurob et al. (2002))

$$Z\beta^* \approx \frac{D_{pipe,Nb} x^M_{Nb}}{a^2}, \tag{3.7}$$

  where $D_{pipe,Nb}$ is the diffusion coefficient of niobium along the dislocation (since it is the slowest diffusing element and hence assumed rate-determining), x^M_{Nb} the molar fraction of niobium in the matrix and a the matrix lattice constant.
- k_B is the Boltzman constant and T is the temperature given in K.

Combining the approximations given above, we find the following time-dependent nucleation rate $I(t)$:

$$I(t) = (N_{total} - N)\left(\frac{D_{pipe,Nb} x^M_{Nb}}{a^2}\right)\exp\left(\frac{-\Delta G^*}{k_B T}\right) \tag{3.8}$$

The activation energy ΔG^*, found in the nucleation rate (Equation (3.8)), and the associated critical radius R^*, used in the source function (Equation (3.2)), are estimated from the expression for the free energy of precipitate formation (Equation (2.1)):

$$\Delta G = V\Delta g_v + A\gamma + \Delta G_{dis}. \tag{2.1}$$

where V and A are respectively the volume and the area of the precipitate, Δg_v is the chemical free energy, also known as the chemical driving force, γ the interface energy, and ΔG_{dis} the free energy release due to the reduction of the elastic energy associated with precipitation on dislocations.
The chemical driving force in the energy balance for heterogeneous nucleation is estimated by

$$\Delta g_v = -\frac{k_B T}{v_{NbCN}} \ln\left(\frac{\text{matrix product}}{\text{solubility product}}\right) := -\frac{R_g T}{v_{m,NbCN}} \ln(\text{saturation}). \tag{3.9}$$

The matrix product is the product of the concentrations (in weight percentages) of the precipitate compounds in the matrix to the power of their stoichiometric ratio x (the ratio of carbon and nitrogen in the precipitate at equilibrium)

$$\text{matrix product} = wt\%Nb^M (wt\%C^M)^x (wt\%N^M)^{1-x}, \tag{3.10}$$

and the solubility product of the complex precipitate (meaning that it can be considered as a mixture of two (or) more precipitates, which consists of two elements) is related to the separate solubility products via (Hudd et al. (1971))

$$K(NbCN) = K(NbC)^x K(NbN)^{1-x} x^x (1-x)^{1-x}, \tag{3.11}$$

$$= \left(\frac{wt\%Nb^{Eq} wt\%C^{Eq}}{x}\right)^x \left(\frac{wt\%Nb^{Eq} wt\%N^{Eq}}{1-x}\right)^{1-x} x^x (1-x)^{1-x}, \tag{3.12}$$

$$= wt\%Nb^{Eq} (wt\%C^{Eq})^x (wt\%N^{Eq})^{1-x}. \tag{3.13}$$

The saturation is the quotient of the matrix product and the solubility product, and can be rewritten as

$$\text{saturation} = \frac{wt\%Nb^M}{wt\%Nb^{Eq}} \left(\frac{wt\%C^M}{wt\%C^{Eq}} \right)^x \left(\frac{wt\%N^M}{wt\%N^{Eq}} \right)^{1-x}. \tag{3.14}$$

Therefore, the saturation gives an indication of how close the matrix concentrations are to their equilibrium concentration. Under isothermal conditions the system will move to a state of equilibrium and, thus, the saturation will tend to one.
The equilibrium concentration in the matrix $wt\%Nb^{Eq}$ can be found by solving the following equation from Hudd et al. (1971):

$$\begin{aligned}
&(wt\%Nb^{Eq})^4(M_C M_N) + (wt\%Nb^{Eq})^3(-2wt\%NbM_C M_N + wt\%CM_N M_{Nb} + wt\%NM_C M_{Nb}) \\
&+ (wt\%Nb^{Eq})^2(-M_{Nb}M_N * K(NbC) - M_{Nb}M_C K(NbN) + (wt\%Nb)^2 M_C M_N - wt\%Cwt\%NbM_N M_N b \\
&- wt\%Nwt\%NbM_C M_{Nb}) + wt\%Nb^{Eq}(wt\%NbM_{Nb}M_N K(NbC) + K(NbN)wt\%NbM_C M_{Nb} \\
&- wt\%NK(NbC)M_{Nb}^2 - wt\%CK(NbN)M_{Nb}^2) + K(NbC)K(NbN)M_{Nb}^2 = 0,
\end{aligned} \tag{3.15}$$

where the solubility products $K(NbN)$ and $K(NbC)$ are temperature dependent, and the initial weight percentages for Nb, C and N are used. The solvus temperature T_{sol}, the maximum temperature at which precipitates can form, is found by substituting $wt\%Nb^0$ for $wt\%Nb^{Eq}$ in Equation (3.15) and solving for the temperature.
The free energy release due to the reduction of the elastic energy associated with dislocations used in Equation (2.1) is defined as (Zurob et al. (2002))

$$\Delta G_{dis} = -\frac{\mu b^2 R \ln(R/b)}{2\pi(1-\nu)} - \frac{\mu b^2 R}{5}, \tag{3.16}$$

leading to the energy balance for nucleation on dislocations:

$$\Delta G = V\Delta g_v + A\gamma - \frac{\mu b^2 R \ln(R/b)}{2\pi(1-\nu)} - \frac{\mu b^2 R}{5}, \tag{3.17}$$

where ν is the Poisson ratio and μ the shear modulus. A schematic representation of the energy changes of precipitate forming as a function of the precipitate radius (Equation (3.17)) is given in Figure 3.1, where it can be seen that the activation energy ΔG^* is the maximum of ΔG.

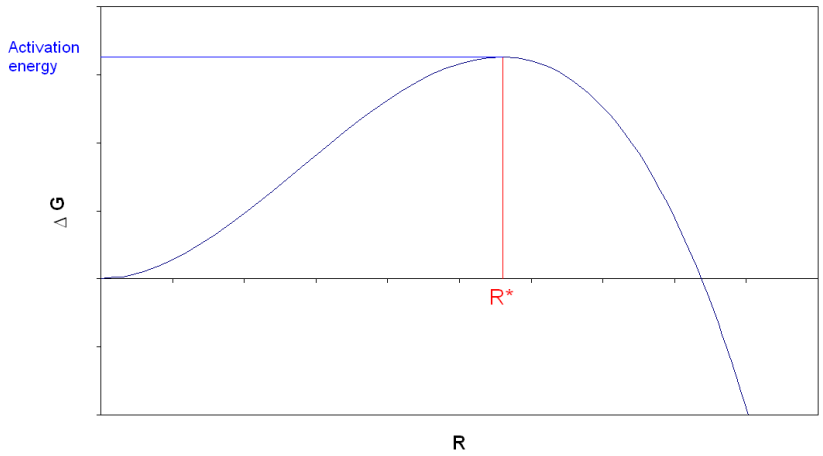

Figure 3.1: Schematic representation of the energy changes ΔG. Image from Perez et al. (2008).

We take the derivative of ΔG with respect to R, given in Equation (3.18) (note that Δg_v and γ do not depend on R), and set it equal to zero to find the critical radius (associated with the maximum of ΔG), where after we substitute the radius back into Equation (3.17) to find the activation energy ΔG^*.

$$\frac{d(\Delta G)}{dR} = 4\pi R^2 \Delta g_v + 8\pi R\gamma - \frac{\mu b^2}{2\pi(1-\nu)}(\ln(R/b)+1) - \frac{\mu b^2}{5} = 0 \tag{3.18}$$

Since, this equation is nonlinear and a (simple) analytic solution is not available, we solve it using a numerical method. The function can be easily differentiated, which makes Newton's method suitable for this problem. As an initial value we use the critical radius for homogeneous nucleation $\frac{-2\gamma}{\Delta g_v}$ (Den Ouden et al. (2013)).

3.2. Growth

In the previous section the nucleation rate $I(t)$, incorporated in the source function $S(R,t)$ was discussed. The growth rate v, as used in the calculation of the precipitate distribution ϕ is approximated by (Vonk (2016))

$$v(\phi,R,t)=\frac{dR}{dt}=\frac{D_{eff,X}}{R}\frac{C_X^M-C_X^R}{C_X^P-C_X^R}, \tag{3.19}$$

where the concentrations C and effective diffusion coefficient refer to the elements in the precipitate (Nb, C, N). The growth rate is directly dependent on R and indirectly dependent on ϕ through the concentrations. The effective diffusion coefficient D_{eff} for precipitates on dislocations is defined by

$$D_{eff,X}=D_{pipe,X}\pi b^2\rho+D_{bulk,X}(1-\pi b^2\rho), \tag{3.20}$$

where the dislocation density ρ is taken constant for now and D_{pipe} and D_{bulk} are respectively the diffusion coefficients in the dislocation and bulk. Because the diffusion coefficient of Nb is orders of magnitude smaller than of C and N, Nb will determine the growth rate of the precipitates. C^M is the concentration of the growth determining solute in the matrix, C^P the concentration of this solute in the precipitate and C^R the concentration of this solute in the matrix at the precipitate/matrix interface.

To calculate the concentration at the precipitate/matrix interface, we start with the growth rate (Equation (3.19)) for each element X (Nb, N and C) separately:

$$v=\frac{D_{eff,X}}{R}\frac{C_X^M-C_X^R}{C_X^P-C_X^R}\quad\Rightarrow\quad C_X^R=\frac{D_{eff,X}C_X^M-vRC_X^P}{D_{eff,X}-vR}. \tag{3.21}$$

This results in three equations (for Nb, N and C) with four unknowns: v, C_{Nb}^R, C_N^R and C_C^R, for which no unique solution is found. To find a fourth equation, we start from Equation (3.18) and rewrite it:

$$\Delta g_v=-\frac{2\gamma}{R}+\frac{\mu b^2}{8\pi^2(1-\nu)R^2}(\ln(R/b)+1)+\frac{\mu b^2}{20\pi R^2}. \tag{3.22}$$

Using the definition of Δg_v (Equation (3.9)) and replacing the matrix product with the interface product (i.e. the product of the concentrations at the precipitate-matrix interface), we get

$$-\frac{R_gT}{v_{m,NbCN}}\ln\left(\frac{\text{interface product}}{\text{solubility product}}\right)=-\frac{2\gamma}{R}+\frac{\mu b^2}{8\pi^2(1-\nu)R^2}(\ln(R/b)+1)+\frac{\mu b^2}{20\pi R^2}, \tag{3.23}$$

where

$$\text{interface product}=wt\%Nb^R(wt\%C^R)^x(wt\%N^R)^{1-x}. \tag{3.24}$$

The weight percentage of an element X in the matrix is found using:

$$wt\%X^M=\frac{C_X^MM_X}{\rho_{aus}}, \tag{3.25}$$

where ρ_{aus} is the mass density of austenite.

Combining the three equations for the growth rates (Equation (3.21)) with the equation for the energy changes (Equation (3.23)), results in four equations with four unknowns: v, C_{Nb}^R, C_N^R and C_C^R, which we can solve.

We use the bisection method to solve the following equation:

$$\frac{\text{interface product}}{\text{solubility product}} - \exp\left(-\frac{v_{m,NbCN}}{R_g T}\left(-\frac{2\gamma}{R} + \frac{\mu b^2}{8\pi^2(1-\nu)R^2}(\ln(R/b)+1) + \frac{\mu b^2}{20\pi R^2}\right)\right) = 0, \tag{3.26}$$

which is a non-linear function of v via the interface product, since the interface concentrations in the interface product depend on v via Equation (3.21). Using this bisection method, we get back the growth rate v, and thereby via Equation (3.21) the interface concentrations. Even though the bisection method is know to be very slow and convergences non monotonic, it has the advantages of a low number of function evaluations in one step and guarantees convergences. Later on, in Chapter 7, we will see that even though a method like Ridders (Wikipedia (2015b)) has more function evaluations per time, the resulting computation time is lower.

In the current calculation of the interface concentrations only the elements that participate in the precipitate have influence on these interface concentrations. In Chapter 4, the calculation of the interface concentrations is adjusted, such that also the elements that do not participate in the precipitate influence the calculations.

4

Multi-component KWN model

Now that we have made a new model, based on the approximations in the nucleation rate made by Zurob et al. (2002), in which the evolution of the mean radius was be replaced by the distributions of the radii, we extend it to a multi-component version. Transforming the original model to a multi-component model is done by extending the standard KWN model and Equations (3.1) and (3.2) such that they account for multiple elements. This means that not only the elements participating in the precipitate have influence on the nucleation and growth rate, but all elements in the system do.

4.1. Nucleation

Following Chapter 3, we assume that the time-dependent nucleation rate $I(t)$ for precipitates, used in the source function, is given by:

$$I(t) = (N_{total} - N) Z\beta^* \exp\left(\frac{-\Delta G^*}{k_B T}\right). \tag{3.3}$$

Some of the approximations and calculations done in this nucleation rate do not only depend on elements participating in the precipitates, but on all elements in the system. To account for this effect, we adjust the approximations of the Zeldovich factor, the rate of atomic attachment and the activation energy.

Parameters Z and β^*

Z is the Zeldovich non-equilibrium factor and β^* is the rate of atomic attachment to the critical nucleus. In the non-multi-component version by Zurob et al. (2002) $Z\beta^*$ was approximated by

$$Z\beta^* \approx \frac{D_{pipe} x_{Nb}^M}{a^2}, \tag{4.1}$$

where D_{pipe} is the diffusion coefficient in the dislocation, x_{Nb}^M the molar fraction of niobium in the matrix and a the matrix lattice constant. This choice of using the properties of niobium was based on the assumption that only niobium has an influence on Z and β^*, since it is the slowest diffusing element and hence rate-determining. A better approximation would be to incorporate all elements in the matrix. However, Den Ouden et al. (2013) showed that the difference between an approximation based on the slowest diffusion element and an approximation based on all elements was not that large. The approximation chosen by Zurob et al. (2002), however, was not physically justified, hence we use a different approximation, where Z and β^* are approximated separately.

The Zeldovich factor was found using the definition by Russell (1980) and the following derivation[1]

$$Z = \sqrt{\frac{-1}{2\pi k_B T}\left(\frac{d^2}{dN^2}(\Delta G)\right)\Big|_{R^*}}, \tag{4.2a}$$

$$= \sqrt{\frac{-1}{2\pi k_B T}\frac{(\Delta G)''(R^*)}{(R^*)^4}\frac{v_{at}^2}{16\pi^2}}, \tag{4.2b}$$

$$= \frac{v_{at}}{2\pi\sqrt{k_B T}}\sqrt{-R^*\Delta g_v - \gamma + \frac{\mu b^2}{16\pi^2(1-\nu)R^*}}\left(\frac{1}{R^*}\right)^2, \tag{4.2c}$$

where v_{at} is the atomic volume of the precipitate and the other variables as defined earlier and in the nomenclature at the end of this thesis. A more extensive derivation of the Zeldovich factor can be found in Appendix A. For the rate of atomic attachment to the critical nucleus β^*, we use the definition proposed by Russell (1980):

$$\beta^* = \frac{4\pi(R^*)^2\lambda^a}{a^2}, \tag{4.3}$$

where λ^a is the effective frequency of a structural unit of precipitate type per unit area. This effective frequency is chosen to be dependent on the slowest diffusion element X (i.e. the element with the lowest diffusion coefficient) and is given by

$$\lambda^a = \frac{D_{X,pipe}x_X^M}{a^2}, \tag{4.4}$$

where $D_{X,pipe}$ is the pipe diffusion coefficient of element X, x_X^M the molar fraction of element X in the matrix and a the lattice constant. This leads to

$$\beta^* = \frac{4\pi(R^*)^2 D_{X,pipe}x_X^M}{a^4}. \tag{4.5}$$

For the product $Z\beta^*$ we find

$$Z\beta^* = \frac{v_{at}}{2\pi\sqrt{k_B T}}\sqrt{-R^*\Delta g_v - \gamma + \frac{\mu b^2}{16\pi^2(1-\nu)R^*}}\left(\frac{1}{R^*}\right)^2\frac{4\pi(R^*)^2 D_{X,pipe}x_X^M}{a^4}, \tag{4.6}$$

$$= \frac{v_{at}}{\sqrt{k_B T}}\sqrt{-R^*\Delta g_v - \gamma + \frac{\mu b^2}{16\pi^2(1-\nu)R^*}}\frac{2D_{X,pipe}x_X^M}{a^4} \tag{4.7}$$

Comparing this approximation to the approximation from Zurob et al. (2002), we find Figure 4.1. The approximation by Zurob et al. (2002) lies below the approximation of $Z\beta^*$ when using the separate approximations of Z and β^*. How this effects the final results, will be discussed in Chapter 9.

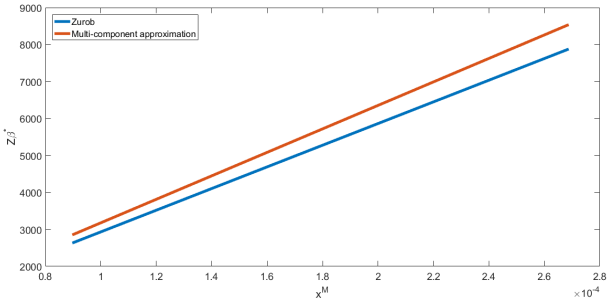

Figure 4.1: Approximations of $Z\beta^*$ by Zurob et al. (2002) and as described in this thesis, for multiple values of the molar fraction of an element in the matrix.

[1] The derivative indicated with the accent is with respect to the precipitate radius R.

Activation energy

ΔG^* is the energy barrier needed to be overcome for nucleation to take place, also known as the activation energy. The activation energy ΔG^*, found in the nucleation rate (Equation (3.8)), and the associated critical radius R^*, found in the source function (Equation (3.2)), are estimated using the expression for the free energy of precipitate formation (Equation (2.1)):

$$\Delta G = V\Delta g_v + A\gamma + \Delta G_d. \tag{2.1}$$

The value of the chemical energy Δg_v is found using Equation (3.9). In this equation we use the weight percentages of the elements in the matrix and in equilibrium. The weight percentage of an element X in the matrix was found using:

$$wt\%X^M = \frac{C_X^M M_X}{\rho_{aus}}, \tag{3.25}$$

where ρ_{aus} is the mass density of austenite. However, this takes into account the concentration of the total system, whereas we would like to calculate the weight percentage in the matrix and the precipitate based respectively on the concentrations in the matrix and the precipitate. For each element $X \in \Psi_P \subseteq \Psi$, where Ψ_P is the set of all elements in the precipitate and Ψ is the set of all elements in the system, we use:

$$wt\%X^M = \frac{C_X^M M_X}{\sum_{Y\in\Psi} C_Y^M M_Y} \quad \text{and} \quad wt\%X^P = \frac{C_X^P M_X}{\sum_{Y\in\Psi_P} C_Y^P M_Y}. \tag{4.8}$$

Using these conversions from concentration to weight percentages, leads to a multi-component version of the activation energy.
Combining all multi-component approximations leads to the following multi-component nucleation rate

$$I(t) = (N_{total} - N)\frac{v_{at}}{\sqrt{k_B T}}\sqrt{-R^*\Delta g_v - \gamma + \frac{\mu b^2}{16\pi^2(1-\nu)R^*}}\frac{2D_{X,pipe}x_X^M}{a^4}\exp\left(\frac{-\Delta G^*}{k_B T}\right), \tag{4.9}$$

where the subscript X refers to the slowest diffusing element in the precipitate considered.

4.2. Growth

In the previous section the nucleation rate $I(t)$, used in the source function $S(R,t)$ was discussed. As described in Chapter 3, the growth rate v as used in the calculation of the precipitate distribution ϕ is defined by Equation (3.19):

$$v(\phi,R,t) = \frac{dR}{dt} = \frac{D_{eff,X}}{R}\frac{C_X^M - C_X^R}{C_x^P - C_x^R}. \tag{3.19}$$

The growth rate (Equation (3.19)) also holds for elements that do not participate in the precipitate. However, since the concentration of those elements in the precipitate is equal to zero, the growth rate changes to

$$v(\phi,R,t) = \frac{dR}{dt} = \frac{D_{eff,X}}{R}\frac{C_X^M - C_X^R}{-C_X^R}, \tag{4.10}$$

for elements that do not participate in the precipitate. In solving the growth rate for the elements in the precipitate we have to use an additional equation to be able to find a unique solution. We use the rewritten equation for the free energy:

$$-\frac{R_g T}{v_{m,NbCN}}\ln\left(\frac{\text{interface product}}{\text{solubility product}}\right) = -\frac{2\gamma}{R} + \frac{\mu b^2}{8\pi^2(1-\nu)R^2}(\ln(R/b)+1) + \frac{\mu b^2}{20\pi R^2}, \tag{4.11}$$

where

$$\text{interface product} = wt\%Nb^R (wt\%C^R)^x (wt\%N^R)^{1-x}. \tag{4.12}$$

In this equation we use the weight percentages of the elements participating in the precipitate. However, as described in the previous section, for the conversion from concentration to weight percentages we need the concentrations of all elements in the system, also those that do not participate in the precipitate:

$$wt\%X^R = \frac{C_X^R M_X}{\sum_{Y \in \Psi} C_Y^R M_Y}. \tag{4.13}$$

Meaning that we need to find the interface concentrations of all elements in the matrix, i.e. the growth rate for all elements in the matrix, leading to N_e equations. This means that for the interface concentration calculations we have N_e equations for the growth rate of each element and $N_e + 1$ unknowns: v and the interface concentration of each of those N_e elements. Again we use the equation for the free energy (Equation (2.1)) as an additional equation (number $N_e + 1$) to be able to solve the system of equations. In this way we derive a multi-component version of the growth rate.

5

Multi-precipitate KWN model

In this chapter, we extend the multi-component model to a version which includes the modelling of different types of precipitates. Throughout this section, we use the following definition

Definition 5.1. *A **type of precipitate p** is the unique combination of the composition of the precipitate, like $NbCN$, AlN and MnS, and the site at which it nucleates, like on dislocations, on grain boundaries and in grains.*

Therefore, when a precipitate of the same composition occurs at two different nucleation sites, it is seen as two types of precipitates with two separate distributions.

For each precipitate type p we use the model for nucleation and growth as described in Chapters 3 and 4. Due to the multi-component properties of this model, no additional model is needed for the interaction between the individual models of each precipitate type. The main features of the multi-precipitate (composition and nucleation site) KWN model are:

- All particles are spherical and classified by their radii in meters (m).
- The time behaviour in seconds (s) of the model is described by the partial differential equation

$$\frac{\partial \phi_p}{\partial t} = -\frac{\partial [v_p \phi_p]}{\partial R} + S_p, \tag{5.1}$$

  in which $\phi_p \equiv \phi_p(R,t)$ in m^{-4} denotes the number density distribution of a precipitate with radius R and at time t, $v_p \equiv v_p(\phi, R, t)$ in ms^{-1} represents the growth rate of a precipitate with radius R and at time t. Further $S_p \equiv S_p(R,t)$ in $\mathrm{m}^{-4}\mathrm{s}^{-1}$ is a source function for a precipitate representing nucleation for the number density distribution of newly appearing precipitates with radius R at time t. The subscript p refers to one unique combination of a precipitate type (composition) and nucleation site as defined in Definition 5.1.

- The value of the source function S_p is given by

$$S_p(R,t) = I_p(t)\delta(R - R_p^*(t)), \tag{5.2}$$

  in which $I_p(t)$ denotes the nucleation rate of a precipitate, $R_p^*(t)$ the critical radius of that precipitate and δ is the Dirac delta function.

The precipitate number density $N_p(t)$ can be retrieved for each precipitate type p separately using the distribution for that specific type of precipitate.

$$N_p(t) = \int_0^\infty \phi_p(R,t)\,dR. \tag{5.3}$$

The precipitate mean radius $\bar{R}_p(t)$ can be retrieved in a similar fashion. We use the bar over the R to emphasise we are dealing with the mean radius.

$$\bar{R}_p(t) = \frac{1}{N_p(t)} \int_0^\infty R\phi_p(R,t)dR, \tag{5.4}$$

Even though no additional model for interaction between the individual models for each precipitate type is needed, the different precipitate types depend on each other via the matrix concentrations, which change during the simulation. When only one type of precipitate is considered in the simulation, we can use the following equation to find the current matrix concentration of element X

$$C_X^M = \frac{C_X^0 - C_X^P f_v}{1 - f_v}, \tag{5.5}$$

where f_v means the volume fraction, defined by

$$f_v = \int_0^\infty \frac{4}{3}\pi R^3 \phi dR. \tag{5.6}$$

However, when simulating different precipitate types at the same time, the concentration of an element X in the matrix can depend on multiple precipitates. We use the following adjusted mass balance to find the concentration of an element X in the matrix

$$C_X^M = \frac{C_X^0 - \sum_{p\in\Theta} C_X^{P(p)} f_v^p}{1 - \sum_{p\in\Theta} f_v^p}, \tag{5.7}$$

where Θ is the set of all precipitate types considered in the model, $C_X^{P(p)}$[1] the concentration of element X in precipitate type p and f_v^p the volume fraction of precipitate type p.

5.1. Various precipitate compositions

In the introduction of the multi-precipitate model, we defined a type of precipitate as the unique combination of a composition of a precipitate and the nucleation site at which it nucleates. In this section, we will only consider types of precipitates which differ in composition, but all nucleate at the same site, namely on dislocations.

5.1.1. Nucleation rate

The nucleation rate $I(t)$ is defined equal to the nucleation rate in Chapter 4, and is defined for each precipitate as:

$$I_p(t) = (N^{total} - \sum_{p\in\Theta} N_p) Z_p \beta_p^* \exp\left(\frac{-\Delta G_p^*}{k_B T}\right), \tag{5.8}$$

where the subscript p refers to the type of precipitate and Θ is the set of precipitates. The definitions of N^{total}, Z_p, β_p^* and ΔG_p^* are equal to those used in Chapter 4, but their values can change due to composition dependent parameters, like diffusion coefficients. These composition dependent parameters will be given later on in this section.

5.1.2. Growth rate

In the previous section the nucleation rate $I_p(t)$, incorporated in the source function $S_p(R,t)$ was discussed. The growth rate v_p as used in the calculation of the precipitate number density distribution ϕ_p is a generalisation to the growth rate as given in Chapter 3 (Equation (3.19)):

$$v_p(\phi,R,t) = \frac{dR_p}{dt} = \frac{D_{eff,X}}{R_p} \frac{C_X^M - C_X^{R(p)}}{C_X^{P(p)} - C_X^{R(p)}}. \tag{5.9}$$

[1] The superscript P refers to the precipitate itself, whereas the subscript p refers the type of precipitate.

where p stands for the precipitate type considered. This growth rate holds for all elements in the matrix. However, the concentrations on the interface and the concentration in the precipitate of those elements are calculated for precipitate type p. For the elements that are not in precipitate type p, the growth rate therefore changes to

$$v_p = \frac{dR_p}{dt} = \frac{D_{eff,X}}{R_p} \frac{C_X^M - C_X^{R(p)}}{-C_X^{R(p)}}. \tag{5.10}$$

For the growth rate is it important to use the correct calculation of the matrix concentration as stated in Equation (5.7).

5.1.3. Composition dependent parameters

In the nucleation rate some parameters depend on the composition of the precipitate.
The activation energy, ΔG^*, is based on the free energy of precipitate formation on dislocations:

$$\Delta G_p = V\Delta(g_v)_p + A\gamma_p - \frac{\mu b^2 R \ln(R/b)}{2\pi(1-\nu_p)} - \frac{\mu b^2 R}{5}. \tag{3.17}$$

For all types of precipitates (composition), this equation is defined the same. However, the value of the parameters, like ν, the poisson ratio, is different for each type of precipitate.
The composition also influences the value of β_p^*, since it is based on the slowest diffusing element in the precipitate:

$$\beta_p^* = \frac{4\pi(R^*)^2 D_{X,pipe} x_X^M}{a^2}. \tag{5.11}$$

An overview of all changing parameters, for the compositions of the precipitates we consider, is given in Table 5.1. Most of the parameters originate from Zurob et al. (2002), Cheng (2003) and Den Ouden (2015). The interfacial energies of AlN and MnS are found using the derivation by Cheng (2003) (in Section 5.1.3 of his work).

Table 5.1: Precipitate type dependent variables and parameters.

	NbC	NbN	AlN	MnS	NbC_xN_{1-x}
ν	0.293	0.293	0.25	0.3	0.293
$\log(K(T))$	$2.06 - \frac{6700}{T}$	$2.80 - \frac{8500}{T}$	$1.03 - \frac{6740}{T}$	$4.092 - \frac{10590}{T}$	$x\log(K_{NbC}) + (1-x)\log(K_{NbN})$ $+x\log(x) + (1-x)\log(1-x)$
v_m	13.39×10^{-6}	12.72×10^{-6}	12.563×10^{-6}	21.805×10^{-6}	$x v_{m,NbC} + (1-x) v_{m,NbN}$
γ	1.0058 $-0.4493 \times 10^{-3} T$	0.9717 $-0.4340 \times 10^{-3} T$	0.8707 $-0.3 \times 10^{-3} T$	1.1412 $-0.4 \times 10^{-3} T$	$2.5 \times 10^{-5}(T_{sol} - T)^{1.5} + 0.375$

5.2. Various nucleation sites

As defined in the introduction of this chapter, a type of precipitate p refers to a unique combination of the composition of a precipitate and the site at which it nucleates. Since precipitates with the same composition can occur at different nucleation sites, this leads to a separate equation for each precipitate type p.

The model used previously in this thesis describes the nucleation on dislocations, but nucleation on grain boundaries and in grains (Den Ouden et al. (2013)) is also considered to be of great influence. Nucleation on other precipitates or inclusions is not considered here, because the area available for nucleation is much lower than the grain boundary area. Interphase nucleation during austenite to ferrite transformation requires the introduction of special models and is recommended for future work.

The nucleation rate, growth rate and various variables for the chosen nucleation sites are given in this section. Both the nucleation rate and the growth rate have the same form as in Chapter 4, but have different values and descriptions for the individual parameters. Some of the parameters only depend on the composition, some only depend on the nucleation site and some depend on both.

5.2.1. Nucleation

For each precipitate type p the nucleation rate $I(t)$ is defined as:

$$I_p(t) = (N_{site}^{total} - \sum_{p \in \Theta_{site}} N_p) Z_p \beta_p^* \exp\left(\frac{-\Delta G_p^*}{k_B T}\right), \tag{5.12}$$

where Θ_{site} is the set of all precipitates that nucleate at a particular nucleation site (of precipitate type p). To illustrate the definition of Θ_{site}, we given an example. Assume we have a simulation with:

- $NbCN$ on dislocations, on grain boundaries and homogeneous nucleation,
- MnS on dislocations, and on grain boundaries,
- AlN on dislocations, and homogeneous nucleation,

and look at precipitate type p_1, chosen as $NbCN$ on dislocations. Then $\Theta_{site} = \Theta_{dis}$ is the set of all $NbCN$, MnS and AlN precipitates on dislocations. When we look at another precipitate type p_2, chosen as MnS on grain boundaries, $\Theta_{site} = \Theta_{gb}$ is the set of all $NbCN$ and MnS precipitates on grain boundaries, since AlN are not chosen to nucleate on grain boundaries.
The definitions of the parameters in the nucleation rate that are nucleation site dependent will be described below.

Number of available nucleation positions

The nucleation rate depends on the maximum number of available nucleation positions minus the number of nucleation positions already occupied. The number of occupied nucleation positions is found by summing over the precipitates types in a specific nucleation site. We use Figure 5.1 as an illustration. The set of all types of precipitates in indicated by Θ. This can be divided in three groups: Θ_{dis}, Θ_{gb} and Θ_{hom}, corresponding to all precipitate types that respectively nucleate on dislocations, on grain boundaries and in grains. When a precipitate type p nucleates on grain boundaries and therefore lies in Θ_{gb}, we sum over all precipitates that also lie in Θ_{gb} to find the number of nucleation positions occupied. We take the sum over all precipitates at one certain nucleation site, since only those precipitates occupy nucleation positions for that specific precipitate type, independent of their composition.

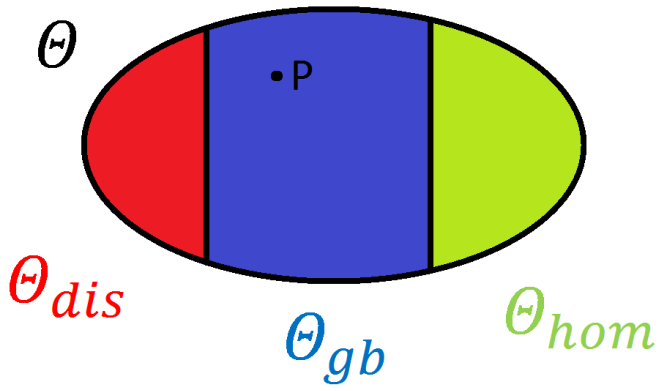

Figure 5.1: Illustration of the set of all precipitates, grouped by the site they nucleate on.

N_{site}^{total} is the number of available nucleation positions at a specific site for a precipitate type p and is defined as the product of a fitting parameter F_{site} and an approximation of the number of nucleation positions. Since, the number of available nucleation positions depends on the nucleation site, and we assume it is independent of the composition of the precipitate type, the subscript $site$ is used. The fitting factor is introduced because of the uncertainty of the correct formula of the maximum number density per site.

The following definitions are used:

- Dislocations (Zurob et al. (2002)):

$$N_{dis}^{total} = F_{dis}\frac{\rho}{b}, \tag{5.13}$$

  where b is the length of the Burgers vector, and ρ the dislocation density.

- Grain boundaries:

$$N_{gb}^{total} = F_{gb}\frac{3}{2a^2 R_{grain}}, \tag{5.14}$$

  where R_{grain} is the radius of a grain and a the matrix lattice parameter.

- Homogeneous nucleation:

$$N_{hom}^{total} = F_{hom}\frac{4}{a^3}. \tag{5.15}$$

Activation energy

Since the free energy of precipitate formation depends on the site where the precipitate is formed, also the activation energy and the critical radius vary. Generally speaking, the free energy of precipitate formation is given by

$$\Delta G = V\Delta g_v + A\gamma + \Delta G_{site}, \tag{5.16}$$

where ΔG_{site} is the free energy change due to nucleation on that specific site. Taking the derivative of this equation to R and setting it equal to zero, returns the activation energy and the critical radius.
For nucleation on dislocations the derivation of the activation energy and the critical radius has been done in Section 3.1, but for the completeness of this section some equations are reproduced. The free energy change due to nucleation on dislocations is given by

$$\Delta G_{site} = \Delta G_{dis} = -\frac{\mu b^2 R\ln(R/b)}{2\pi(1-\nu)} - \frac{\mu b^2 R}{5}, \tag{3.16}$$

which leads to the total free energy of precipitate formation

$$\Delta G = \frac{4}{3}\pi R^3\Delta g_v + 4\pi R^2\gamma - \frac{\mu b^2 R\ln(R/b)}{2\pi(1-\nu)} - \frac{\mu b^2 R}{5}. \tag{3.17}$$

The activation energy and corresponding critical radius are found using the derivative of this equation to R and setting it equal to zero, as described in Section 3.1:

$$\frac{d(\Delta G)}{dR} = 4\pi R^2\Delta g_v + 8\pi R\gamma - \frac{\mu b^2}{2\pi(1-\nu)}(\ln(R/b)+1) - \frac{\mu b^2}{5} = 0. \tag{3.18}$$

For nucleation on grain boundaries the free energy change due to the release of grain boundary energy at the position of the precipitate is given by

$$\Delta G_{site} = \Delta G_{gb} = -\pi R^2\gamma_{gb}, \tag{5.17}$$

which leads to the total free energy of precipitate formation

$$\Delta G = \frac{4}{3}\pi R^3\Delta g_v + 4\pi R^2\gamma - \pi R^2\gamma_{gb}, \tag{5.18}$$

where γ_{gb} is the grain boundary energy. The value of γ_{gb} depends on the material considered. In the case of austenite we take the value of 0.75 J/m^2. Taking the derivative of the equation to R and setting it equal to zero, leads to the activation energy and critical radius for nucleation on grain boundaries:

$$\begin{cases} R^*_{gb} &= \frac{\gamma_{gb}-4\gamma}{2\Delta g_v}, \\ \Delta G^*_{gb} &= \frac{\pi(-\gamma_{gb}+4\gamma)^3}{12\Delta g_v^2}. \end{cases} \tag{5.19}$$

For homogeneous nucleation, the free energy due to nucleation does not exists ($\Delta G_{site} = 0$) and the free energy of precipitate formation is defined by

$$\Delta G = V\Delta g_v + A\gamma. \tag{5.20}$$

Taking the derivative of this equation to R and setting it equal to zero, leads to the activation energy and critical radius for homogeneous nucleation:

$$\begin{cases} R^*_{hom} &= \frac{-2\gamma}{\Delta g_v}, \\ \Delta G^*_{hom} &= \frac{16\pi\gamma^3}{3\Delta g_v^2}. \end{cases} \tag{5.21}$$

Parameters Z and β^*

Z_p and β^*_p are respectively the Zeldovich factor and the rate of atomic attachment, both dependent on precipitate type p. As described in Section 5.1 β^* depends on the slowest diffusing element, and includes the diffusion coefficient for that element:

$$\beta^*_p = \frac{4\pi(R^*)^2 D_{site,X} x_X^M}{a^2}. \tag{5.22}$$

As the subscript $site$ in $D_{site,X}$ indicates, different diffusion coefficients are used for different nucleation sites. For nucleation on dislocations, on grain boundaries and homogeneous nucleation we take the pipe diffusion coefficient, the grain boundary diffusion coefficient and the bulk diffusion coefficient respectively. For all sites we again take the diffusion coefficient of the slowest diffusing element.
The Zeldovich factor is based on the free energy of precipitate formation, via the general formula for the Zeldovich factor (Russell (1980))

$$Z_p = \sqrt{\frac{-1}{2\pi k_B T}\left(\frac{d^2}{dN^2}(\Delta G)_p\right)\Big|_{R^*}}, \tag{5.23}$$

where R^* is the critical radius and ΔG is the free energy of precipitate formation. For nucleation on dislocations, the Zeldovich factor is derived in Chapter 4. For homogeneous nucleation the Zeldovich factor can be found in various studies in literature, such as Den Ouden et al. (2013) and Russell (1980), and is given by

$$Z = \frac{v_{at}\sqrt{\gamma}}{2\pi\sqrt{k_B T}}\left(\frac{1}{R^*}\right)^2, \tag{5.24}$$

where v_{at} is the atomic volume of the precipitate, k_B the Boltzman constant and T the temperature. We derive the Zeldovich factor for nucleation on grain boundaries, using the free energy of precipitate formation for nucleation on grain boundaries given before.

$$Z = \sqrt{\frac{-1}{2\pi k_B T}\left(\frac{d^2}{dN^2}(\Delta G)\right)\Big|_{R^*}}, \tag{5.25a}$$

$$= \sqrt{\frac{-1}{2\pi k_B T}\frac{(8\pi R^*\Delta g_v + 8\pi\gamma - 2\pi\gamma_{gb})}{(R^*)^4}\frac{v_{at}^2}{16\pi^2}}, \tag{5.25b}$$

$$= \frac{v_{at}}{2\pi\sqrt{k_B T}}\sqrt{\gamma - \frac{1}{4}\gamma_{gb}}\left(\frac{1}{R^*}\right)^2. \tag{5.25c}$$

$$\tag{5.25d}$$

A more extensive derivation of the Zeldovich factor can be found in Appendix A.

This leads to the following Zeldovich factors for the various nucleation sites we are considering:

$$Z_{site} = \begin{cases} \frac{v_{at}}{2\pi\sqrt{k_B T}} \sqrt{-R^* \Delta g_v - \gamma + \frac{\mu b^2}{16\pi^2(1-\nu)R^*}} \left(\frac{1}{R^*}\right)^2 & \text{for dislocations,} \\ \frac{v_{at}}{2\pi\sqrt{k_B T}} \sqrt{\gamma - \frac{1}{4}\gamma_{gb}} \left(\frac{1}{R^*}\right)^2 & \text{for grain boundaries,} \\ \frac{v_{at}}{2\pi\sqrt{k_B T}} \sqrt{\gamma} \left(\frac{1}{R^*}\right)^2 & \text{for homgeneous nucleation.} \end{cases} \tag{5.26}$$

5.2.2. Growth

In the previous section the nucleation rate $I_p(t)$, incorporated in the source function $S_p(R,t)$ was discussed. Similar to the growth rate for precipitates with different compositions, we find for v_p:

$$v_p(\phi, R, t) = \frac{dR_p}{dt} = \frac{D_{site,X}}{R_p} \frac{C_X^M - C_X^R}{C_X^P - C_X^R}, \tag{5.27}$$

where p stands for the precipitate type considered[1]. The growth rate holds for each elements in the system. However, the concentrations on the interface and the concentration in the precipitate are calculated for precipitate type p. The growth rate for elements that are not in this precipitate type p therefore changes to

$$v_p(\phi, R, t) = \frac{dR_p}{dt} = \frac{D_{site,X}}{R_p} \frac{C_X^M - C_X^R}{-C_X^R}. \tag{5.28}$$

When the precipitates on dislocations and on grain boundaries grow, they also take up elements from the bulk. We therefore use an effective diffusion coefficient for growth on dislocations and growth on grain boundaries and the bulk diffusion coefficient for homogeneous nucleation. The effective diffusion coefficient is defined as

$$D_{eff} = f_v^{site} D_{site} + (1 - f_v^{site}) D_{bulk}, \tag{5.29}$$

where f_v^{site} is the volume fraction of the specific site in the system. This is a new parameter belonging to a nucleation site and should not be confused with the volume fraction of the precipitate.
The volume fraction of dislocations is approximated using the dislocation density and the dislocation pipe radius R_{core}

$$\begin{aligned} f_v^{dis} &= \frac{V_{dis}}{V_{sys}}, \\ &= \frac{\pi R_{core}^2 \rho V_{sys}}{V_{sys}}, \\ &= \pi R_{core}^2 \rho, \end{aligned} \tag{5.30}$$

where R_{core} is approximated by b (Zurob et al. (2002)), the burgers vector. The volume fraction of the grain boundaries is approximated using the radius of a grain R_{grain} and the thickness of the grain boundary δ_{gb}.

$$\begin{aligned} f_v^{gb} &= \frac{V_{gb}}{V_{sys}}, \\ &= \frac{A_{gb}\delta_{gb}}{V_{sys}}, \\ &= \frac{V_{sys}\frac{3}{2R_{grain}}\delta_{gb}}{V_{sys}}, \\ &= \frac{3\delta_{gb}}{2R_{grain}}, \end{aligned} \tag{5.31}$$

[1] The superscript P refers to the precipitate itself, whereas the subscript p refers the type of precipitate.

where we use that the area of a grain boundary A_{gb} is defined as

$$\begin{aligned} A_{gb} &= \frac{A_{grain}}{2} N_{grain}, \\ &= 2\pi R_{grain}^2 \frac{V_{sys}}{4/3\pi R_{grain}^3}, \\ &= V_{sys} \frac{3}{2R_{grain}}. \end{aligned} \tag{5.32}$$

This leads to the following list of diffusion coefficients in the growth rate (Equation (5.27)):

$$D_{site,X} = \begin{cases} D_{pipe}\pi b^2 \rho + D_{bulk}(1-\pi b^2\rho) & \text{for dislocations,} \\ D_{gb}\frac{3\delta_{gb}}{2R_{grain}} + D_{bulk}(1-\frac{3\delta_{gb}}{2R_{grain}}) & \text{for grain boundaries,} \\ D_{bulk} & \text{for homogeneous,} \end{cases} \tag{5.33}$$

where δ_{gb} is the thickness of the grain boundary and R_{grain} the radius of a grain ($\approx$ 10 micrometer). The diffusion coefficient (bulk, pipe or grain boundary) of the slowest diffusing element is used in the effective diffusion coefficient.
When solving the growth rate for nucleation on dislocations, we combined Equation (5.27) with the solubility product, corrected for the Gibbs-Thomson effect, to get a unique solution for all element concentrations:

$$\frac{\text{interface product}}{\text{solubility product}} - \exp\left(-\frac{v_{m,p}}{R_g T}\left(-\frac{2\gamma}{R} + \frac{\mu b^2}{8\pi^2(1-\nu)R^2}(\ln(R/b)+1) + \frac{\mu b^2}{20\pi R^2}\right)\right) = 0. \tag{3.26}$$

For nucleation on grain boundaries we use a similar derivation as for nucleation on dislocations. We start with the derivative of Equation (5.18), the equation for the free energy release of precipitation formation on grain boundaries, and rewrite it:

$$\frac{d\Delta G}{dR} = 4\pi R^2 \Delta g_v + 8\pi R\gamma - 2\pi R\gamma_{gb} = 0, \tag{5.34}$$

$$-4\pi R^2 \Delta g_v = 8\pi R\gamma - 2\pi R\gamma_{gb}, \tag{5.35}$$

$$\Delta g_v = -\frac{2\gamma}{R} + \frac{\gamma_{gb}}{2R} \tag{5.36}$$

Using the definition of Δg_v (Equation (3.9)), we find the required additional equation:

$$\frac{\text{interface product}}{\text{solubility product}} - \exp\left(-\frac{v_{m,p}}{R_g T}\left(-\frac{2\gamma}{R} + \frac{\gamma_{gb}}{2R}\right)\right) = 0. \tag{5.37}$$

Following this same procedure, gives for homogeneous nucleation

$$\frac{\text{interface product}}{\text{solubility product}} - \exp\left(-\frac{v_{m,p}}{R_g T}\left(-\frac{2\gamma}{R}\right)\right) = 0, \tag{5.38}$$

which is the common Gibbs-Thomson effect.

5.2.3. Nucleation site dependent parameters

As stated before, we consider three different nucleation sites: dislocations, grain boundaries and homogeneous nucleation. For different precipitate compositions we found different values of some parameters, like the poisson ratio ν and the interfacial energy γ. However, the nucleation site only has influence on the diffusion coefficients. For example, dislocations and grain boundaries can be seen as element highways in the crystal structure.
For all the elements in the system, we need the diffusion coefficients at the three different nucleation sites given before. The diffusion coefficient is generally described by the Arrhenius relation:

$$D = D_0 \exp\left(\frac{-Q_d}{R_g T}\right), \tag{5.39}$$

where R_g is the gas constant, T the temperature in Kelvin, D_0 is the maximum diffusion coefficient (at infinite temperature) in m^2/s and Q_d the activation energy for diffusion in J/mol. The diffusion coefficients on the three nucleation sites are given in Table 5.2. Some of the grain boundary diffusion coefficients in literature are given in m^3/s, with the following definition:

$$s\delta_{gb}D_{gb} = (s\delta_{gb}D_{gb})_0 \exp\left(\frac{-Q_{gb}}{R_g T}\right) \tag{5.40}$$

These value have to be divided by the thickness of the grain δ_{gb} and a segregation factor s. For the thickness of the grain we take a value of $3a \approx 10^{-9}$, where a is the matrix lattice constant and for the segregation factor we take the value one. For the pipe diffusion coefficient we also find a deviating definition in literature (Kaur et al. (1989))

$$\pi R_{core}^2 D_{pipe} f_d^{-1} = (\pi R_{core}^2 D_{pipe} f_d^{-1})_0 \exp\left(\frac{-Q_d}{R_g T}\right), \tag{5.41}$$

where R_{core} is the dislocation pipe radius, and f_d the correlation factor for dislocation diffusion. To retrieve D_0 from this equation we have to divide the pre-factor $(\pi R_{core}^2 D_{pipe} f_d^{-1})_0$ by $\pi R_{core}^2 f_d^{-1}$. Following Zurob et al. (2002) we approximate the dislocation pipe radius by the burgers vector b and let f_d be equal to one. Comparing the bulk diffusion coefficients to the pipe and grain boundary diffusion coefficients for various temperatures in Figure 5.2, we find that the pipe and grain boundary diffusion coefficients are indeed higher than the bulk diffusion coefficients, as mentioned before (highway in the crystal structure).

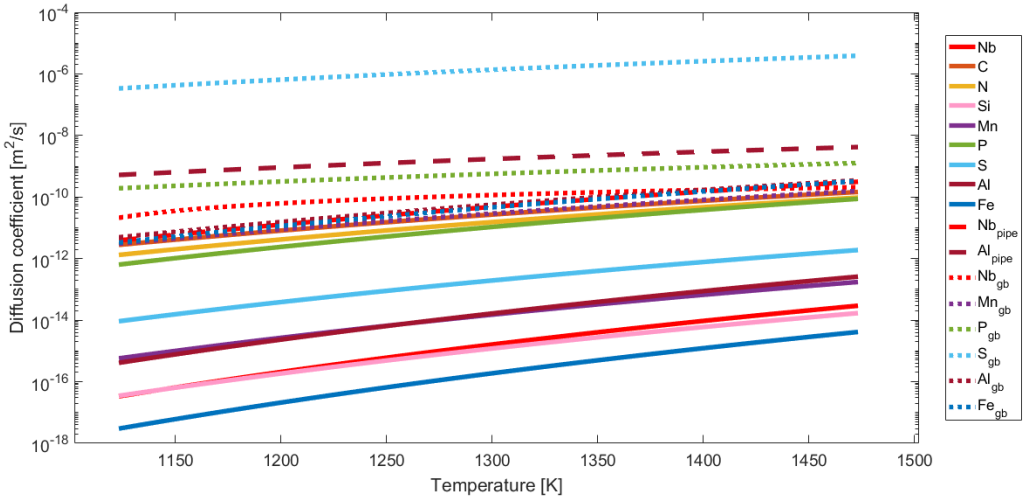

Figure 5.2: Diffusion coefficients for various temperatures, elements and sites.

Table 5.2: Diffusion coefficients (bulk, pipe and grain boundary) in austenite. D_0 is given in m^2/s and Q_d is given in kJ/mol. The values originate from LeClaire and Neumann (1990), Zurob et al. (2002), Murch (2001), Cheng (2003), Kucera and Stransky (1981) and Kaur et al. (1989).

Element	$D_{bulk}: D_0$	$D_{bulk}: Q_d$	$D_{pipe}: D_0$	$D_{pipe}: Q_d$	$D_{gb}: D_0$	$D_{gb}: Q_d$
Nb	0.83×10^{-4}	266.5	4.1×10^{-4}	172.5	(a)	(a)
C	0.48×10^{-4}	155.5	(c)	(c)	(c)	(c)
N	0.91×10^{-4}	168.56	(c)	(c)	(c)	(c)
Si	7.0×10^{-6}	243	(c)	(c)	(c)	(c)
Mn	0.16×10^{-4}	224.6	(c)	(c)	(b)	(b)
P	6.3×10^{-4}	193.4	(c)	(c)	5.49×10^{-7}	74.31
S	0.5×10^{-4}	209.3	(c)	(c)	1.01×10^{-2}	96.23
Al	2.51×10^{-4}	253.4	3.4×10^{-6}	82.01	3.0×10^{-4}	167.4
Fe	0.49×10^{-4}	284.1	(c)	(c)	8.25×10^{-4}	180.5

(a) For Nb (niobium) we have found two measurements of diffusion data on grain boundaries in Kaur et al. (1989): $s\delta_{gb}D_{gb} = 1.20 \times 10^{-19}$ m^3/s at 1288.5 K and $s\delta_{gb}D_{gb} = 7.40 \times 10^{-20}$ m^3/s at 1210 K. Fitting the Arrhenius relation (Equation (5.39)) through these points, results in the following diffusion coefficient dependent on temperature

$$D_{gb} = 1.8906 \times 10^{-7} \exp\left(\frac{-79691}{R_g T}\right). \tag{5.42}$$

Since this method is only based on two data points (at high temperatures), the accuracy of this diffusion coefficient can be doubted.

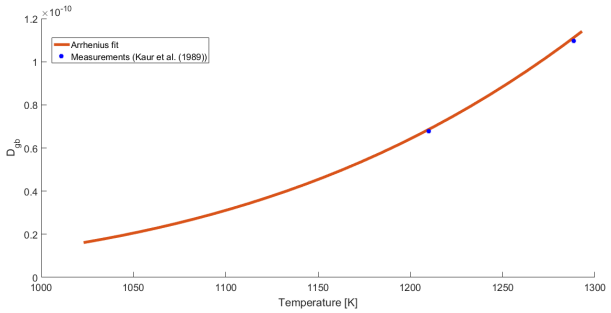

Figure 5.3: Fit of the Arrhenius line through niobium diffusion data.

(b) Pandit (2011) and Murch (2001) describe that during experimental work they discovered that grain boundary diffusivity for substitutional atoms like Cr, Mn, Ni and Mo in austenite to be within a factor 3 of the Arrhenius line described by $(\delta_{gb}D_b)_0 = 5.4 \times 10^{-14}$ m^3/s and $Q_d = 155$ kJ/mol. Since no other information for these elements is found, we use this Arrhenius line for the grain boundary diffusivity of Mn (manganese).

(c) For some of the elements no dislocation and/or grain boundary diffusivity data is available. We use the following approximation:

$$\begin{cases} D_{pipe} = \alpha(T) D_{bulk}, \\ D_{gb} = \beta(T) D_{bulk}, \end{cases} \tag{5.43}$$

where α and β are temperature dependent parameters, that are based on the ratios of the known bulk and pipe diffusion coefficients and the known bulk and grain boundary diffusion coefficients of the other elements respectively. The values of α and β are given in Table 5.3 and plotted in Figure 5.4, together with the average values of α and β. We use these averages multiplied with the bulk diffusion coefficient for the elements of which we do not know the pipe and/or grain boundary diffusion coefficient. One should be careful using such an approximation, since it can influence the final results.

Table 5.3: $\alpha(T)$ and $\beta(T)$ for the elements in the system, when available.

Element	$\alpha(T)$	$\beta(T)$
Nb	$5.06 \exp\left(\frac{94000}{R_g T}\right)$	
P		$8.71 \times 10^{-4} \exp\left(\frac{119090}{R_g T}\right)$
S		$202.00 \exp\left(\frac{113070}{R_g T}\right)$
Al	$1.35 \times 10^{-2} \exp\left(\frac{171390}{R_g T}\right)$	$1.20 \exp\left(\frac{86000}{R_g T}\right)$
Fe		$16.84 \exp\left(\frac{103600}{R_g T}\right)$

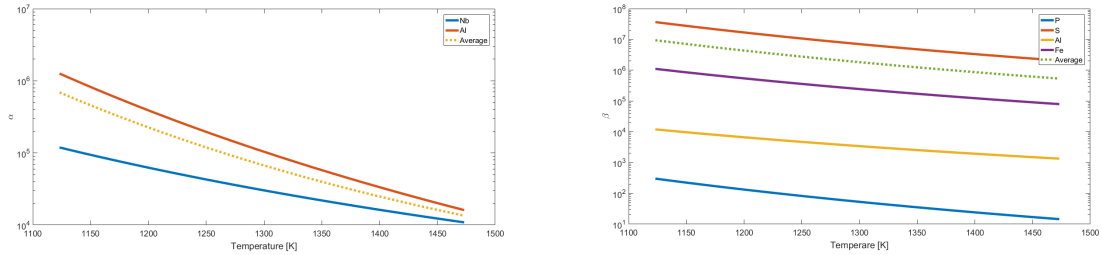

(a) $\alpha(=\frac{D_{pipe}}{D_{bulk}})$ for different temperatures

(b) $\beta(=\frac{D_{gb}}{D_{bulk}})$ for different temperatures

Figure 5.4: $\alpha(T)$ and $\beta(T)$ for the elements in the system, when available.

The diffusion coefficients of the elements in the matrix largely influence the growth of the precipitates. When the multi-component version of the model is used, each element, and thereby each diffusion coefficient, influences the growth rate. The approximations that are used for the diffusion coefficients are based on few data points or no data is even available. For such an important parameter in the model it is therefore recommended, for future work, to perform experiments to find the missing diffusion coefficients.

6

Numerical Methods

In this thesis we are looking for a solution to the evolution problem introduced and described in Chapter 3:

$$\frac{\partial \phi}{\partial t} = -\frac{\partial [v\phi]}{\partial R} + S, \tag{3.1}$$

Since this partial differential equation (PDE) is non-linear in ϕ, we find an approximation of the solution using a numerical method. In this chapter we will start with the introduction of multiple PDE solvers, and describe which one we choose to use and why. Thereafter we will do an analysis of the resulting discretised system and an overview of the various algorithms used will be given.

6.1. Numerical methods to solve PDE

Generally speaking, one can use four approaches for finding a solution for a PDE: the finite volume method (FVM), the finite difference method (FDM), the finite element method (FEM) and the Discontinuous Galerkin (GD) (or spectral method). For all four methods, values are calculated at discrete mesh points in the radius domain. However, traditional FDMs have the disadvantages that they cannot handle discontinuities and energy and mass are not rigorously conserved. For FEMs this mass and energy conservation is not straightforward either and one has to take special care to ensure a conservative solution. The FVM is based on the fact that many physical laws are conservation laws, i.e. what goes into one cell on one side needs to leave the same cell on another side. Following this idea, one ends up with a formulation that consists of flux conservation equations defined in an averaged sense over the cells. In this way the method guarantees the conservation of fluxes through a particular control volume. The GD method also gives conversation of mass. However, this method is especially applicable if the solution has discontinuities, which is not the case for our problem. More information on the given numerical methods can be found in Leveque (2007), Van Kan et al. (2014) and Wikipedia (2016d).
In this thesis we will use the finite volume method, combined with an upwind method. Although, the finite volume method, as well as the upwind method are theoretically first order in both time and place, we use these methods as they are simple methods, preserve the stability and more importantly monotonicity[1] of the numerical solution unconditionally and guarantee conservation. Another advantage of this method is that it is easily formulated for non-uniform grids.

6.2. Radius domain

Since precipitates nucleate with a critical radius, the focus of the solution will be in the neighbourhood of this radius. Precipitates with a radius much larger than the critical radius will be little found. We would like to create a radius domain, such that the number density distribution can be represented in more detail at small radii. This leads to a logarithmic (non-uniform) radius domain. As described in the previous section, the finite volume method can easily be formulated for non-uniform grids.

[1] A method is called monotonicity-preserving if $Q_i^n \geq Q_{i+1}^n$ for all i implies that $Q_i^{n+1} \geq Q_{i+1}^{n+1}$ for all i, where n is the time step and Q_i is the approximation in cell i. It is guarantees that any discontinuities cannot become oscillatory, but at most smeared in future time steps (Leveque (2007)).

The radius domain, chosen in the range from 0.1 nm to 1×10^4 nm, is divided in multiple cells with a logarithmic distance $\Delta R(i)$, i.e.

$$\frac{\Delta R(i+1)}{\Delta R(i)} = \text{constant} > 1, \text{as illustrated in Figure 6.1.}$$

Two radius vectors are used during the implementation:

- R(i), describing the centre points of the cells, where i numbers the cells in the radius domain.
- Re(i), describing the edges of the cells.

This is needed since the solution of the differential equation is given at the centre points, but other unknowns such as the growth rate are given at the cell edges. Precipitates with a critical radius neither grow or dissolve, precipitates with a radius smaller than the critical radius dissolve and precipitates with a radius larger than the critical radius start to grow. This means that the growth rate equals zero for radii equal to the critical radius, negative for radii smaller than the critical radius and positive for radii larger than the critical radius.

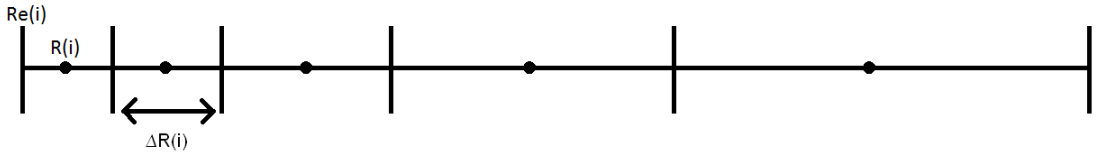

Figure 6.1: Illustration of the radius domain.

As the figure indicates, we use a vertex-centered finite volume method, meaning that the cells are surrounding the node point, lying in the middle of the cell, at which the volume average value $\phi_i(R,t)$ is calculated.

6.3. Discretisation of the PDE

Now that we have defined the radius domain, we discretise the PDE, such that we can find the volume average value, i.e. approximation to the solution at the node points described in the previous section.
Starting from Equation (3.1):

$$\frac{\partial \phi}{\partial t} = -\frac{\partial [v\phi]}{\partial R} + S, \tag{3.1}$$

we choose n points in the particle radius domain in the manner as described in Section 6.2 and let $\boldsymbol{\phi}$ be a column vector containing the n unknowns. We integrate both sides of the equation over a cell Ω_i (surrounding a point i) in the radius domain:

$$\int_{\Omega_i} \frac{\partial \boldsymbol{\phi}}{\partial t} dR = \int_{\Omega_i} -\frac{\partial (\boldsymbol{\phi} v)}{\partial R} dR + \int_{\Omega_i} S dR. \tag{6.1}$$

Approximating each part of Equation 6.1, yields the following expressions

- For the time derivative

$$\int_{\Omega_i} \frac{\partial \boldsymbol{\phi}}{\partial t} dR \approx \Delta R_i \frac{d\boldsymbol{\phi}_i}{dt}, \tag{6.2a}$$

- For the growth term (using Leveque (2007))

$$\begin{aligned}\int_{\Omega_i} -\frac{\partial(\boldsymbol{\phi} v)}{\partial R} dR &= -(\boldsymbol{\phi} v)\big|_{\Gamma_i}, \\ &= -((\boldsymbol{\phi} v)_{i+\frac{1}{2}} - (\boldsymbol{\phi} v)_{i-\frac{1}{2}}), \\ &\approx -[(v^-_{i+\frac{1}{2}}\boldsymbol{\phi}_{i+1} + v^+_{i+\frac{1}{2}}\boldsymbol{\phi}_i) - (v^-_{i-\frac{1}{2}}\boldsymbol{\phi}_i + v^+_{i-\frac{1}{2}}\boldsymbol{\phi}_{i-1})], \\ &= -[-v^+_{i-\frac{1}{2}}\boldsymbol{\phi}_{i-1} + (v^+_{i+\frac{1}{2}} - v^-_{i-\frac{1}{2}})\boldsymbol{\phi}_i + v^-_{i+\frac{1}{2}}\boldsymbol{\phi}_{i+1}], \\ &= v^+_{i-\frac{1}{2}}\boldsymbol{\phi}_{i-1} - (v^+_{i+\frac{1}{2}} - v^-_{i-\frac{1}{2}})\boldsymbol{\phi}_i - v^-_{i+\frac{1}{2}}\boldsymbol{\phi}_{i+1}. \end{aligned} \tag{6.2b}$$

  The growth rates $v_{i-\frac{1}{2}}$ and $v_{i+\frac{1}{2}}$ are respectively the growth rates at Re(i) and Re(i+1). Also, in these equations the superscripts + and − mean the positive and negative part respectively. The positive part and negative part of a number a are defined as

$$\begin{cases} a^+ = \max(a, 0), \\ a^- = \min(a, 0). \end{cases}$$

- For the source function

$$\int_{\Omega_i} S dR = \int_{\Omega_i} \delta(R - R^*) I(t) dR = I(t)\mathbb{1}_{R^* \in \Omega_i}, \tag{6.2c}$$

  where $\mathbb{1}$ is the indicator function.

We have discretised Equation (3.1), which can now be written as

$$\frac{\partial \boldsymbol{\phi}}{\partial t} = A\boldsymbol{\phi} + S. \tag{6.3}$$

The matrix A, an $n \times n$ matrix, and the column vector S, an $n \times 1$ vector are both non-linear functions of $\boldsymbol{\phi}$ and defined as

$$A_{i,i-1}(\boldsymbol{\phi}) = \frac{1}{\Delta R_i} v^+_{i-\frac{1}{2}}(\boldsymbol{\phi}) \qquad \text{for } i = 2, \dots, n, \tag{6.4a}$$

$$A_{i,i}(\boldsymbol{\phi}) = -\frac{1}{\Delta R_i} v^+_{i+\frac{1}{2}}(\boldsymbol{\phi}) + \frac{1}{\Delta R_i} v^-_{i-\frac{1}{2}}(\boldsymbol{\phi}) \qquad \text{for } i = 1, \dots, n, \tag{6.4b}$$

$$A_{i,i+1}(\boldsymbol{\phi}) = -\frac{1}{\Delta R_i} v^-_{i+\frac{1}{2}}(\boldsymbol{\phi}) \qquad \text{for } i = 1, \dots, n-1, \tag{6.4c}$$

$$S_i(\boldsymbol{\phi}) = \frac{1}{\Delta R_i} I(t_i)\mathbb{1}_{R^* \in \Omega_i}, \qquad \text{for } i = 1, \dots, n-1, \tag{6.4d}$$

and $A_{i,j}(\boldsymbol{\phi}) = 0$ if not defined above.

6.4. Eigenvalue analysis

If we investigate the properties of the matrix A combined with the properties of the growth rate v and critical radius R^* at a certain time, we can distinguish the following three situations

- For each Ω_i with $R < R^*$, $R \in \Omega_i$ we have $v_{i-\frac{1}{2}}, v_{i+\frac{1}{2}} < 0$.
- For each Ω_i with $R^* \in \Omega_i$ we have $v_{i-\frac{1}{2}} < 0$ and $v_{i+\frac{1}{2}} > 0$.
- For each Ω_i with $R > R^*$, $R \in \Omega_i$ we have $v_{i-\frac{1}{2}}, v_{i+\frac{1}{2}} > 0$.

Let i be such that we have the first situation. For each Ω_i with $R < R^*$, $R \in \Omega_i$ we have $v_{i-\frac{1}{2}}, v_{i+\frac{1}{2}} < 0$. Then we find for the upper diagonal:

$$\begin{aligned} A_{i,i+1}(\boldsymbol{\phi}) &= -\frac{1}{\Delta R_i} v^-_{i+\frac{1}{2}}(\boldsymbol{\phi}) \\ &= -\frac{1}{\Delta R_i} v_{i+\frac{1}{2}}(\boldsymbol{\phi}), \end{aligned} \tag{6.5a}$$

for the lower diagonal

$$\begin{aligned} A_{i+1,i}(\boldsymbol{\phi}) &= A_{(i+1),(i+1)-1}(\boldsymbol{\phi}) \\ &= \frac{1}{\Delta R_{i+1}} v^{+}_{(i+1)-\frac{1}{2}}(\boldsymbol{\phi}) \\ &= \frac{1}{\Delta R_{i+1}} v^{+}_{i+\frac{1}{2}}(\boldsymbol{\phi}) \\ &= 0, \end{aligned} \tag{6.5b}$$

and for the main diagonal

$$\begin{aligned} A_{i,i}(\boldsymbol{\phi}) &= -\frac{1}{\Delta R_i} v^{+}_{i+\frac{1}{2}}(\boldsymbol{\phi}) + \frac{1}{\Delta R_i} v^{-}_{i-\frac{1}{2}}(\boldsymbol{\phi}) \\ &= \frac{1}{\Delta R_i} v_{i-\frac{1}{2}}(\boldsymbol{\phi}). \end{aligned} \tag{6.5c}$$

This means that for the first case we only have an element on the upper and main diagonal in $A(\boldsymbol{\phi})$. Now let i be such that we have the second situation. For each Ω_i with $R^* \in \Omega_i$ we have $v_{i-\frac{1}{2}} < 0$ and $v_{i+\frac{1}{2}} > 0$. Then we find for the upper diagonal:

$$\begin{aligned} A_{i,i+1}(\boldsymbol{\phi}) &= -\frac{1}{\Delta R_i} v^{-}_{i+\frac{1}{2}}(\boldsymbol{\phi}) \\ &= 0, \end{aligned} \tag{6.6a}$$

for the lower diagonal

$$\begin{aligned} A_{i,i-1}(\boldsymbol{\phi}) &= \frac{1}{\Delta R_i} v^{+}_{i-\frac{1}{2}}(\boldsymbol{\phi}) \\ &= 0, \end{aligned} \tag{6.6b}$$

and for the main diagonal

$$\begin{aligned} A_{i,i}(\boldsymbol{\phi}) &= -\frac{1}{\Delta R_i} v^{+}_{i+\frac{1}{2}}(\boldsymbol{\phi}) + \frac{1}{\Delta R_i} v^{-}_{i-\frac{1}{2}}(\boldsymbol{\phi}) \\ &= -\frac{1}{\Delta R_i} v_{i+\frac{1}{2}}(\boldsymbol{\phi}) + \frac{1}{\Delta R_i} v_{i-\frac{1}{2}}(\boldsymbol{\phi}). \end{aligned} \tag{6.6c}$$

This means that for the second situation we only have the main diagonal. Now let i be such that we have the third situation. For each Ω_i with $R > R^*$, $R \in \Omega_i$ we have $v_{i-\frac{1}{2}}, v_{i+\frac{1}{2}} > 0$. Then we find for the upper diagonal:

$$\begin{aligned} A_{i,i+1}(\boldsymbol{\phi}) &= -\frac{1}{\Delta R_i} v^{-}_{i+\frac{1}{2}}(\boldsymbol{\phi}) \\ &= 0, \end{aligned} \tag{6.7a}$$

for the lower diagonal

$$\begin{aligned} A_{i+1,i}(\boldsymbol{\phi}) &= A_{i+1,i+1-1}(\boldsymbol{\phi}) \\ &= \frac{1}{\Delta R_{i+1}} v^{+}_{i+1-\frac{1}{2}}(\boldsymbol{\phi}) \\ &= \frac{1}{\Delta R_{i+1}} v^{+}_{i+\frac{1}{2}}(\boldsymbol{\phi}) \\ &= \frac{1}{\Delta R_{i+1}} v_{i+\frac{1}{2}}(\boldsymbol{\phi}), \end{aligned} \tag{6.7b}$$

and for the main diagonal

$$\begin{aligned} A_{i,i}(\boldsymbol{\phi}) &= -\frac{1}{\Delta R_i} v^{+}_{i+\frac{1}{2}}(\boldsymbol{\phi}) + \frac{1}{\Delta R_i} v^{-}_{i-\frac{1}{2}}(\boldsymbol{\phi}) \\ &= -\frac{1}{\Delta R_i} v_{i+\frac{1}{2}}(\boldsymbol{\phi}). \end{aligned} \tag{6.7c}$$

This means that for the third case we have a lower and main diagonal, leading to the three-block structure of $A(\boldsymbol{\phi})$ depicted as ($\times$ indicates a possibly non-zero value)

$$\left[\begin{array}{c|c} U & B \\ \hline 0 & L \end{array}\right] = \left[\begin{array}{cccc|cccc} \times & \times & & & & & & \\ & \times & \times & & & & & \\ & & \times & \times & \times & & & \\ \hline & & & & \times & \times & & \\ & & & & \times & \times & \times & \\ & & & & & \times & \times & \\ & & & & & & \times & \times \end{array}\right], \tag{6.8}$$

where U is an upper-diagonal matrix, L a lower-diagonal matrix and B a matrix with possibly one non-zero value.
The time-dependent eigenvalues of this block matrix are given by the eigenvalues of the individual blocks U and L (Wikipedia (2015a)). From the structure of the individual blocks we know, the eigenvalues are on the diagonal, resulting in following eigenvalues:

$$\lambda_i = -\frac{1}{\Delta R_i} v^+_{i+\frac{1}{2}}(\boldsymbol{\phi}) + \frac{1}{\Delta R_i} v^-_{i-\frac{1}{2}}(\boldsymbol{\phi}) \tag{6.9}$$

Again we can distinguish the three situations:

- For each Ω_i with $R < R^*$, $R \in \Omega_i$ we have $v_{i-\frac{1}{2}}, v_{i+\frac{1}{2}} < 0$, so

$$\lambda_i = \frac{1}{\Delta R_i} v_{i-\frac{1}{2}}(\boldsymbol{\phi}), \tag{6.10}$$

  with $v_{i-\frac{1}{2}} < 0$, so negative eigenvalues.

- For each Ω_i with $R^* \in \Omega_i$ we have $v_{i-\frac{1}{2}} < 0$ and $v_{i+\frac{1}{2}} > 0$, so

$$\lambda_i = -\frac{1}{\Delta R_i} v_{i+\frac{1}{2}}(\boldsymbol{\phi}) + \frac{1}{\Delta R_i} v_{i-\frac{1}{2}}(\boldsymbol{\phi}), \tag{6.11}$$

  are negative eigenvalues, since $v_{i-\frac{1}{2}} < 0 \Rightarrow \frac{1}{\Delta R_i} v_{i-\frac{1}{2}}(\boldsymbol{\phi}) < 0$ and $v_{i+\frac{1}{2}} > 0 \Rightarrow -\frac{1}{\Delta R_i} v_{i+\frac{1}{2}}(\boldsymbol{\phi}) < 0$.

- For each Ω_i with $R > R^*$, $R \in \Omega_i$ we have $v_{i-\frac{1}{2}}, v_{i+\frac{1}{2}} > 0$, so

$$\lambda_i = -\frac{1}{\Delta R_i} v_{i+\frac{1}{2}}(\boldsymbol{\phi}), \tag{6.12}$$

  with $v_{i+\frac{1}{2}} > 0$, so negative eigenvalues.

This shows that the eigenvalues are negative and real for all i, meaning that any time integration method can be made stable by reducing the time step, as long as the stability region of the method includes (part of) the negative real axis (Vuik et al. (2015)). Furthermore, Vonk (2016) found that the Backward Euler method gives the best results for the physical problem we are solving and so we will again use this Backward Euler method, where we solve the obtained non-linear equation using Picard's Fixed Point method. We combine the Backward Euler method with a variable time step selection as will be described later on.

6.5. Backward Euler

When solving the equation

$$\frac{d\boldsymbol{Y}}{dt} = f(\boldsymbol{Y}, t), \tag{6.13}$$

the implicit backward Euler method is defined by [1]

$$\boldsymbol{Y}_{n+1} = \boldsymbol{Y}_n + \Delta t \boldsymbol{f}(t_{n+1}, \boldsymbol{Y}_{n+1}), \text{ where } \boldsymbol{Y}_{n+1} \approx \boldsymbol{Y}(t_{n+1}) \text{ and } t_{n+1} = t_n + \Delta t. \tag{6.14}$$

[1] Note that the new time is also found in this step.

Applying the Backward Euler method to our discretised differential Equation (6.3), we find Equation (6.15). Notice that the subscript $n+1$ in (6.15) now refers to the $n+1$ time step and not the individual elements of A anymore.

$$\boldsymbol{\phi}_{n+1} = \boldsymbol{\phi}_n + \Delta t(A_{n+1}\boldsymbol{\phi}_{n+1} + S_{n+1}), \tag{6.15}$$

where

$$\boldsymbol{\phi}_{n+1} \approx \boldsymbol{\phi}(t_{n+1}),\ A_{n+1} \approx A(\boldsymbol{\phi}_{n+1}, t_{n+1}) \text{ and } S_{n+1} \approx S(\boldsymbol{\phi}_{n+1}, t_{n+1}). \tag{6.16}$$

We solve this equation using Picard's Fixed Point method. The fixed point method states that we can find a fixed point p of a function g if we start with an initial point $p^{(0)}$ and use the iteration $p^{(k)}$ by $p^{(k)} = g(p^{k-1})$. If this sequence converges to p and g is continuous it holds that $p = g(p)$ and we have found a fixed point p (Vuik et al. (2015)). Applying the Fixed Point method to Equation (6.14), we find

$$\boldsymbol{\phi}_{n+1}^{k+1} = g(\boldsymbol{\phi}_{n+1}^{k}), \quad k = 0, 1, \ldots \tag{6.17a}$$

$$= \boldsymbol{\phi}_n^k + \Delta t(A_{n+1}^k \boldsymbol{\phi}_{n+1}^k + S_{n+1}^k) \tag{6.17b}$$

as the Picard's iteration step. In this iteration, k indicates the fixed point iteration and n the time step. During the first simulations, we found that the computation times were too high and we adjusted Picard's Fixed Point method, as will be described in Chapter 7.

Even though the Backward Euler method is numerically quite stable, an additional method is needed to guarantee a high accuracy. To keep the truncation error below a certain user-defined tolerance level, the step size is chosen adaptively, meaning that it adapts to the truncation error. Another advantage of using an adaptive time step, is the automatic increase of the time step when limited changes appear in the approximation of the solution, i.e. it increases the efficiency of the solving method. An approximation for the truncation error is given by

$$\tau_{n+1} = ||\boldsymbol{\phi}_{n+1} - \tilde{\boldsymbol{\phi}}_{n+1}||_\infty, \tag{6.18}$$

where $\boldsymbol{\phi}$ and $\tilde{\boldsymbol{\phi}}$ are two numerical methods. To apply this adaptive step size, we need a second numerical method to compare it to our Backward Euler method. We choose the Backward Euler method itself for this, but using two smaller step sizes $\frac{h}{2}$ leading to two solutions, at time $t_n + \frac{\Delta t}{2}$ and time $t_n + \frac{\Delta t}{2} + \frac{\Delta t}{2} = t_n + \Delta t$, which we can then compare to the one step Backward Euler at time $t_n + \Delta t$. Subsequently we use a tolerance parameter to determine whether we accept or reject our approximation:

$$\text{TOL} = \text{percentage} \cdot ||\boldsymbol{\phi}_{n+1}||_\infty. \tag{6.19}$$

Since we find two solutions $\boldsymbol{\phi}_{n+1}$ and $\tilde{\boldsymbol{\phi}}_{n+1}$ at t_{n+1}, we can choose which solution to use as a final solution for that specific time step. We choose to use the solution obtained using the two smaller time steps, since it is more accurate. This leads to Algorithm 6.1, where the parameters Δt_{start}, α β, percentage and t_{end} are set by the user.

6.6. Multi-precipitate

As described in Chapter 5, multiple types of precipitates can nucleate and grow at several nucleation sites at the same time. Each precipitate type at a specific nucleation site gives one distribution, leading to a set of distributions when simulating multiple precipitate types and/or nucleation sites. For example, we would like to simulate three types of precipitates: AlN, MnS, and NbCN, where each precipitate can nucleate at three sites: dislocations, grain boundaries and in the grains. This leads to 9 distributions:

$$\phi_{AlN,dis} \quad \phi_{AlN,gb} \quad \phi_{AlN,hom} \quad \phi_{MnS,dis} \quad \phi_{MnS,gb} \quad \phi_{MnS,hom} \quad \phi_{NbCN,dis} \quad \phi_{NbCN,gb} \quad \phi_{NbCN,hom}$$

We solve the 9 partial differential equations related to these distributions simultaneously, meaning that in one Backward Euler step, all 9 distributions should be accepted or the time step is changed. In Algorithm 6.2 we see the adjusted version of the Backward Euler algorithm for multiple types of precipitates and multiple nucleation sites. We compute the solutions simultaneously, since the distribution of one precipitate has influence on the distribution of another precipitate via the matrix concentrations. Also the Picard iteration is executed simultaneously for the same reason, leading to Algorithm 6.3 for the Picard iterations.

Algorithm 6.1: Euler Backward with adaptive time step algorithm

```
Set Δt = Δt_start;
while time(j)+Δt < tend
    Compute φ_{n+1/2} via Picard;
    Compute φ_{n+1/2+1/2} = φ_{n+1} based on φ_{n+1/2} via Picard;
    Compute φ̃_{n+1} via Picard; %Use φ_{n+1/2+1/2} as initial guess for the
        BE method
    Compute τ_{n+1};
    Compute TOL;
    if τ_{n+1} > β TOL
        Reject φ_{n+1};
        Set Δt = Δt/2;
    elseif τ_{n+1} > TOL
        Accept φ_{n+1};
        Set Δt= Δt·0.9·(TOL/τ_{n+1})^{1/2};
        Set n = n+1;
    elseif τ_{n+1} > TOL/α
        Accept φ_{n+1};
        Set n = n+1;
    else
        Accept φ_{n+1};
        Set Δt= Δt·0.9·(TOL/τ_{n+1})^{1/2}/α;
        Set n = n+1;
    end
end
```

Algorithm 6.2: Euler Backward with adaptive time step algorithm

```
Set Δt = Δt_start;
while time(n)+Δt < tend
    for prec = [all precipitates types (compositions)]
        for site = [all sites at which that precipitate nucleates]
            Compute φ_{n+1/2} via Picard;
            Compute φ_{n+1/2+1/2} = φ_{n+1} based on φ_{n+1/2} via Picard;
            Compute φ̃_{n+1} via Picard; %Use φ_{n+1/2+1/2} as initial guess
                for the BE method
            Compute τ_{n+1};
            Compute TOL;
            if Picard returns no solution
                Δt = Δ/2
                Reset time step
            end
        end
    end
    if any(τ_{n+1} > β TOL)
        Reject all φ_{n+1};
        Set Δt = Δt/2;
        Reset time step
    elseif all(τ_{n+1} > TOL)
        Accept all φ_{n+1};
        Set Δt= Δt·0.9·(TOL/τ_{n+1})^{1/2};
        Set n = n+1;
    elseif all(τ_{n+1} > TOL/α)
        Accept all φ_{n+1};
        Set n = n+1;
    else
        Accept all φ_{n+1};
        Set Δt= Δt·0.9·(TOL/τ_{n+1})^{1/2}/α;
        Set n = n+1;
    end
end
```

Algorithm 6.3: Picard algorithm for multiple distributions

```
while solution available
    if the new distribution is not allowed % Concentrations and/or
        volume fractions are physically incorrect
        no solution can be found
        solution(prec,site) = 0;
        return to Backward Euler algorithm
    end
    for prec = [all precipitates types (compositions)]
        for site = [all sites at which that precipitate nucleates]
            φ^{k+1}_{n+1} = φ^k_n + Δt(A^k_{n+1} φ^k_{n+1} + S^k_{n+1});
            Compute REL ERR between φ^{k+1}_{n+1} and φ^k_{n+1};
            Compute TOL;
            if REL ERROR <= TOL
                solution(prec,site) = 1;
            end
        end
    end
    if sum(sum(solution)) == total_sites % All distributions have a
        correct solution
        solution found
        return to Backward Euler algorithm
    else % Picard iteration continues
        continue
    end
end
```

7

Computational issues

During the first simulations, using the algorithms described in the previous chapter, a number of computational issues arose. In this chapter, these issues will be explained and solutions are proposed. After applying the improvements mentioned in this chapter, simulations are done of which the results can be found in Chapters 8, 9 and 10.

7.1. Precipitate nucleation size

In Zurob et al. (2002), the size at which precipitates start to nucleate was set at $\tilde{R} = \alpha \cdot R^*$, where α was chosen as 1.05. This was done to avoid numerical instability of the algorithm and is physically justified since it accounts for the fact that nucleated precipitates can only grow if their radius is slightly larger than the nucleation radius. In our numerical approach this translates to determining the size class $[R_{j^*-\frac{1}{2}}, R_{j^*+\frac{1}{2}}]$ which incorporates the radius $\tilde{R}$, and adding precipitates to it. Using this radius, we replace the source function in Equation (3.2) with

$$S(R,t) = \delta(R - \tilde{R}_c(t))I(t), \tag{7.1}$$

where $\tilde{R}_c$ represents the centre of the size class which includes $\tilde{R}$. $\tilde{R}$ can be seen as an adjusted critical radius and as stated before, was chosen by Zurob et al. (2002) as $1.05R^*$. In some literature on precipitation, the adjusted critical radius $\tilde{R}$ was chosen as R_{k_BT}, where the value k_BT is assumed to be a very small number, meaning that the adjusted radius is slightly bigger than the critical radius. Based on this idea, we test two new approaches for the adjusted critical radius, based on physical approximations:

- Find the adjusted critical radius R_{k_BT} at which the corresponding free energy is k_BT lower than the activation energy ΔG^* (see Figure 7.1). (Found in various publications, these include Maugis and Gouné (2005).)
- Find the adjusted critical radius R_{k_BT} by using the approximation of the change in the number of atoms in the precipitate. (see Figure 7.2).

For the first approach we solve the following equation for the energy balance using the Newton-Raphson method:

$$(\Delta G^* - k_BT) = V\Delta g_v + A\gamma - \frac{\mu b^2 R_{k_BT}\ln(R_{k_BT}/b)}{2\pi(1-\nu)} - \frac{\mu b^2 R_{k_BT}}{5}, \tag{7.2}$$

which after substitution and rewriting gives

$$f(R_{k_BT}) = -\Delta G^* + k_BT + (\frac{4}{3}\pi(R_{k_BT})^3)\Delta g_v + (4\pi(R_{k_BT})^2)\gamma - \frac{\mu b^2 R_{k_BT}\ln(R_{k_BT}/b)}{2\pi(1-\nu)} - \frac{\mu b^2 R_{k_BT}}{5} = 0. \tag{7.3}$$

For the Newton-Raphson method we need the derivative of the function f when solving $f(x) = 0$ for x. Differentiating Equation (7.3) with respect to R_{k_BT} yields

$$\frac{df}{dR_{k_BT}} = 4\pi(R_{k_BT})^2\Delta g_v + 8\pi R_{k_BT}\gamma - \frac{\mu b^2}{2\pi(1-\nu)}\left(\ln\left(\frac{R_{k_BT}}{b}\right)+1\right) - \frac{\mu b^2}{5}. \tag{7.4}$$

As an initial guess we take the critical radius R^* multiplied by a factor 1.05, to make sure we find a radius greater than the critical radius[1].

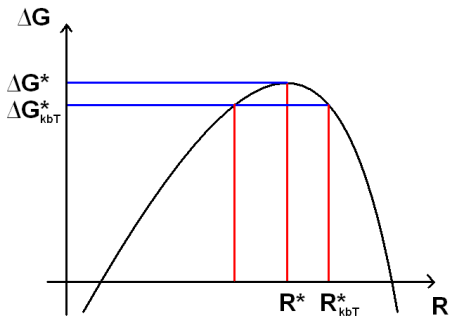

Figure 7.1: Free energy curve againt the radius.

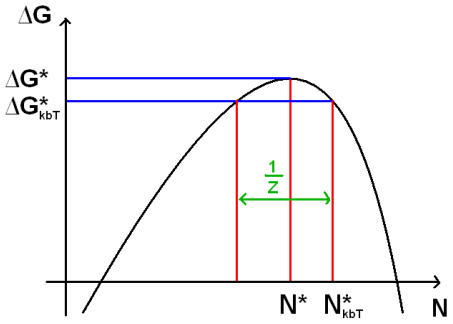

Figure 7.2: Free energy curve against the number of atoms in the precipitate.

The second approach of finding a critical radius R_{k_BT} is by using the Zeldovich factor and the change in the number of atoms in the precipitate. The Zeldovich factor for nucleation on dislocations was derived in Chapter 4:

$$Z = \frac{v_{at}}{2\pi\sqrt{k_B T}}\sqrt{-R^*\Delta g_v - \gamma + \frac{\mu b^2}{16\pi^2(1-\nu)R^*}}\left(\frac{1}{R^*}\right)^2 \tag{7.5}$$

Using this Zeldovich factor we set the adjusted critical radius R_{k_BT} as

$$R_{k_BT} = \frac{1}{2Z}\frac{v_{at}}{4\pi(R^*)^2} + R^*. \tag{7.6}$$

The first term in this equation follows from Russell (1980) which states that the change in the number of atoms in the precipitate can be approximated by $1/(2Z)$ when decreasing the free energy by k_BT (illustrated in Figure 7.1). Using this approximation we find the increase in critical radius given above:

$$\begin{cases} N &= \frac{1}{v_{at}}\frac{4}{3}\pi(R^*)^3 := f(R), \\ dN &= f'(R)dR \Rightarrow dR = \frac{dN}{f'(R)}, \end{cases} \quad \Rightarrow \quad dR = \frac{dN}{f'(R)} = \frac{1}{2Z}\frac{v_{at}}{4\pi(R^*)^2}. \tag{7.7}$$

We will compare both the results of the simulations and the computation time using the different approximations of R_{k_BT}:

1. $R_{k_BT} = 1.05R^*$, as done by Zurob et al. (2002). (*1.05 Zurob et al. (2002)*)

2. Finding the radius at which the corresponding activation energy is k_BT lower than the activation energy ΔG^*. (*Newton (with ΔG)*)

3. Using the approximation of the change in the number of atoms in the precipitate dN. (*Zeldovich factor*)

The approximations were compared in simulations, using a $NbCN$ precipitate nucleating on dislocations. The results are given in Figure 7.3 and the computation times in Table 7.1. From Figure 7.3 we see there is no large change in the results, neither in the precipitate number density nor in the precipitate mean diameter, caused by a different choice of R_{k_BT}. Also, looking at the computation time we see no clear standout. However, we would like to be able to choose the best approach from the three and see whether the general approximation of $1.05R^*$ by Zurob et al. (2002) is comparable to the other two physical based approximations.

[1] Note that there might also be a radius smaller than the critical radius which agrees with Equation (7.3).

Method	Run 1 (s)	Run 2 (s)	Run 3 (s)	Run 4 (s)	Run 5 (s)	Average
1.05 (Zurob et al. (2002))	75	70	72	65	67	69.8
Newton (with ΔG)	74	68	67	66	77	70.4
Zeldovich factor	70	69	71	72	69	70.2

Table 7.1: Computation times of a 100,000 seconds simulation using different approximations for the adjusted critical radius R_{k_BT}.

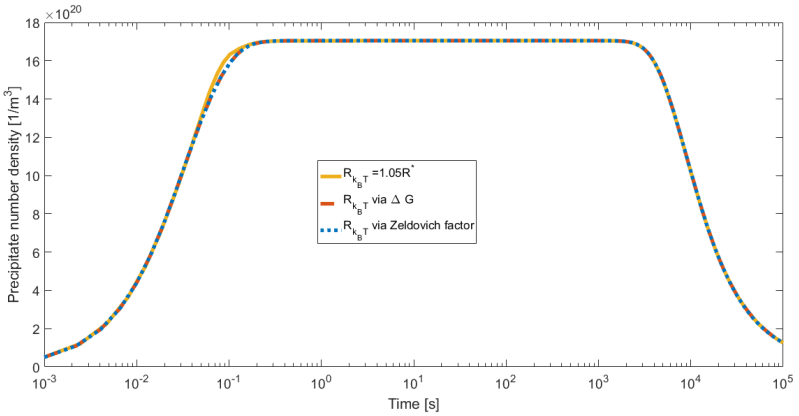

(a) Precipitate number density.

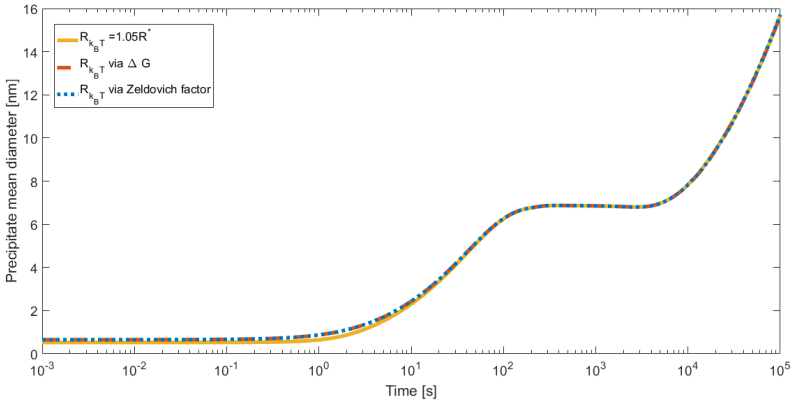

(b) Precipitate mean diameter.

Figure 7.3: Simulation results with different approximations of R_{k_BT}.

In Figures 7.4 and 7.5 we compare the factor $\frac{R_{k_BT}}{R^*}$ to the factor 1.05 initiated by Zurob et al. (2002). We see that at the beginning of the simulation the physical approximations lead to higher factors for R_{k_BT}. Looking at the results in Figure 7.3 this higher factor translates to a slightly lower bend in the precipitate number density and a slightly lower precipitate mean diameter. However, as stated before the differences are minimal. As the simulation continues, the factor in Figures 7.4 and 7.5 decrease and even drop below 1.05. Since the R_{k_BT} term is connected to nucleation, and no nucleation occurs anymore after a few seconds, the influence of the factor dropping below 1.05 can not be seen in the results. We choose to use the approximation that uses the Zeldovich factor, since this factor is also used in the multi-component version of the KWN model, it is a physically based approximation and has a comparable computation time to the other two methods.

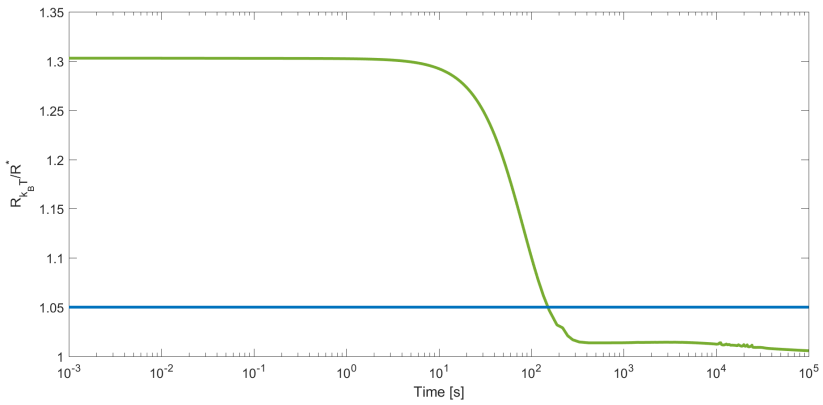

Figure 7.4: Factor $\frac{R_{k_BT}}{R^*}$ in time, where R_{k_BT} is found using the Zeldovich factor.

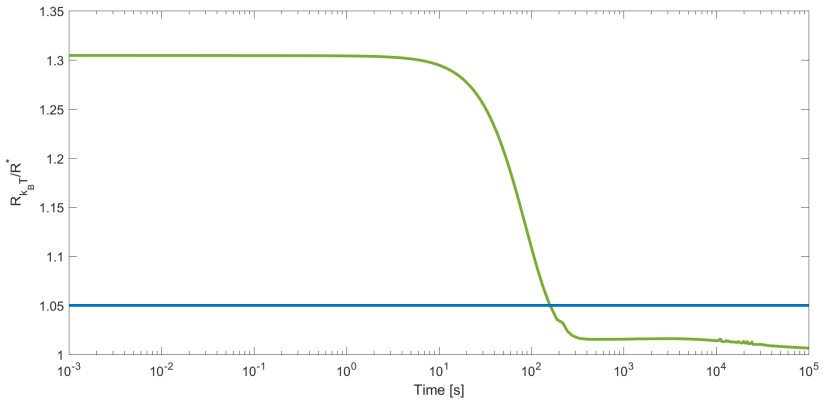

Figure 7.5: Factor $\frac{R_{k_BT}}{R^*}$ in time, where R_{k_BT} is found using Newton's method.

7.1.1. Compensation for the loss of nucleated precipitates

Besides the choice of size class to which the newly nucleated precipitates are added, a second difficulty appears. When adding precipitates to the chosen size class, a problem occurs when the critical radius R^* lies in that same size class. We use Figure 7.6 as an illustration. If the two radii R^* and R_{k_BT} are incorporated in the same cell, the newly nucleated precipitates are added to that cell (illustrated by the green striped rectangle). At the left side of this cell the growth rate is negative, but at the right side of this cell the growth rate is positive, meaning that in the next time step (t_{n+1}), a part of the newly nucleated precipitates will disappear again (illustrated by the yellow shaded part of the green striped rectangle), since part of these precipitates have a radius smaller than the critical radius, and thus a negative growth rate. This loss of nucleated precipitates is a side effect of the FVM method caused by the averaging over one cell of this method. It is an undesirable effect because precipitates with a radius R_{k_BT} are intended to be stable and to grow. To compensate for this loss, we add more nuclei than actually needed (indicated by the dark green stripes), since we know a part will disappear again. The part of the compensation that will stay behind after growth and shrinkage (precipitates with radius larger than the critical radius and illustrated by the second yellow shaded rectangle) needs to be equal in size as the part that disappears. Therefore the two yellow shaded rectangles should be the same in size, leading to the following nucleation rate

$$\tilde{I}(t) = \Delta R_i \frac{I(t)}{Re(i+1) - R^*} \tag{7.8}$$

If the radii are incorporated in different cells, the nuclei are added to a different cell (a cell that lays right of the cell which incorporates R^*), meaning that all of the nucleated precipitates stays in the system and no compensation is needed.

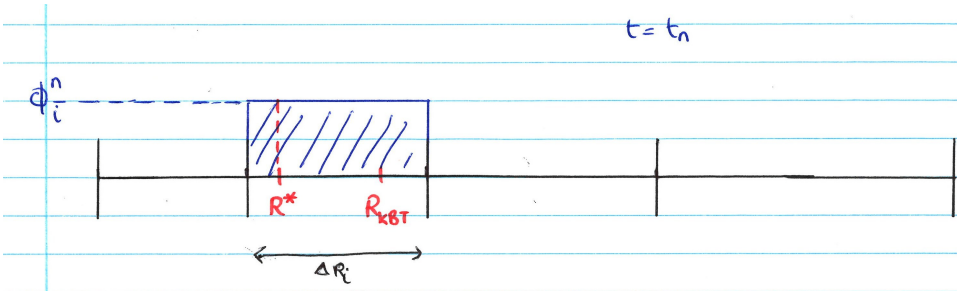

(a) First timestep.

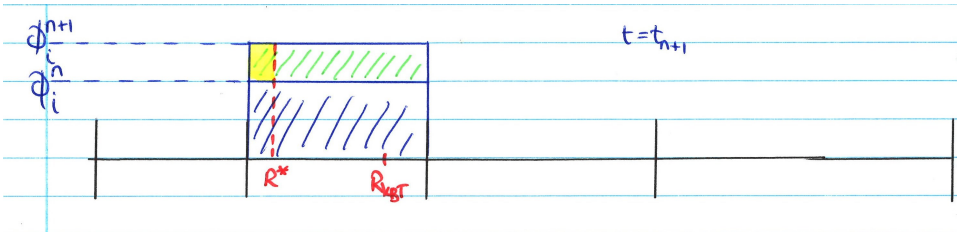

(b) Second timestep.

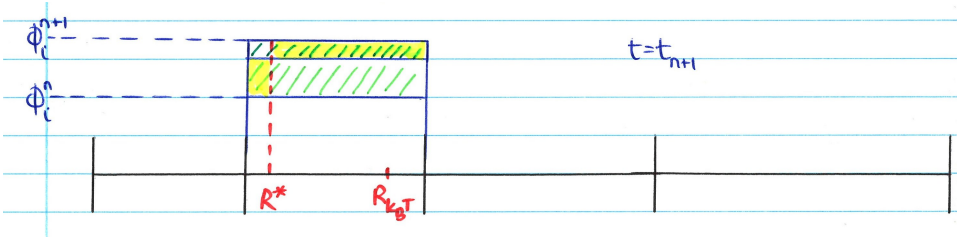

(c) Second timestep with adjusted nucleation rate.

Figure 7.6: Illustration of the compensation of nucleation, because of the incorporation of the critical radii R^* and R_{k_BT} in the same cell.

7.2. Computation time

During the first simulations we had a great difficulty in running simulations for large simulation times. To give an indication: it took around 240 seconds to calculate 10 simulation seconds, whereas we would like to have around 100,000 simulation seconds to compare it to experimental data and earlier obtained results. The next improvements were introduced to lower the computation time.

7.2.1. Picard iteration

The long computation time was mainly caused by the intensive calculations done in the right-hand side of the Picard iteration.

$$\boldsymbol{\phi}_{n+1}^{k+1} = \boldsymbol{\phi}_n + \Delta t(A_{n+1}^k \boldsymbol{\phi}_{n+1}^k + S_{n+1}^k) \tag{7.9}$$

To reduce the computation time, we adjust the Picard iterate by solving part of the right-hand side for the next iteration

$$\boldsymbol{\phi}_{n+1}^{k+1} = \boldsymbol{\phi}_n + \Delta t(A_{n+1}^k \boldsymbol{\phi}_{n+1}^{k+1} + S_{n+1}^k)] \tag{7.10}$$

Rewriting this equation yields the new Picard's step

$$[I - \Delta t A_{n+1}^k]\boldsymbol{\phi}_{n+1}^{k+1} = \boldsymbol{\phi}_n + \Delta t S_{n+1}^k \tag{7.11}$$

To solve Equation (7.11) the matrix $[I - \Delta t A_{n+1}^k]$ must be inverted, which sounds even more intensive than the calculations before. However, due to the block structure of A this invert is straight-forward and not as time consuming as the matrix multiplication done in Equation (7.9).

7.2.2. Growth rate

Besides the computation time of the Picard iteration itself, the calculations inside the Picard step are also time consuming. Especially the calculation of the growth rate is very intensive. The growth rate was found by solving non-linear Equation (3.26) for the growth rate v.

$$\frac{\text{interface product}}{\text{solubility product}} - \exp\left(-\frac{v_{m,NbCN}}{R_g T}\left(-\frac{2\gamma}{R} + \frac{\mu b^2}{8\pi^2(1-\nu)R^2}(\ln(R/b)+1) + \frac{\mu b^2}{20\pi R^2}\right)\right) = 0, \tag{7.12}$$

which is a function of v via the interface product, since the interface concentrations in the interface product depend on v via Equation (3.21).
We test the following root finding methods and compare the computation times:

- Newton's Method, a root finding method which uses the first derivative of the function that is evaluated and is defined by

  $$x_{n+1} = x_n - \frac{f(x_n)}{f'(x_n)}. \tag{7.13}$$

  (Vuik et al. (2015))

- Bisection Method, a bracketing method which repeatedly bisects a given interval (by dividing it in two equal parts) and then select a sub-interval in which a root must lie (Vuik et al. (2015)).

- Ridders' Method, a bracketing method which repeatedly bisects a given interval in a smart way and then select a sub-interval in which a root must lie. This method converges quadratically, when the function is well-behaved close to the root. It uses the midpoint of the original interval and a fourth point defined by

  $$x_4 = x_3 + (x_3 - x_1)\frac{\text{sign}(f(x_1) - f(x_2))f(x_3)}{\sqrt{f(x_3)^2 - f(x_1)f(x_2)}} \tag{7.14}$$

  (Wikipedia (2015b)).

- Dekker's Method, a method that combines the bisection method with the secant method. The secant method is defined as

  $$x_{n+1} = x_n - f(x_n)\frac{x_n - x_{n-1}}{f(x_n) - f(x_{n-1})} \tag{7.15}$$

  and can be seen as an approximation of Newton's method. In the first step we use the solution of the previous time step as the value for x_{n-1}. Dekker's method chooses the best iterate from the bisection and the secant method under some restrictions (Wikipedia (2016b)).

During the simulation we found a time at which Newton's method converged so slowly that no solution could be found. In Figure 7.7 the iteration points are shown, which show that due to the slope of the function the iterates are jumping from one side to the other, but do not get close to the root fast enough. The Newton's method will therefore not be used in the calculation of the growth rate.

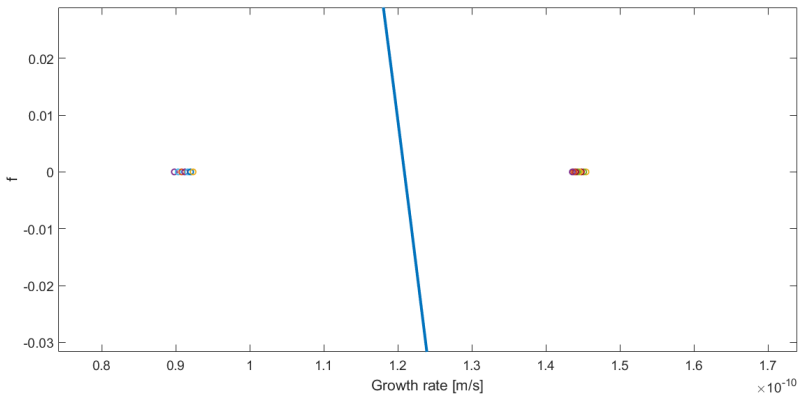

Figure 7.7: Newton iteration that fails after a maximum number of iterations.

We compare the three root finding methods that are left by running the simulation 5 times for each method and look at the average computation time of each method in Table 7.2.

Method	Run 1 (s)	Run 2 (s)	Run 3 (s)	Run 4 (s)	Run 5 (s)	Average
Bisection Method	118	117	116	116	116	116.6
Ridders' Method	58	61	75	67	66	65.4
Dekker's Method	118	116	113	112	112	114.2

Table 7.2: Computation times of a 100,000 seconds simulation using different root finding methods for the growth rate.

It shows that the Ridders' method is by the far the fastest method of the three root-finding methods. The bisection and the Dekker's method give comparable results. Looking at the number of times the Dekker's method choose the secant iterate over the bisection iterate, we find 0. Meaning that the Dekker's method actually reduces to the bisection method in our simulation and therefore gives comparable results to the single bisection method. Using the Ridders' method, we find the growth rates as given in Figures 7.8a and 7.9a at respectively $t = 0$ s and at $t = 100,000$ s.

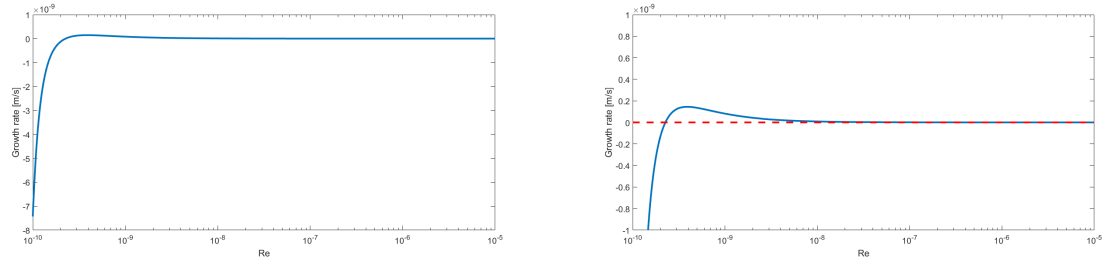

(a) The growth rate at the cell edges.

(b) The growth rate at the cell, zoomed in.

Figure 7.8: The growth rate at the cell edges at time is zero on different axes.

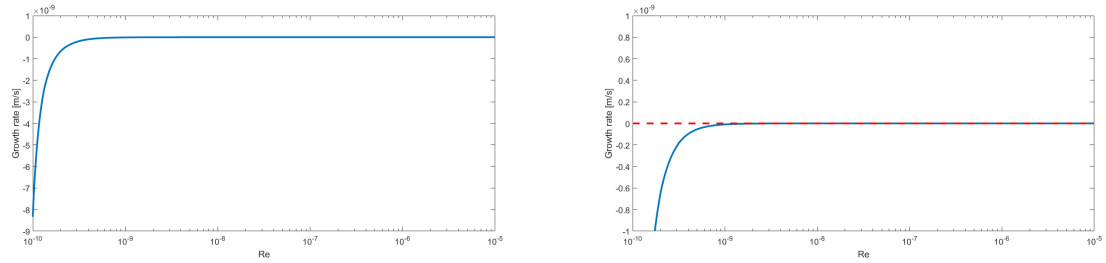

(a) The growth rate at the cell edges.

(b) The growth rate at the cell edges, zoomed in.

Figure 7.9: The growth rate at the cell edges at time is 100,000 s on different axes.

When the concentrations of the elements in the precipitate are near their equilibrium concentration, coarsening takes places, i.d. the growth of large precipitates at the expense of small precipitates. The driving force for coarsening is the reduction of the interfacial energy and thereby the total free energy. By the growth of large precipitates and the disappearance of small ones the total interfacial area is reduced, which reduces the free energy. In the model by Zurob et al. (2002), an artificial coarsening function is introduced to capture this phenomenon, based on assumptions about the coarsening regime. However, in the distribution model presented in this work, the coarsening mechanism is naturally incorporated. The growth rate captures this mechanism: precipitates with a radius corresponding to a positive growth rate will grow and precipitates with a radius corresponding to a negative growth rate will dissolve. In Chapter 8 the differences in the precipitate number density as well as in the precipitate mean diameter will be given, using the artificial coarsening function in the mean radius approach by Zurob et al. (2002) and the naturally incorporated coarsening in the distribution approach by Kampmann and Wagner (1991).

Going back to the growth rates found in Figures 7.8a and 7.9a at respectively $t = 0$ s and at $t = 100,000$, we are mostly interested in the radius at which the growth rate equals zero, since this indicates the switch between growth or dissolution. To get a better view on the positive growth rates corresponding to growth of the precipitates, we adjust the vertical axis and find Figures 7.8b and 7.9b. We find that the radius at which the growth rate equals zero increases, meaning that the switch between growing and dissolving moves to larger precipitates. This is as expected since the growth rate involves a $1/R$ term, leading to a smaller growth rate v for a larger radius R. The maximum value of the growth rate will decrease over time, since the concentration of niobium in the matrix decreases. This is confirmed by the height of the bump in Figures 7.8b and 7.9b, the highest value of the growth rate after 0 seconds lies around 0.2×10^{-9} whereas the highest value is 1.3134×10^{-12} after 100,000 seconds.

7.3. Critical radius

During simulation we found that Newton's method would sometimes return a complex number for the critical radius. It was unclear if this is caused by a numerical implementation error, or no critical radius should actually be found due to the physical condition of the system. To find out, we look at the behavior of $\frac{d(\Delta G)}{dR}$ (Equation (3.18)) for different values of the chemical energy Δg_v, since we expect this variable will influence the behavior of the function. We distinguish two cases: $\Delta g_v < 0$ and $\Delta g_v > 0$. This first case is the most common one in publications and in the situation of nucleation and precipitate growth. The second case is less frequent investigated and could occur for example when we deal with a under-saturated system for instance after a sudden temperature rise. In the case of a positive chemical energy, no nucleation should take place, but dissolution of the precipitates.

In Figure 7.10a we plot the value of $\frac{d(\Delta G)}{dR}$ for negative values of Δg_v varying between -2.1298×10^9 (Δg_v at time is zero for our simulation) and 0. It seems that for some values we do find a root (which corresponds to the critical radius for that specific Δg_v) and for some value we do not. However, zooming out far enough in Figure 7.10b we see that there does exist a root, but at a very large radius. When using Newton's method it occurred that the initial value was taken too small and the method would converge to the minimum at the left side of the function, instead of converging to the far right root. Adjusting the initial value in this case would be appropriate.
In Figure 7.11 we plot the value of $\frac{d(\Delta G)}{dR}$ for values of Δg_v varying between 0 and 2.1298×10^9 ($|\Delta g_v|$ at time is zero for our simulation). As we said before, no nucleation should take place and therefore we also expect to find no root. Figure 7.11 confirms this as there are no roots for the function for any value of $\Delta g_v > 0$.
Using this information, we adjust our algorithm of finding the critical radius. In Figure 7.13, a flowchart is given, which describes the new process. We use that there exists a root when the function has a maximum and a minimum (first derivative of the function, i.e. the second derivative to R, equal to zero).

7.3.1. New computation time

Combining all improvements described in this chapter and optimising the code lead to a great reduction of the computation time. We ran the simulation for the $NbCN$ precipitate, without multi-component or multi-precipitate extension. Before the adjustments it took around 240 seconds to calculate 10 simulation seconds, whereas now it takes around 21 seconds to calculate 100,000 simulation seconds[1].

[1] For the simulation we use MATLAB 2016b on Windows®

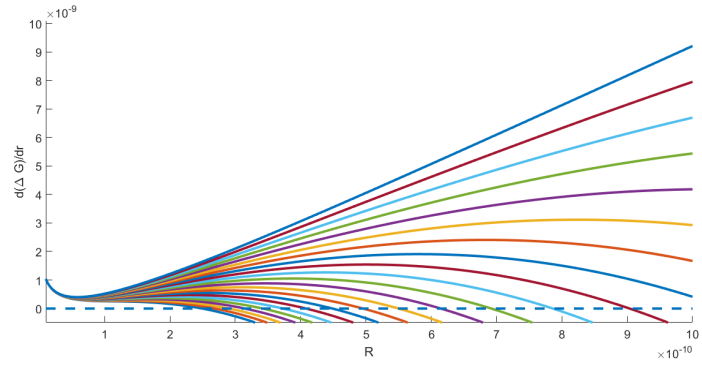

(a) Negative Δg_v.

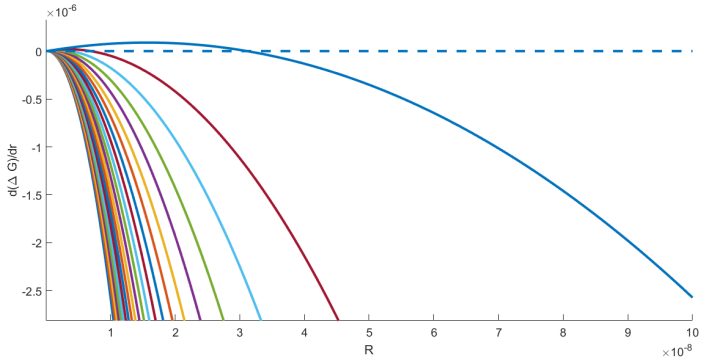

(b) Negative Δg_v (zoomed out).

Figure 7.10: Value of $\frac{d(\Delta G)}{dR}$ for negative values of Δg_v varying between -2.1298×10^9 and 0. The lines correspond to decreasing values of Δg_v looking from the top line to the bottom line, where the top line corresponds to $\Delta g_v = 0$ and the bottom line corresponds to $\Delta g_v = -2.1298 \times 10^9$.

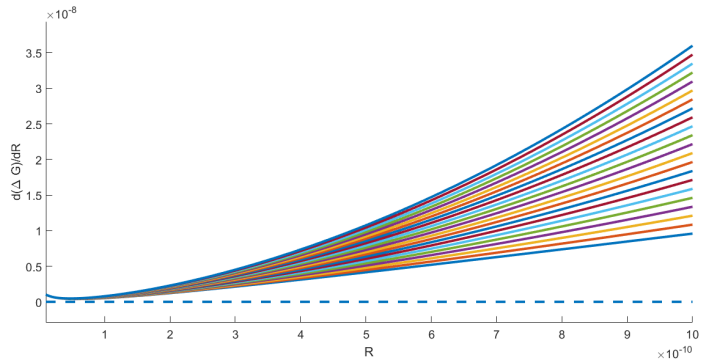

Figure 7.11: Positive Δg_v.

Figure 7.12: Value of $\frac{d(\Delta G)}{dR}$ for positive values of Δg_v varying between 0 and 2.1298×10^9. The lines correspond to decreasing values of Δg_v looking from the top line to the bottom line, where the top line corresponds to $\Delta g_v = 2.1298 \times 10^9$ and the bottom line corresponds to $\Delta g_v = 0$.

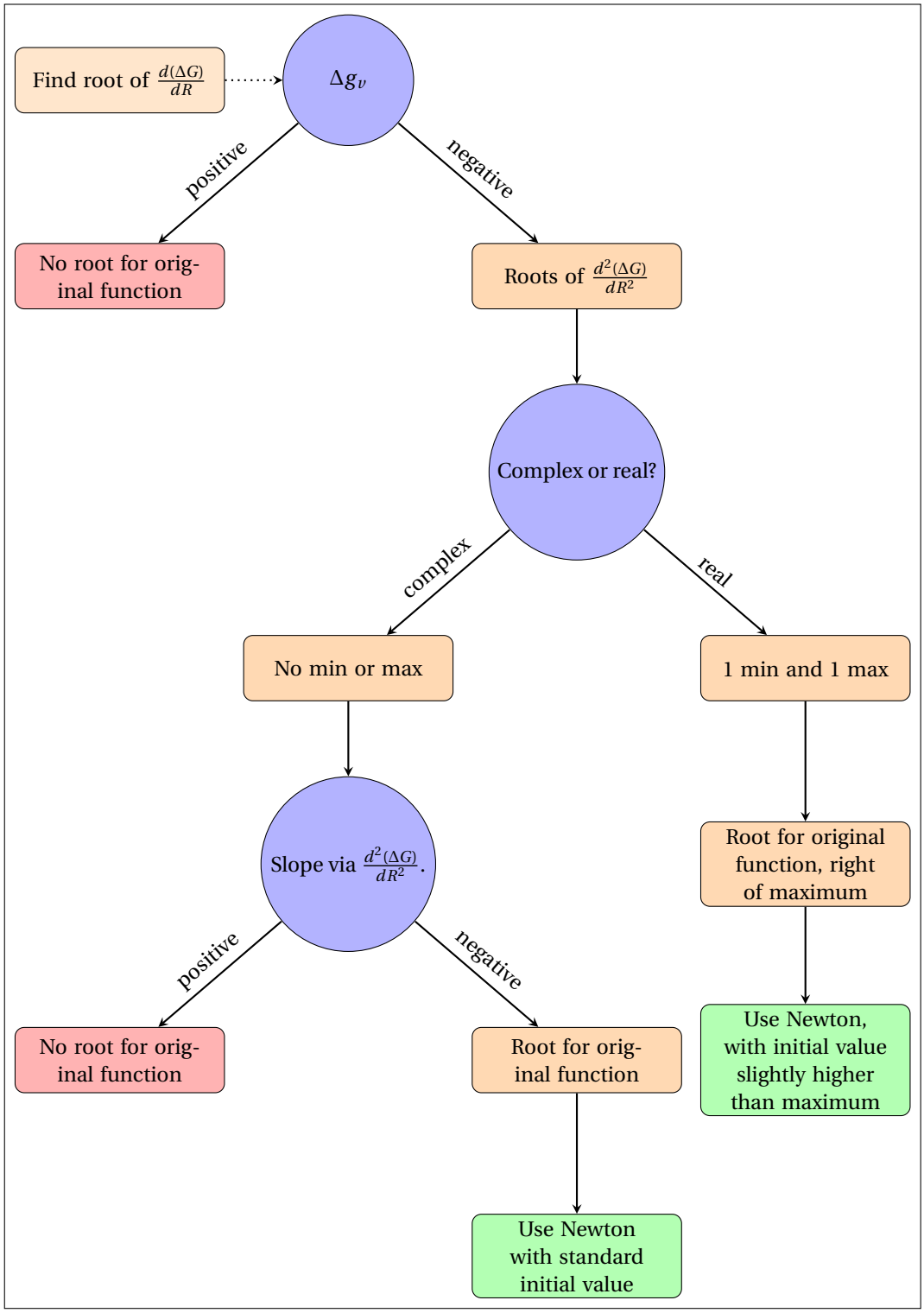

Figure 7.13: Flowchart concerning the calculation of the critical radius.

II

Simulations and numerical results

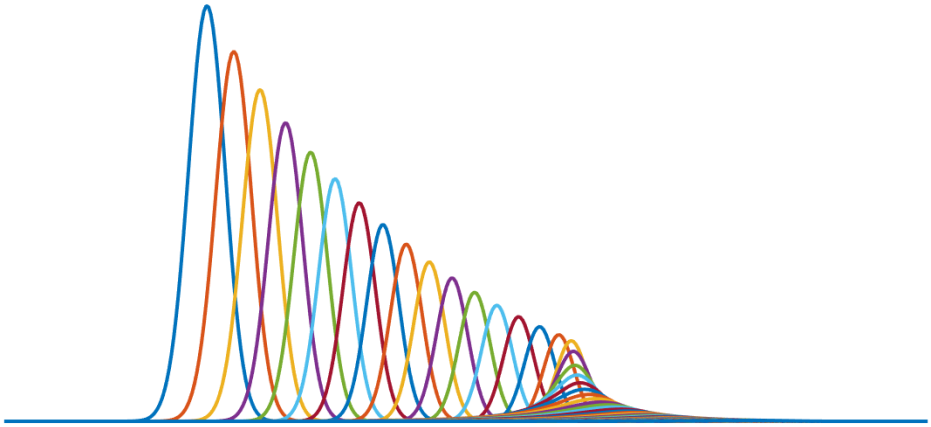

8

KWN model

To verify the quantitative and qualitative behavior of the distribution approach introduced in Chapter 3, we compare the results for the precipitate number density and precipitate mean diameter to the results obtained using the models from Kranendonk (2005) and Vonk (2016), both based on the mean radius approach by Zurob et al. (2002). For the comparison we use the configuration of the parameters given in Table 8.1 (precipitation parameters[1]), Table 8.2 (numerical parameters of which the meanings can be found in the nomenclature at the end of this thesis) and Table 8.3 (the composition of the alloy used).

The composition of the alloy used in simulations by Zurob et al. (2002) and Kranendonk (2005) is equal to the one used in this thesis, except from the initial weight percentage of Al. Zurob et al. (2002) and Kranendonk (2005) used an initial weight percentage of 0 for Al, but because we would like to simulate AlN precipitates in future chapters, we choose a slightly higher value of 0.01. This will not have a large influence on the results obtained for the $NbCN$ precipitates since no multi-component mechanisms are used yet.

Table 8.1: Precipitation parameters used in the simulations.

Parameter	Value	Unit
T	1123.15 (850 °C)	K
R_g	8.31441	J/(K mol)
ρ	3.27×10^{14}	$1/m^2$
k_B	1.38×10^{-23}	J/K
ν	0.293	
F	1.32×10^{-3}	
N_a	6.022142×10^{23}	1/mol
$v_{m,NbC}$	13.39×10^{-6}	m^3/mol
$v_{m,NbN}$	12.72×10^{-6}	m^3/mol
b	2.53144×10^{-10}	m
$N(0)$	0	$1/m^3$
$R(0)$	R^*	m

Table 8.2: Numerical parameters used in the simulations.

Parameter	Value	Unit
Δt_{start}	1×10^{-3}	s
α	2	
β	3/2	
t_{start}	0	s
t_{end}	100,000	s
percentage	0.05	%

Table 8.3: Alloy composition of alloy N1 used in the simulations in weight percentages.

C	Si	Mn	P	S	Nb	Al	N	Fe
0.076	0.06	1.34	0.0058	0.0026	0.03	0.01	0.0061	98.4695

In the simulations done by Kranendonk (2005) and Vonk (2016), it was assumed that precipitation only takes place at dislocations, the system was supersaturated and no precipitates were present at the start of the simulation ($N(0) = 0$). We use a zero vector for ϕ at time is zero for the distribution approach, which is equivalent

[1] The temperature, time and composition dependent parameters are found in Appendix B.

to $N(0) = 0$ because of the definition of the precipitate number density:

$$N(t) = \int_0^\infty \phi(R,t)dR. \tag{8.1}$$

To fairly compare the obtained results we do not use the adjusted critical radius initiated in Chapter 7, but the old approximation by Zurob et al. (2002) of $1.05R^*$. The other improvements initiated in that chapter were just to improve the computation time and will therefore be used.

8.1. Comparison of results to Kranendonk (2005) and Vonk (2016)

The comparison between the three models, the distribution model by Robson (2014), the mean radius model by Kranendonk (2005) (Tata Steel) and the mean radius model by Vonk (2016), is given below and the results, both the precipitate number density as well as the precipitate mean diameter, are given in Figure 8.1.

- Approach
  - **Vonk (2016)**: Mean radius approach (Zurob et al. (2002)) with Backward Euler.
  - **Kranendonk (2005)**: Mean radius approach (Zurob et al. (2002)) with Runge-Kutta 4.
  - **This work**: Distributions approach (Robson (2014), Den Ouden et al. (2013)) with Backward Euler.
- Calculation interface concentration
  - **Vonk (2016)**: Variable C and N interface concentration.
  - **Kranendonk (2005)**: C and N interface concentration equal to their matrix concentration.
  - **This work**: Variable C and N interface concentration.
- Differential equations during coarsening
  - **Vonk (2016)** - (based on Deschamps and Brechet (1999)):

$$\frac{dR}{dt} = \frac{4}{27}\frac{C_{Nb}^{Eq}}{C_{Nb}^{P} - C_{Nb}^{Eq}}\frac{R_0 D_{bulk}}{R^2}, \tag{8.2}$$

$$\frac{dN}{dt} = \frac{1}{R}\frac{dR}{dt}\left(\frac{R_0 C_{Nb}^{M}}{R(C_{Nb}^{P} - C_{Nb}^{M})}\left(\frac{3}{4\pi R^3} - N\right) - 3N\right). \tag{8.3}$$

  - **Kranendonk (2005)** - (based on Zurob (2003)):

$$\frac{dR}{dt} = \frac{D_{eff}}{R}\frac{C_{Nb}^{R} - C_{Nb}^{R27/23}}{C_{Nb}^{P} - C_{Nb}^{Eq}}, \tag{8.4}$$

$$\frac{dN}{dt} = \frac{1}{R}\frac{dR}{dt}\left(\frac{R^* \ln\left(\frac{wt\%Nb^{M}}{wt\%Nb^{Eq}}\right) C_{Nb}^{M}}{R(C_{Nb}^{P} - C_{Nb}^{M})}\left(\frac{3}{4\pi R^3} - 2N + \frac{4}{3}\pi R^3 N^2\right) - 3N\right). \tag{8.5}$$

  - **This work**: Coarsening is not defined in distribution approach, but is naturally incorporated.

Looking at the results obtained in Figure 8.1, it seems that the model by Vonk (2016) has a mismatch in the precipitate density and a lower precipitate diameter at long times, expected to be caused by a different coarsening regime. Comparing the coarsening regime of Vonk (2016) and Kranendonk (2005), we find two main differences: the use of a effective diffusion coefficient in Kranendonk (2005) compared to a bulk diffusion coefficient in Vonk (2016), and the equations in general. We apply two adjustments and compare the results. The first adjustment is the use of the effective diffusion coefficient in the growth rate in the coarsening regime and the second adjustment is the use of the differential equations from Kranendonk (2005) for the precipitate diameter R and the precipitate density N in the coarsening regime, which also uses the effective diffusion coefficient. This gives the results found in Figure 8.2.

We find that both adjustments give the desired result, as the mismatch in the precipitate density and precipitate mean diameter is decreased. We suspect that the use of the effective diffusion coefficient has a large influence on the results, despite of the equations used in the coarsening regime. To confirm this expectation we also plot the precipitate number density and precipitate mean diameter in Figure 8.3, using the bulk diffusion coefficient in both descriptions (Vonk (2016) and Kranendonk (2005)). We indeed find that the use of the bulk diffusion coefficient in the equations for the coarsening regime by Kranendonk (2005) gives the same results as when using the bulk diffusion coefficient in the equations for the coarsening regime by Vonk (2016). We conclude that the descriptions of the coarsening regime, by Kranendonk (2005) and Vonk (2016), give the same results and in general agree with the results obtained using the distribution model, as long as the (same) effective diffusion coefficient is used. When the precipitates on dislocations and on grain boundaries have grown since nucleation, they also take up elements from the bulk. Using an effective diffusion coefficient for growth on dislocations and growth on grain boundaries is therefore well substantiated and we may safely assume that the results obtained using the distribution model are correct and describe the coarsening regime well. This conclusion is shared by Perez et al. (2008), who also verified that the distribution approach gives correct results.

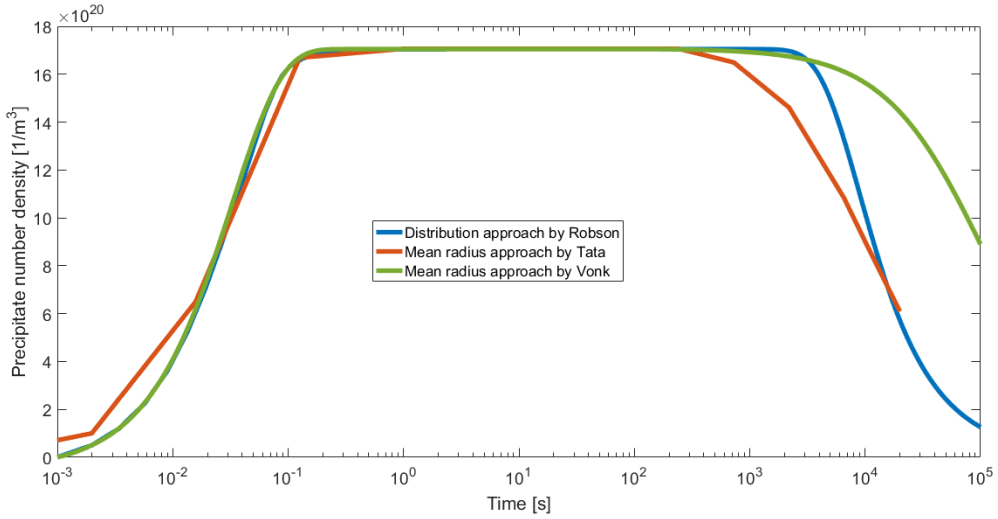

(a) Precipitate number density.

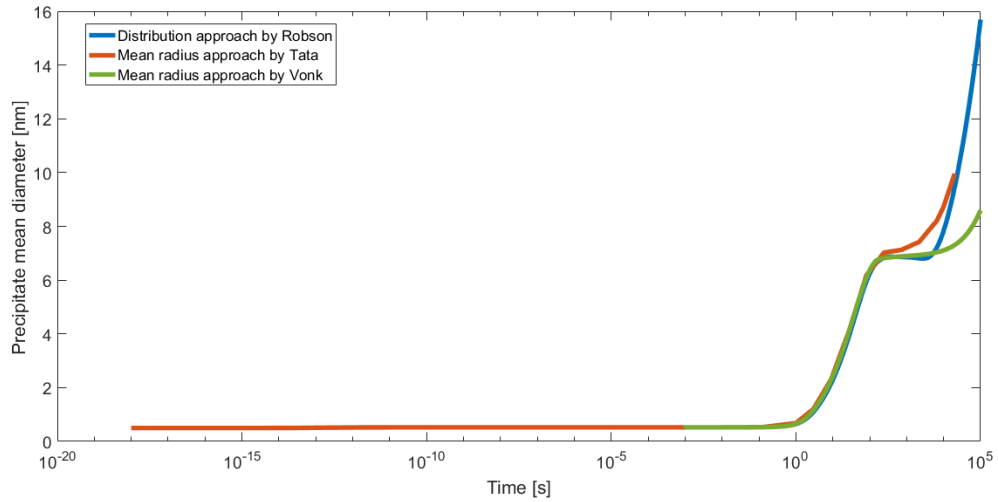

(b) Precipitate mean diameter.

Figure 8.1: Simulation results with distribution approach by Robson (2014) using Backward Euler compared to simulation results with mean-radius approach from Zurob et al. (2002) by Kranendonk (2005) (Tata Steel) using Runge-Kutta 4 and the mean-radius approach from Zurob et al. (2002) by Vonk (2016) using Backward Euler.

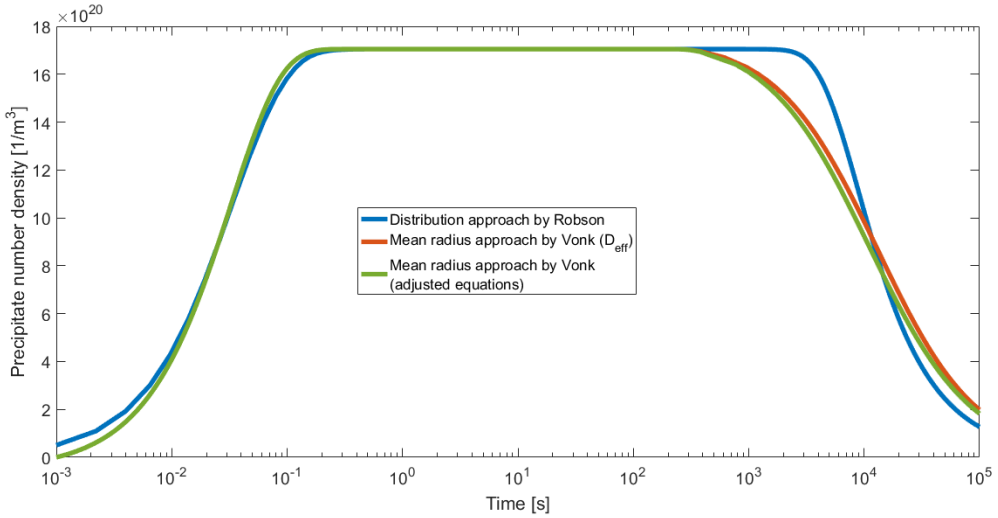

(a) Precipitate number density.

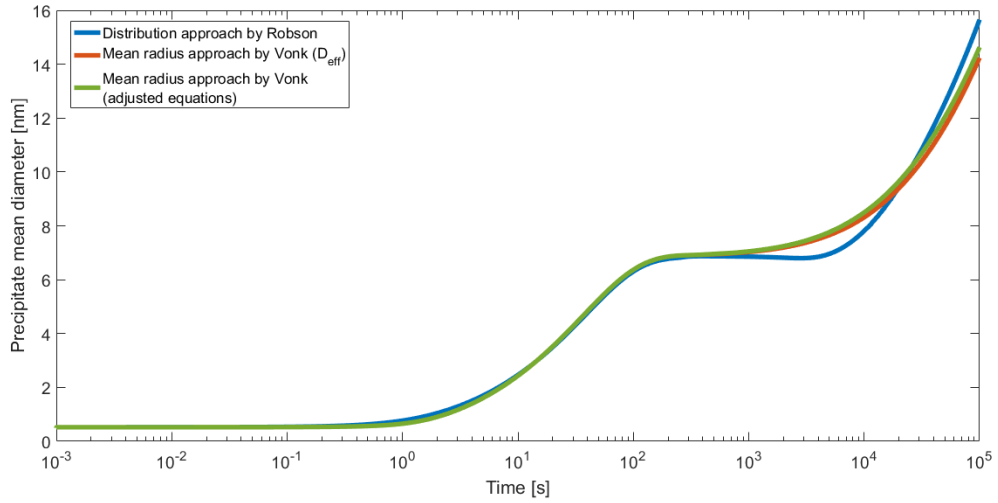

(b) Precipitate mean diameter.

Figure 8.2: Simulation results with distribution approach by Robson (2014) using Backward Euler compared to simulation results with mean-radius approach from Zurob et al. (2002) by Vonk (2016) using Backward Euler and an effective diffusion coefficient in the growth rate and the mean-radius approach from Zurob et al. (2002) by Vonk (2016) using Backward Euler and the differential equations during the coarsening regime from Kranendonk (2005).

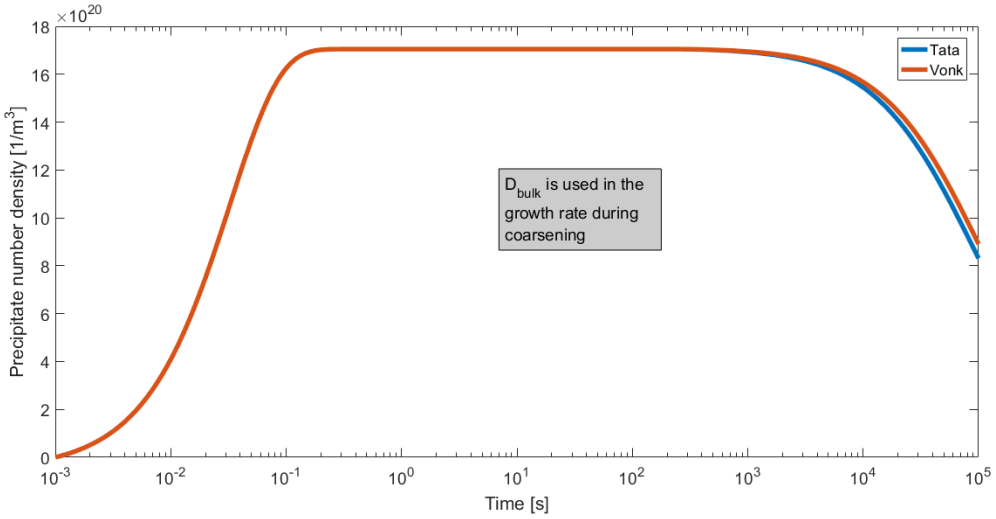

(a) Precipitate number density.

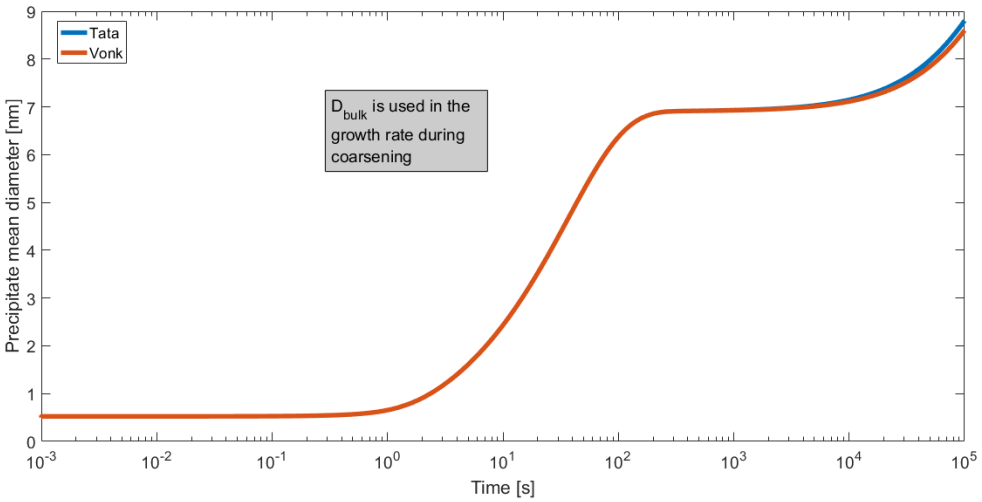

(b) Precipitate mean diameter.

Figure 8.3: Simulation results with the mean-radius approach from Zurob et al. (2002) by Kranendonk (2005) (Tata Steel) using Runge-Kutta 4 and the mean-radius approach from Zurob et al. (2002) by Vonk (2016) using Backward Euler. In both approaches we use the bulk diffusion coefficient in the growth rate in the coarsening regime.

8.2. Number density distribution

Now that we have verified that the results found using the distribution model follow the results found using the mean approach model and vice versa, we analyse the behaviour of the number density distribution during precipitation. In precipitation we can define four stages: nucleation: the appearance of precipitates from a supersaturated matrix, growth: the growing of the precipitates, coarsening: the growth of large precipitates at the expense of small precipitates and (partial) dissolving. This last stage only happens in special occasions and will therefore not be considered in this section.

As Zurob et al. (2002) noted, each stage has its own characteristics: during nucleation, the precipitate number density increases, during pure growth the number density stays constant and the mean diameter increases and finally during the coarsening stage the precipitate number density decreases, while the mean diameter increases. In Figure 8.4 we globally indicated the three different stages of precipitation in the plot of the precipitate number density as a function of the time. These characteristics can also be found in the number density distribution. We plot the distribution right after nucleation, during growth and during coarsening, in Figure 8.5.

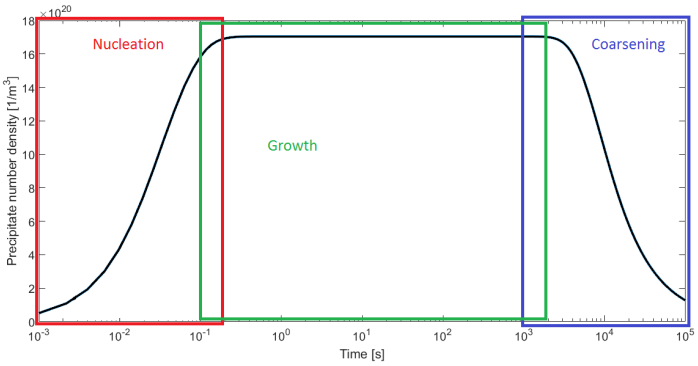

Figure 8.4: Illustration of different stages in precipitation.

Directly after nucleation (after 0.001 seconds, Figure 8.5a), the number density distribution has a large peak slightly right of the critical radius as expected, since the nucleated precipitates can only grow if their radius is slightly larger than the nucleation radius and are therefore added to a size class right of the critical radius (see Chapter 7).
During the second stage of precipitation, growth (Figure 8.5b), the peak of the number density distribution starts to move to the right, since the precipitate grow. In the figure it looks as if the total number of precipitates decreases, however if we look at the precipitates number density for these times in Table 8.4, the number of precipitates even slightly increases. This is because there is still some nucleation and not just pure growth.
As described in Chapter 3, coarsening is naturally incorporated in the distribution model. Looking at the change of the distributions during the coarsening stage in Figure 8.5c we find that both the height of the peak, as well as the width of the peak decreases, which indicates that the precipitate number density decreases. Table 8.5 confirms this and thereby shows that precipitates are dissolving. When we zoom in and indicate the maxima of the number distributions at the various times (Figure 8.5d), we see that the maximum is moving to the right, which shows that at the same time precipitates dissolve (number density decreases) and precipitates grow, i.e. coarsening takes place.

Table 8.4: The precipitate number density for different times during the growth stage of precipitation.

Time (s)	0.06	0.1367	0.2078	0.3740	0.6432
Precipitate number density ($\times 10^{21}$ 1/m^3)	1.5089	1.6551	1.6943	1.7041	1.7047

Table 8.5: The precipitate number density for different times during the coarsening stage of precipitation.

Time (s)	32782	33282	34282	36282	38782
Precipitate number density ($\times 10^{20}$ 1/m^3)	3.6541	3.6027	3.5041	3.3222	3.1195

Remarkably is also the change in the shape of the precipitate size distribution: just after nucleation the distribution looks like a delta-distribution, but when the precipitates grow the distribution is much more like a log-normal distribution. During the coarsening stage the distribution is quite similar to the predicted LSW distribution. Both log-normal and LSW distribution are non-symmetric but with a different skewness: the log-normal distribution has a sharp rise before the mode (the radius, at which the distribution has its maximum) and a long tail for radii larger than the mode, while the LSW distribution has a gentle slope for radii smaller than the mode and a steep drop to zero for radii larger than the mode. If size distributions can be measured accurately, the difference in skewness of the distributions also suggests that by comparing the experimental and simulated distribution an estimate can be made at what stage in the precipitate evolution a material was at the end of a temperature scheme.

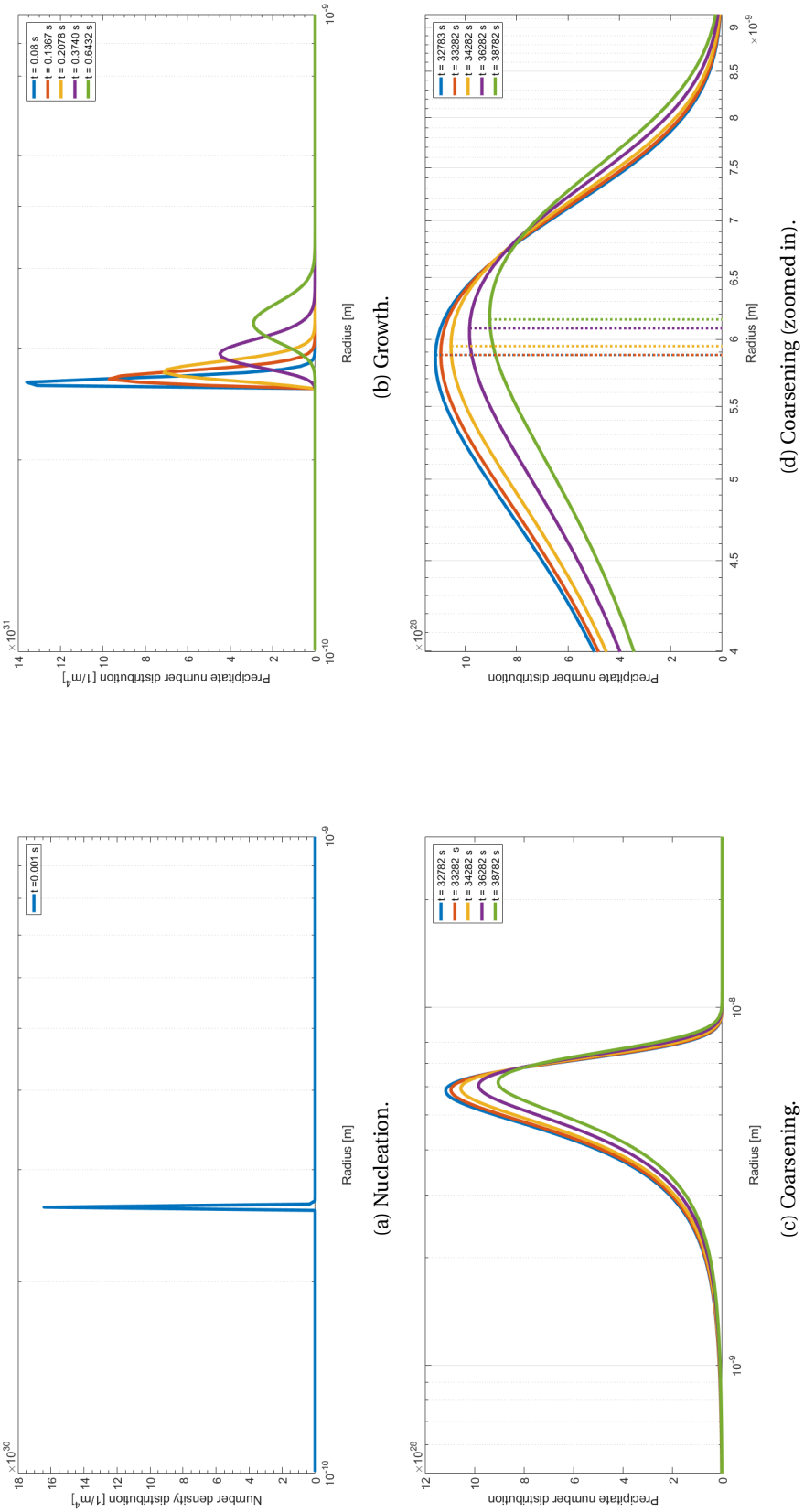

(a) Nucleation. (b) Growth. (c) Coarsening. (d) Coarsening (zoomed in).

Figure 8.5: The number density distribution during the three stages of precipitation: nucleation, growth and coarsening. Note that the axes of the different plots vary, so no comparisons in the height of the peaks can be directly made.

8.3. PTT diagram

Now that we have implemented and tested the distribution model, we use the results of a set of temperatures to construct a PTT (precipitation-time-temperature) curve, which involves the times when precipitation starts and finishes. This PTT curve can be used to adjust the processes of steel making. If one wants to optimise the precipitation in ferrite during annealing after cold rolling, precipitation in austenite during hot rolling should be minimised. A PTT diagram can give an indication of the minimum cooling rate during and after hot rolling to prevent or minimise precipitation in austenite for a specific composition. We construct the PTT curve, using the following steps and accompanying illustration in Figure 8.6.

- The volume fraction of precipitates as a function of time is calculated for a constant temperature. This is indicated in the top picture by the black line.
- Two times on this curve are selected: the time where the volume fraction is 5% of the equilibrium volume fraction and the time where the volume fraction is 95% of the equilibrium volume fraction. These criteria can differ per researcher, some choose 1% and 99% percent as start and end percentages respectively. In the top picture, the equilibrium volume fraction is indicated by the green line, and the 5% and 95% criteria by the red lines. If the time at which the volume fraction is exactly 5% or 95% of the equilibrium volume fraction is not available, interpolation is used to find the specific time.
- The previous step is repeated for various temperatures, in every step leading to two data points. These points are plotted in a time-temperature diagram, in which all the data points for the same equilibrium volume fraction percentage are connected with each other, giving two (black) curves as shown in the bottom picture.

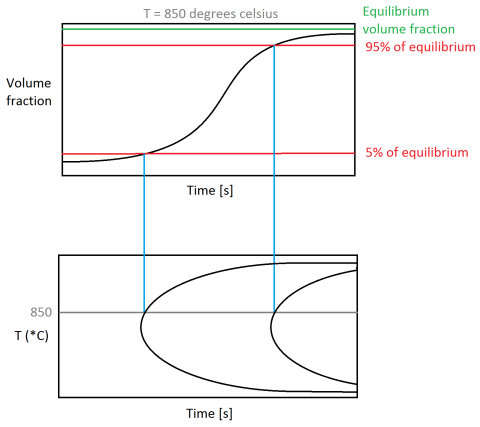

Figure 8.6: Illustration of the construction of a PTT curve.

If nucleation on grain boundaries and dislocations is considered, an additional first step is added: values for the grain size and dislocation density are chosen. During the simulation these quantities remain constant.

From literature we know that the temperature has an influence on both the activation energy and the diffusion coefficient, each with opposite effect: on one hand, increasing the temperature decreases the probability of forming new nuclei, which decreases the nucleation rate. On the other hand, increasing the temperature increases the diffusivity, making it easier to form new nuclei, which increases the nucleation rate.
In the literature study by Vonk (2016) a PTT diagram for nucleation on dislocations was constructed. The mean radius approach was used for this and we found an unexpected hard switch between the temperature at which the diffusion coefficient had a larger influence, to the temperature where the activation energy had a larger influence. This hard switch leads to a non-symmetrical shape of the PTT diagram, when using a linear time scale. In the literature most PTT diagrams are plotted using a base 10 logarithmic scale for the time axis. However, when using such a logarithmic time scale, we found the result to be even more non-symmetric, in contradiction to the symmetrical PTT diagrams found in literature. In the literature study by Vonk (2016) some possible cause were given:

- In the literature the data points at high temperatures are too sparse to estimate the correct trend as function of the temperature or these data points are not even present.
- A large error is made in the interpolation to find the time at which 5% and 95% of the equilibrium volume fraction is reached.
- The mean radius approach gives inaccurate results for the PTT diagram.

To check if the problem is caused by the usage of the mean radius approach, we construct the PTT diagram using the results of the distribution approach. The volume fractions for different temperatures are given in

Figure 8.7 and the resulting PTT diagram is given in Figure 8.8. Again we find the non-symmetrical shape in the PTT diagram on the linear time axis and an even more non-symmetrical shape in the PTT diagram using the a base 10 logarithmic time scale. The PTT diagram seems to exist of two parts, the part above 900 °C and the part below 900 °C. Each of these two parts has a parabolic shape (despite the time scale), but the two parts do not fit together, specifically the curve belonging to the 95% of the equilibrium volume fraction. We may conclude that this effect is not caused by the choice of modelling approach (mean radius or distribution approach). Other causes described above are still possible. In Chapter 10, we also construct the PTT diagrams for nucleation on grain boundaries and for homogeneous nucleation to see whether we find similar non-symmetrical diagrams or if we find more symmetrical results.

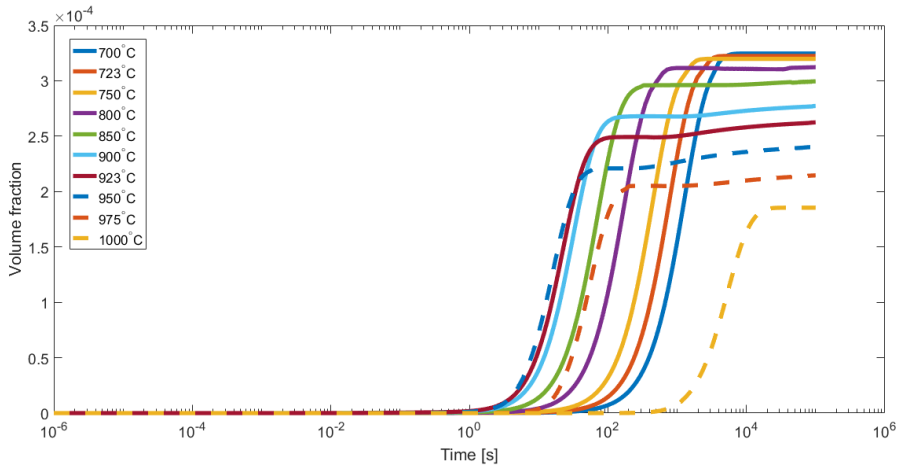

Figure 8.7: Volume fraction in time for different temperatures using the distribution approach on dislocations.

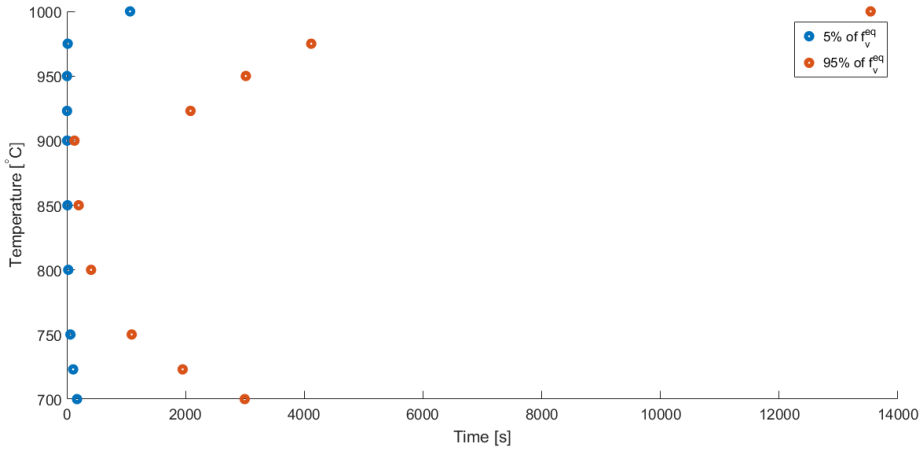

(a) Precipitate-time-temperature curve on a linear time scale.

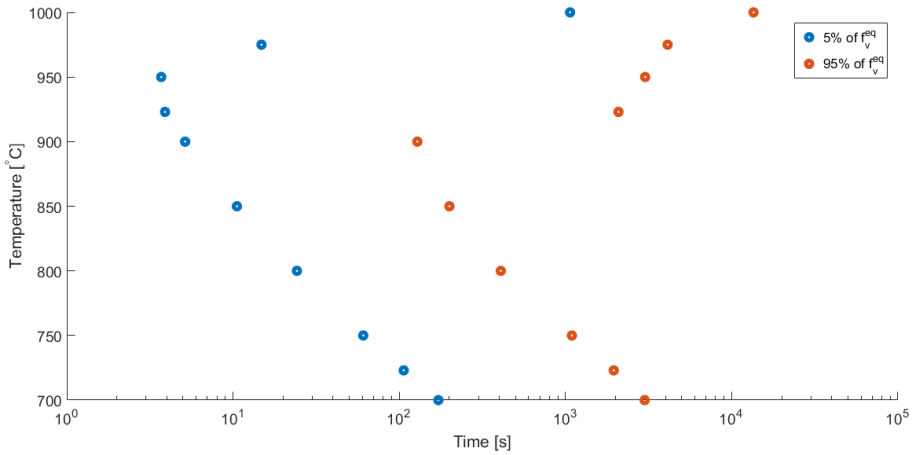

(b) Precipitate-time-temperature curve on a logarithmic time scale.

Figure 8.8: The precipitate-time-temperature curve using the distribution approach on dislocations.

9

Multi-component KWN model

All elements in the system influence the nucleation and growth of the precipitates, even when the elements do not participate in the precipitate. The growth rate for example is influenced by the diffusion coefficients and concentrations of all elements in the system. The binary KWN model as described in Chapter 3 did not include the influence of non-precipitate elements on the system. In this thesis an extension of the model was made, such that the influence of all elements is taken into account when simulating the nucleation and growth of precipitates. For the details on this model we refer to Chapter 4. This multi-component model was implemented, of which the results can be found in this chapter.

For all simulations in this chapter, we use the matrix composition before precipitation and other initial and numerical values as described in Chapter 8. To correctly analyse the effect of the adjustments we make to the original model, we adjust the model step by step. The first adjustment is taking into account other elements in the system and not only the elements in the precipitate during the calculations of the concentrations. We refer to Sections 4.1 and 4.2 for the details of these adjustments. Implementing the adjustments in the calculation of the concentration gives the results presented in Figure 9.1. The multi-component version of $Z\beta^*$ as described in Section 4.1 is not yet used. The results show that there is very little influence from the adjustment made in the calculation of the concentrations.

When we also implement the adjusted approximation for the Zeldovich factor Z and the rate of atomic attachment β^* as described in Section 4.1, we find the results in Figure 9.2. Again, no large differences can be seen. For the simulations in this chapter we use a constant weight percentage for the elements that do not participate in the precipitate. In later chapters we will simulate combinations of precipitate compositions, leading to a varying weight percentages of multiple elements, possibly leading to more visible effects in the results caused by the multi-component mechanism in the model. Also, in the equation for β^* we use the diffusion coefficient along dislocations, since we believe the atoms move through the dislocation since diffusion along a dislocation is much faster than through the bulk:

$$\beta^* = \frac{4\pi(R^*)^2 D_{X,pipe} x_X^M}{a^4}. \tag{9.1}$$

However, one could also argue that the atoms move along the dislocation as well as through the bulk. This would lead to using an effective diffusion coefficient in the equation for β^*:

$$\beta^* = \frac{4\pi(R^*)^2 D_{X,eff} x_X^M}{a^4}. \tag{9.2}$$

If we use this description for the atomic attachment, we see that large differences occur between the basic binary KWN model and the adjusted multi-component KWN model[1] (Figure 9.3). To fit the model to experimental data, Zurob et al. (2002) uses 5 data points for the precipitate mean diameter. However, if we adjust the data fitting parameter F (in the simulation called F_{prec}) in a range of 0.01-0.02 in Figure 9.4, we note it has

[1] The choice of effective diffusion coefficient can also have a big influence on the results. For future work various descriptions of the effective diffusion coefficient could be tested and the results compared.

large influence on the precipitate density, but little influence on the precipitate mean diameter. This means that changing the fitting parameter such that the mean diameter fits the data points (or binary KWN model), can have a big influence on the precipitate number density.
Since we do not have experimental data on the precipitate number density, we can not draw any conclusion on the fitting. Zurob et al. (2002) uses an indirect approach to verify the values of the precipitate number density with reality. Via the recrystallisation and recovery model he retrieves the softening fraction. For the softening fraction, experimental data are available, and he could adjust the fitting parameter such that both the mean diameter and the softening fraction agree with the data. Since our model is not yet coupled to the recrystallisation and recovery models, the possibilities for validation are restricted. Therefore we use the model that agrees best with the model made by Zurob et al. (2002), the model with the pipe diffusion coefficient, since we know that this model agrees with the experimental on both the mean diameter and the softening fraction. For future work, more experimental work should be done on more variables, such that verification and data fitting of the model can be executed correctly.

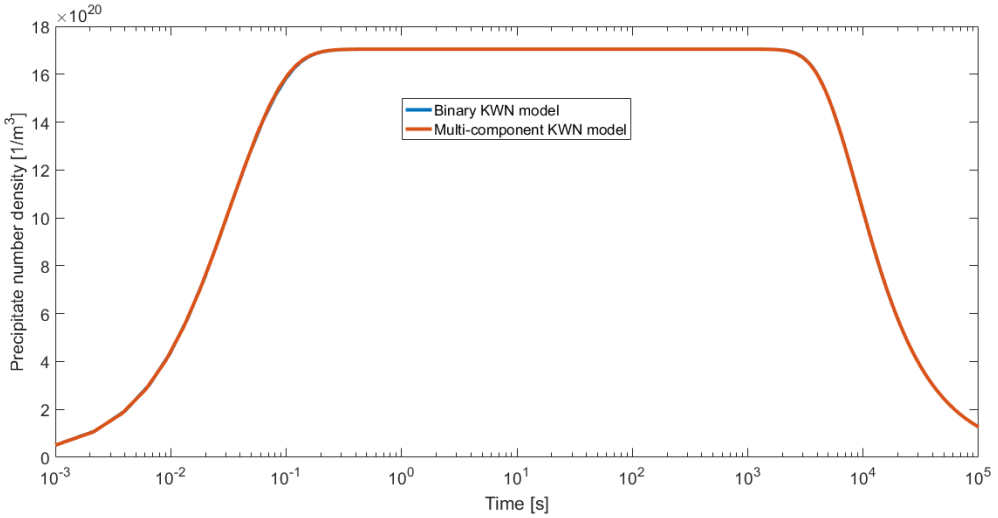

(a) Precipitate number density.

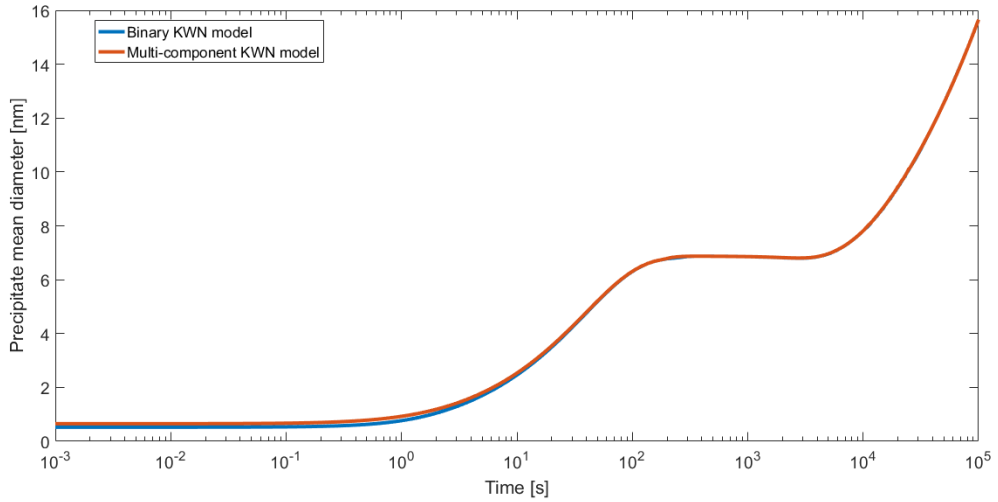

(b) Precipitate mean diameter.

Figure 9.1: Simulation results using the binary KWN model from Chapter 3 and the multi-component KWN model from Chapter 4 without the adjusted approximation for Z and β^*.

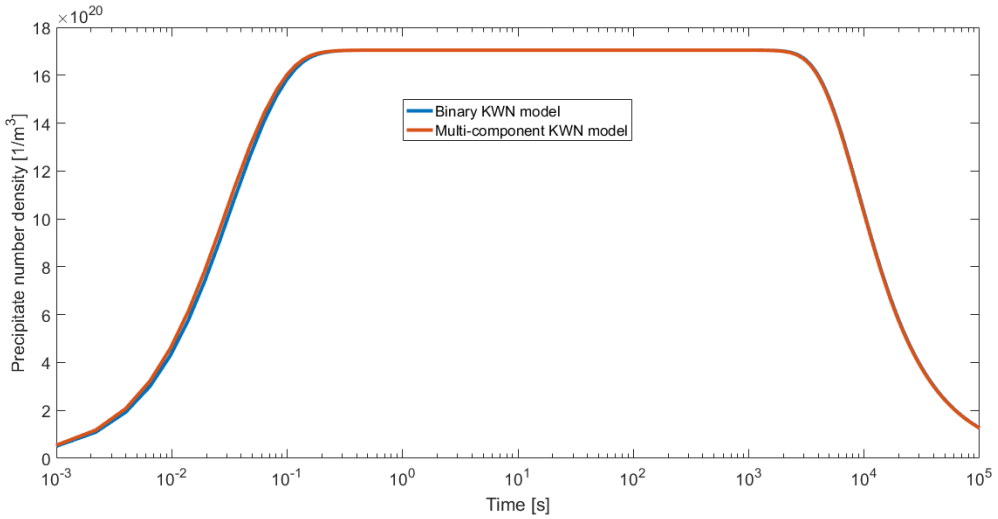

(a) Precipitate number density.

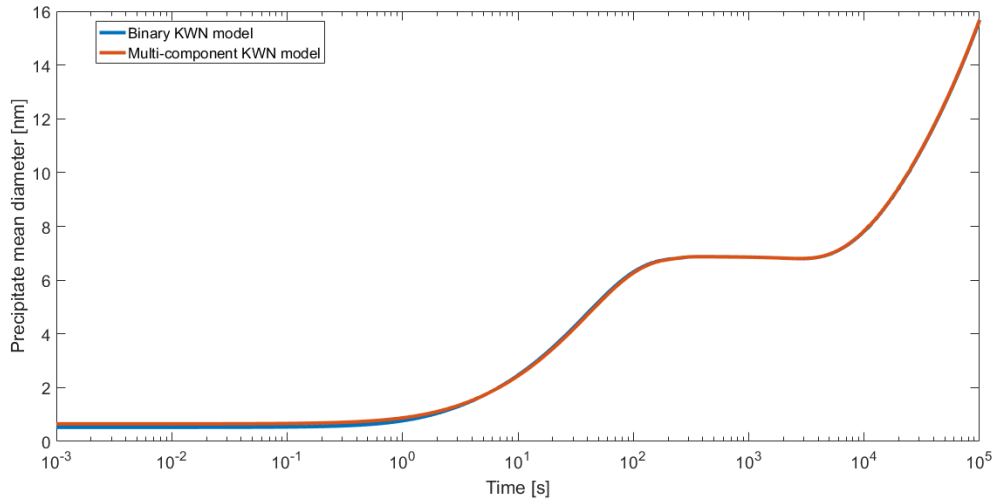

(b) Precipitate mean diameter.

Figure 9.2: Simulation results using the binary KWN model from Chapter 3 and the multi-component KWN model from Chapter 4 with the adjusted approximation for Z and β^* (based on D_{pipe}).

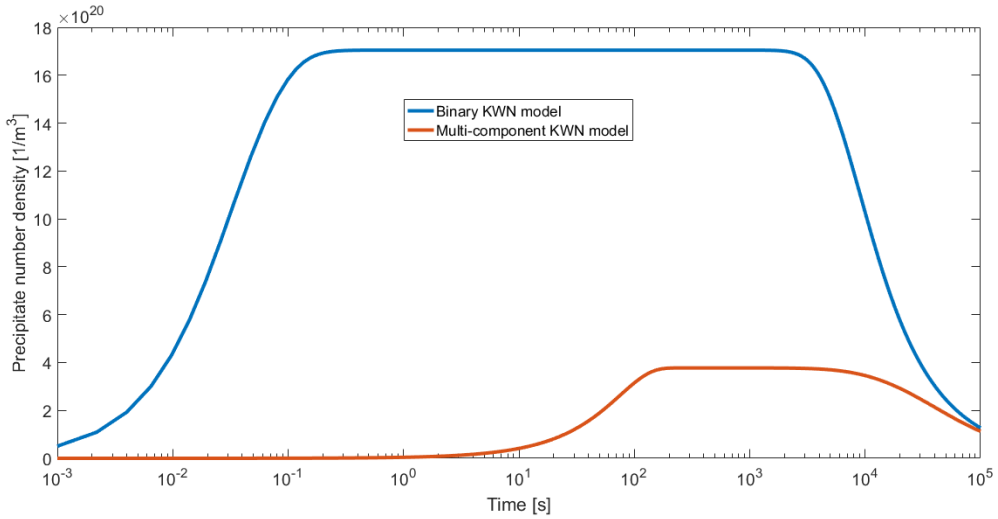

(a) Precipitate number density.

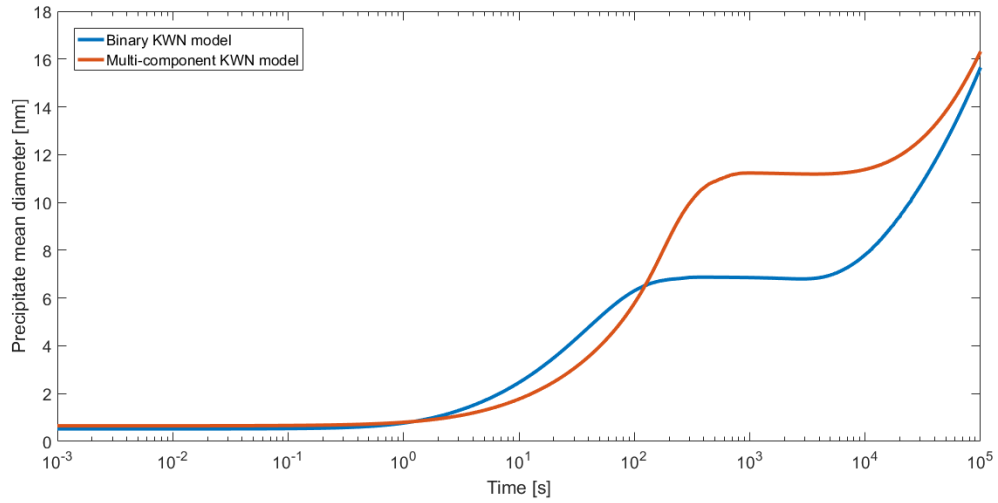

(b) Precipitate mean diameter.

Figure 9.3: Simulation results using the binary KWN model from Chapter 3 and the multi-component KWN model from Chapter 4 with the adjusted approximation for Z and β^* (based on D_{eff}).

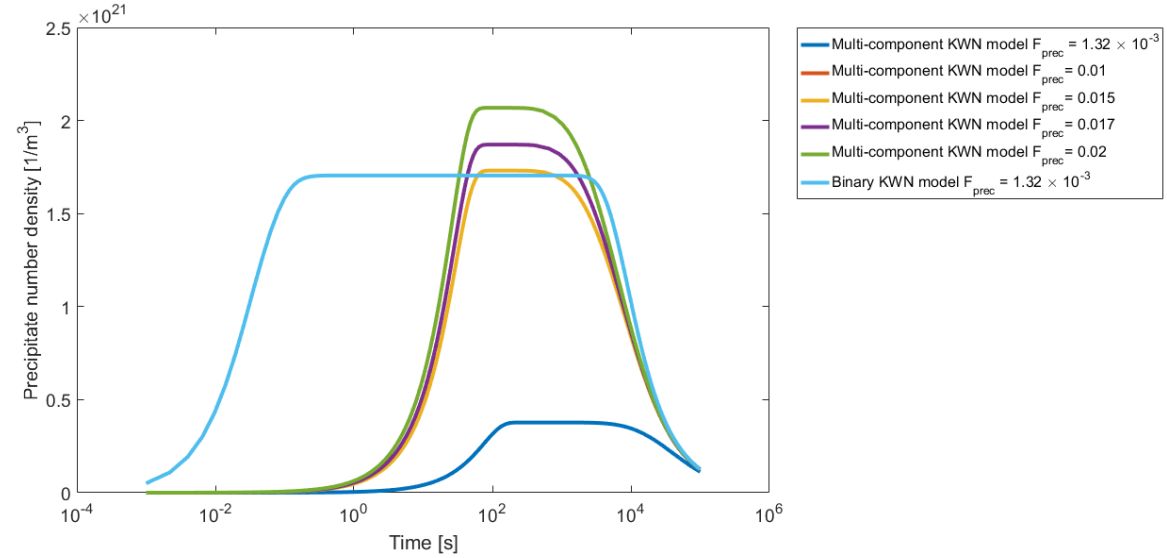

(a) Precipitate number density.

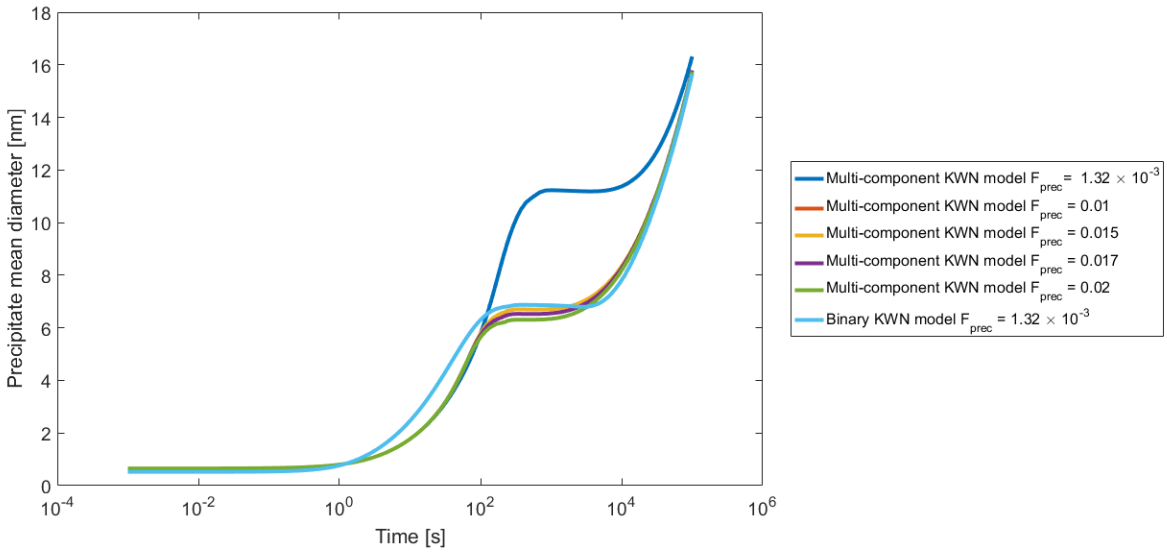

(b) Precipitate mean diameter.

Figure 9.4: Simulation results using the binary KWN model from Chapter 3 and the multi-component KWN model from Chapter 4 with the adjusted approximation for Z and β^* (based on D_{eff}) for various values of F_{prec}.

10

Multi-precipitate KWN model

Because most steel alloys frequently contain many alloying elements, different precipitates can occur simultaneously (for instance, $NbCN$, AlN, MnS). The multi-component KWN model was therefore extended to simulate multiple precipitates types at the same time. However, each of these precipitates can also nucleate at multiple sites, like dislocation, grain boundaries and in grains. Also incorporating this complexity to the model, lead to the so called multi-precipitate KWN model. For the details on this model we refer to Chapter 5.

Part of the multi-precipitate model is the implementation of nucleation on grain boundaries and homogeneous nucleation. Using these implementations, the PTT diagrams for nucleation on grain boundaries and homogeneous nucleation are constructed to compare to the PTT diagram for nucleation on dislocations given in Chapter 8. Thereafter, the results of the implementation of the complete multi-component, multi-precipitate model are given, with several combinations of precipitate compositions and nucleation sites to illustrate the possibilities of the model and the interaction between various precipitate compositions, various nucleation sites, and combinations. Also, we will introduce a non-isothermal time dependent temperature scheme influencing the model parameters through time and thereby the final results. Finally, we will simulate the dissolution of precipitates in a preheat furnace in the hot strip mill, by calculating the precipitate evolution during a (non-isothermal) time dependent temperature scheme for such a furnace.

For the simulations in this section we use the matrix composition before precipitation and other initial and numerical values described in Chapter 8, completed with the values of the fitting parameters given in Table 10.1 and the varying parameters and equations described in Chapter 5. We use the value of the fitting parameter for dislocation also for the other two nucleation sites, since we have no experimental data available for nucleation on grain boundaries and homogeneous nucleation to fit the model to.

Table 10.1: Fitting parameters used in the simulations.

Parameter	Value
F_{dis}	1.32×10^{-3}
F_{gb}	1.32×10^{-3}
F_{hom}	1.32×10^{-3}

For each precipitate type (unique combination of precipitate composition and nucleation site) we give the results, consisting of the precipitate number density $N(t)$, the precipitate mean radius $\bar{R}(t)$, the volume fraction $f_v(t)$ and the saturation. Each of these variables is directly or indirectly derived from the number density distribution ϕ:

$$N(t) = \int_0^\infty \phi(R,t)\,dR \tag{10.1}$$

$$\bar{R}(t) = \frac{1}{N(t)} \int_0^\infty R\phi(R,t)\,dR, \tag{10.2}$$

$$f_v(t) = \int_0^\infty \frac{4}{3}\pi R^3 \phi(R,t)\, dR, \tag{10.3}$$

$$\text{saturation} = \frac{\text{matrix product}}{\text{solubility product}}, \tag{10.4}$$

where the matrix product is derived using the volume fraction, via Equation (5.7):

$$C_X^M = \frac{C_X^0 - \sum_{p\in\Theta} C_X^{P(p)} f_v^p}{1 - \sum_{p\in\Theta} f_v^p}. \tag{5.7}$$

10.1. PTT diagram

In Chapter 8, we constructed the PTT diagram for nucleation on dislocations (Figure 8.8). The PTT diagram had an unexpected non-symmetrical shape (using the distribution approach), which was also found by Vonk (2016) (using the mean radius approach). In Chapter 5, the description of the model for nucleation on grain boundaries and homogeneous nucleation was introduced, as part of the multi-precipitate model. Using these descriptions, we construct PTT diagrams for $NbCN$ precipitates with nucleation on grain boundaries and with homogeneous nucleation, to see whether also these nucleation sites give non-symmetrical PTT diagrams. The description of how to construct such a PTT diagram can be found in Section 8.3.

The temperatures chosen for the construction of the PTT diagram lie between the minimum temperature of austenite, since our model is currently developed for austenite simulations, and the solvus temperature. The solvus temperature depends on the composition of the precipitate, since it is found using the solubility product which is different for each precipitate composition. Also, the weight percentages of the elements participating in the precipitate are taken into account during the calculation of the solvus temperature. The solvus, but also on the initial weight percentages of the precipitate elements. For the initial alloy composition as described in Table 8.3, we find the following solvus temperatures for the different precipitate compositions. We use the $NbCN$ precipitate in the comparison of the different PTT diagrams for nucleation on dislocations, nucleation on grain boundaries and homogeneous nucleation.

	NbC	NbN	AlN	MnS	$NbCN$
T_{sol} (°C)	1030.1	1027.0	1017.7	1257.1	1093.9

Table 10.2: Solvus temperatures for the different precipitate compositions for alloy N1 (Table 8.3).

As described in Section 8.3, we know that the temperature influences the probability of nuclei forming, so does the diffusion coefficient, each with opposite effect on the nucleation rate. Increasing the temperature makes the probability of forming new nuclei smaller, which lowers the lower nucleation rate. On the other hand, increasing the temperature increases the diffusion coefficient, making it easier to form new nuclei, which increases the higher nucleation rate. In Figure 10.1 the volume fraction for different temperatures for nucleation on grain boundaries is given. We see a turning point at around 925 °C. Below this temperature, the influence from the diffusion coefficient is larger and the nucleation rate increases and after this point we find the influence from the activation energy is larger, leading to a lower nucleation rate. The switch between these situations is similar to the switch found for nucleation on dislocations.

Looking at the resulting PTT diagram in Figure 10.2, we find the same non-symmetrical shape for higher temperatures as found for nucleation on dislocations. We use a base 10 logarithmic time scale, since it is often used in literature. In agreement with the results found for nucleation on dislocations, the non-symmetrical shape is mainly caused by the 95% points, corresponding to the time at which the volume fraction is equal to 95% of the equilibrium volume fraction. The time at which the volume fraction of the 975 °C simulation reaches this 95% of the equilibrium volume fraction is even later than the time at which the volume fraction of the 1000 °C reaches the 95% of the equilibrium fraction, causing an even more irregular PTT diagram. When we zoom in on the evolution of the volume fraction in time for the 975 °C simulation, we find Figure 10.3 and note that there exists a small plateau in the volume fraction, instead of a constant increase (indicated by the arrow). The volume fraction at this plateau still increases, but due to the use of a logarithmic time scale

this results in a constant line. The naming 'plateau' therefore seems a bit ambiguous, but we will use it to easily refer to this part of the plot of the volume fraction. The slower increasing volume fraction (the plateau) postpones the moment at which the volume fraction reaches 95% of the equilibrium volume fraction. For the other temperatures in Figure 10.1, this small plateau also exists for all simulations, but the size differs. At lower temperatures the plateau seems to have vanished, but this is caused by the scale of the plot.

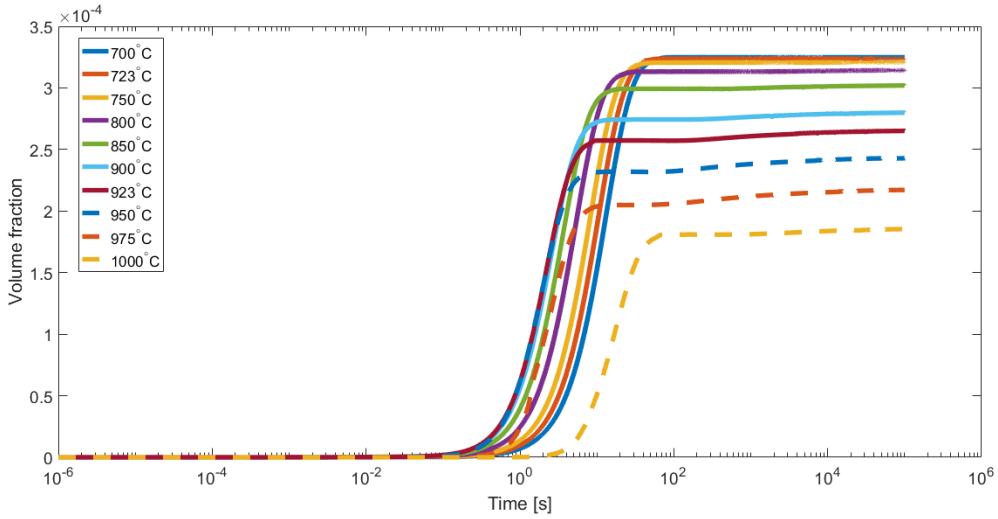

Figure 10.1: Volume fraction in time for different temperatures using the distribution approach on grain boundaries.

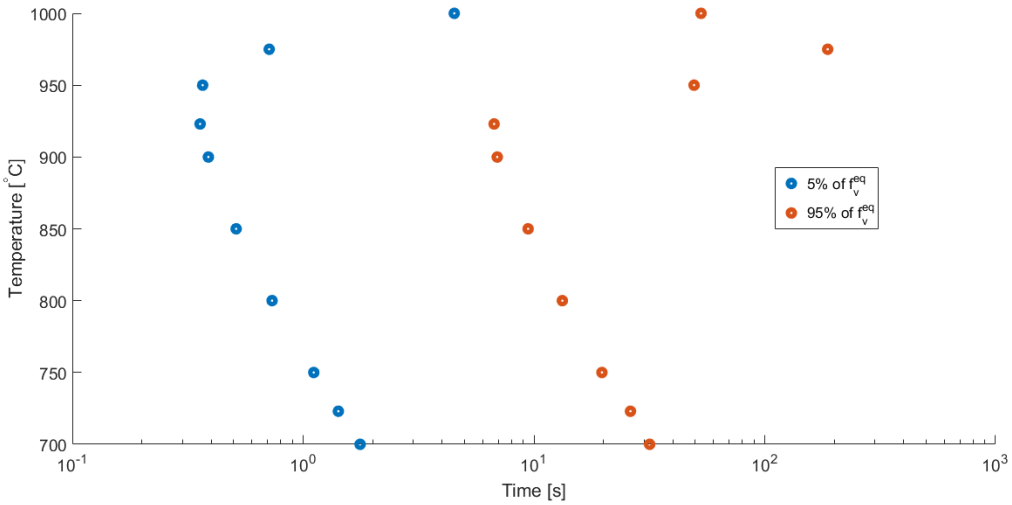

Figure 10.2: The precipitate-time-temperature curve using the distribution approach on grain boundaries.

The plateau in the volume fraction exists at the moment when nucleation has already stopped, but coarsening is not yet fully active, leading to a slower increasing volume fraction. It seems that the temperature influences the strength of this effect and thereby the size of the plateau. As stated in Section 8.3, some researchers use different reference percentages of the equilibrium volume fraction to construct the PTT diagram. They use 1% and 99% instead of respectively 5% and 95% used in this study. The shape of the PTT diagram might be influenced by this choice and would become more symmetric, since the effect of the plateau is decreased. However, when we plot the PTT diagram for multiple reference percentages in Figure 10.4, using the same 10 simulation temperatures as before, we find the same non-symmetrical shape for each reference percentage.

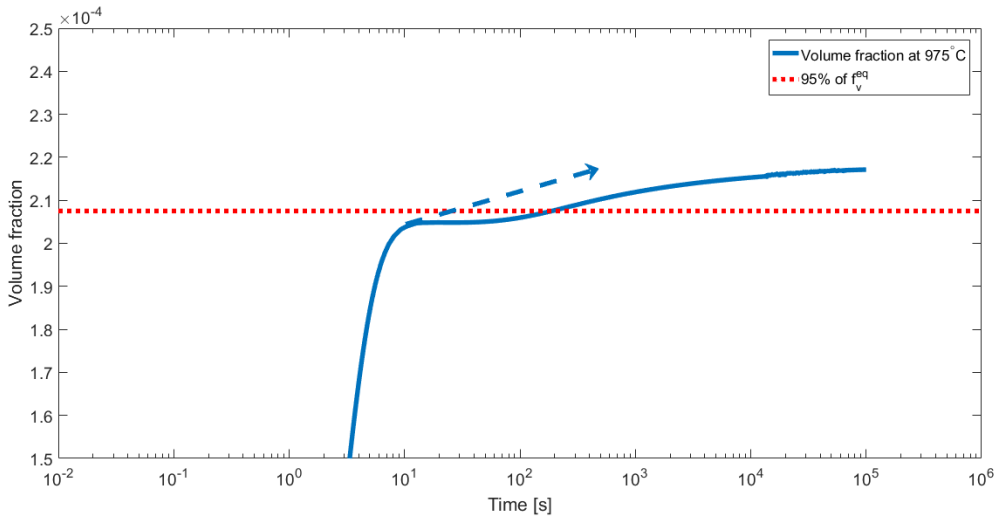

Figure 10.3: Volume fraction in time at 975 °C, zoomed in on the part where the volume fraction is close to 95% of the equilibrium volume fraction.

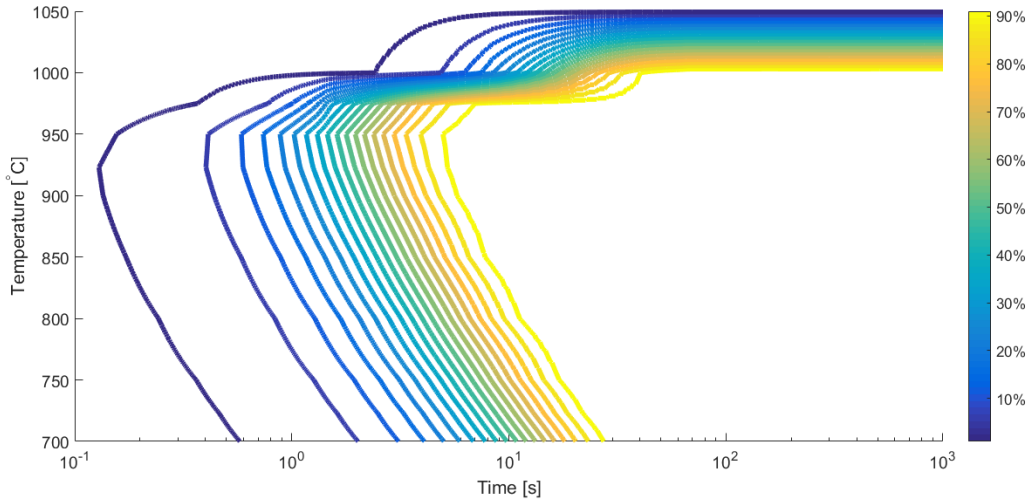

Figure 10.4: PTT diagrams for multiple percentages of the equilibrium volume fraction for nucleation on grain boundaries. The colours in the legend correspond to different percentages of the equilibrium volume fraction. For example 0.1 corresponds to 10% of the equilibrium volume fraction.

When plotting the PTT diagram for nucleation on dislocations using multiple percentages we find Figure 10.5. We find non-symmetrical shapes for the PTT diagrams for all percentages, as we expected from the earlier found PTT diagram (Figure 8.8). The cusps on the lines are caused by the interpolation technique used. To get a more detailed and smooth image, one must run the simulation for more temperatures.

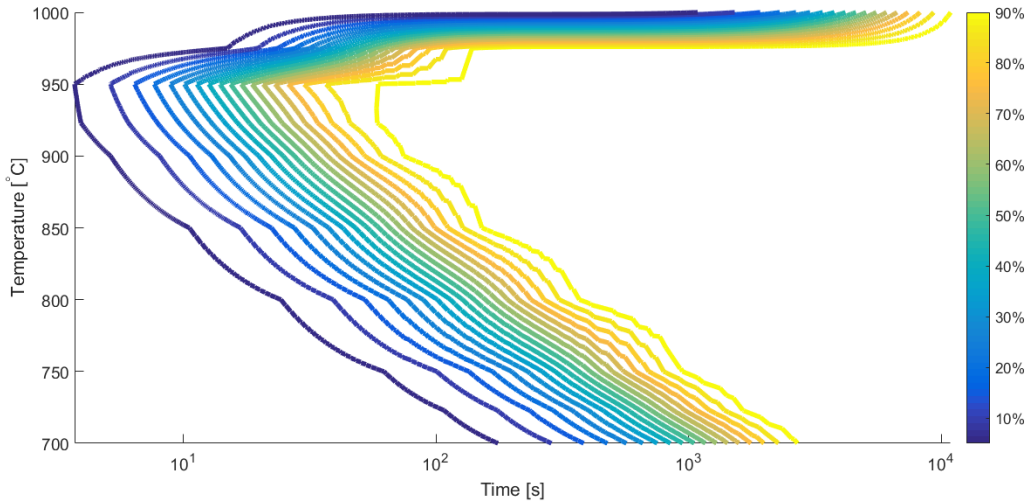

Figure 10.5: PTT diagrams for multiple percentages of the equilibrium volume fraction for nucleation on dislocations. The colours in the legend correspond to different percentages of the equilibrium volume fraction.

In Figure 10.6 the volume fractions for different temperatures for homogeneous nucleation are given. We do not find the plateaus in the volume fraction, as we did find for nucleation on dislocations and on grain boundaries. The resulting PTT diagram in Figure 10.7, shows this gives a more symmetrical shape. When plotting other PTT diagrams for homogeneous nucleation with different reference percentages, we find Figure 10.8. For all percentages we find the more or less symmetrical shape in the PTT diagram. Again, we find the cusps in the PTT diagram caused by the interpolation technique.

In general, it seems as if for non-homogeneous nucleation we find a non-symmetrical PTT diagram and for homogeneous nucleation we find a symmetrical PTT diagram. However, this should be further investigated.

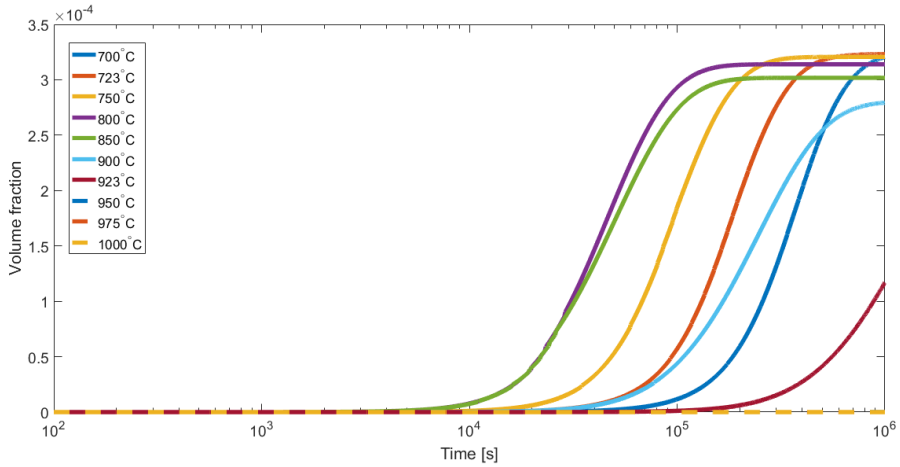

Figure 10.6: Volume fraction in time for different temperatures using the distribution approach for homogeneous nucleation.

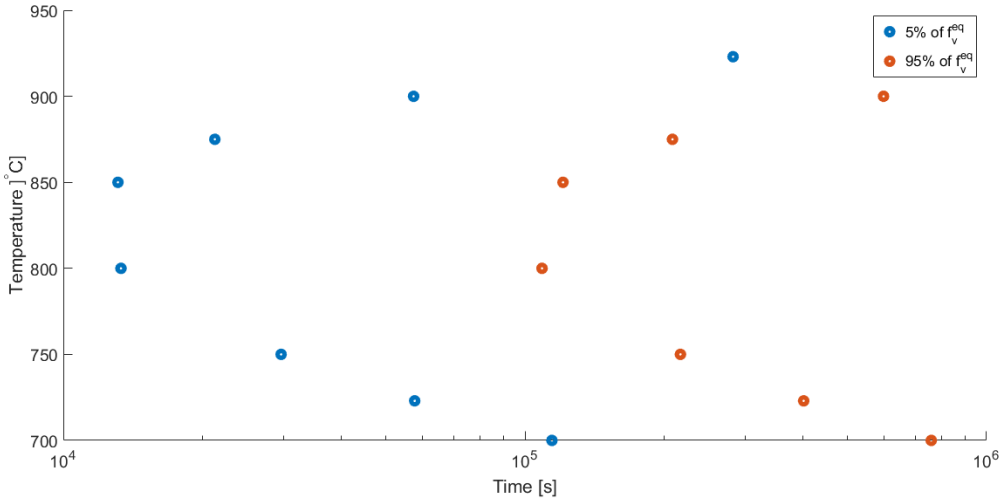

Figure 10.7: The precipitate-time-temperature curve using the distribution approach for homogeneous nucleation.

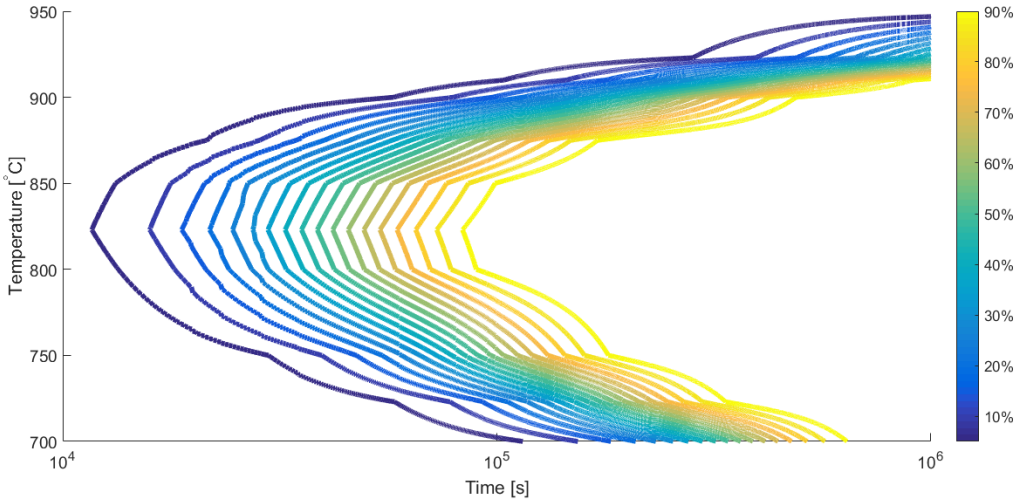

Figure 10.8: PTT diagrams for multiple percentages of the equilibrium volume fraction for homogeneous nucleation. The colours in the legend correspond to different percentages of the equilibrium volume fraction.

10.2. Various precipitate compositions

As described in the introduction of this section, different precipitate compositions[1] can occur simultaneously. We will illustrate the interaction between the different precipitate compositions, by first simulating the three precipitates (AlN, MnS, $NbCN$) separately at one nucleation site, namely on dislocations, and thereafter the three precipitates simultaneously at this site. We choose only one nucleation site, since it is just to illustrate the influence of multiple precipitate compositions and the capabilities of the model. Other combinations of precipitate compositions and nucleation site can also be used.

10.2.1. Simulation

The implementation used for nucleation of one precipitate originates from Chapter 4 (including the multi-component version of $Z\beta^*$), and the implementation used for the nucleation of the three precipitates simultaneously originates from Section 5.1. For the simulation we use a dislocation density (ρ) of 3.27×10^{14} $1/m^2$ and a temperature of 850 °C. Futhermore, we use the initial and numerical values from Chapter 8. The results of the simulation are found in Figures 10.9 to 10.16.

AlN

In Figure 10.13 the results for nucleation of the AlN precipitates are presented. In each plot, both the simulation with only nucleation of the AlN precipitates, as well as the simulation with nucleation of the three precipitates are presented. Looking at the number density, it seems as if nucleation of the AlN starts much earlier when competition is taken into account. However, this is mainly caused by the large difference in order of magnitude of the vertical scales. The number density of the simulation with competition is an order of magnitude 4 times smaller than the number density of the simulation without competition, which is a direct effect of the nucleation $NbCN$ that apparently has the preference of nucleating. When using the same y-axes for both results, we find Figure 10.9 and see that the real difference in the starting time of nucleation is a lot smaller. The competition still causes an advanced nucleation, which is probably caused by the indirect competition with the other precipitate compositions via the multi-component mechanism.

A clear cause of the advanced nucleation is hard to find, because of the complexities and cross dependencies of the model. A possible cause could be that the interaction of the different precipitates. The MnS precipitates nucleate earlier than the other precipitate compositions in the individual simulations. This also happens when simulation the three precipitate compositions at the same time. Earlier nucleation of MnS (compared to the other two) causes the concentrations of the other elements in the matrix to be relatively higher in this simulation than for the individual simulations of AlN and $NbCN$ precipitates. This results in a slightly less negative growth rate for precipitates with a radius smaller than the critical radius (as shown in Figure 10.10). Due to a less negative growth rate for small precipitates, the small precipitates dissolve slower, leading to a higher number density and larger mean radius. On the other hand, since the other elements in the matrix (not Mn ans S) form more stable precipitates, the concentration of Mn and S becomes relatively higher in the simulation than for the simulation without competition, also leading to more MnS precipitates. This leads to a reinforcing effect for all precipitates and an earlier increase in the precipitate number density. Later on in the simulation, the decrease in the nucleation rate damps this interaction effect, the growth rates becomes equal, and the precipitate number density reaches its maximum. This same effect is seen in both the precipitate number density of $NbCN$, as well as for MnS. The strength of the effect depends on the precipitate.

The volume fraction of the AlN precipitates is again orders of magnitude smaller when taking competition into account. From the saturation and the volume fraction, we see that the plateau in the number density is not caused by the kinetics of the AlN, but by the competition, since both the saturation and the volume fraction did not reached an equilibrium level yet.

The size of the AlN precipitates (Figure 10.13b) is larger than expected from experimental data and literature. This is caused by a high diffusion coefficient, leading to a higher growth rate for longer times. Comparing the growth rate of the AlN precipitates with and without competition of other precipitate compositions, for a precipitate with a radius of 1×10^{-8} m, we find Figure 10.11. In the beginning of the simulation, the competition causes the growth rate to decrease earlier, but due to the high diffusion coefficient and the influence

[1] In this thesis a precipitate compositions mean different kinds of precipitates, and not one kind precipitate like NbC_xN_{1-x} with varying x and y.

of the other elements in the system, the growth rate is larger for longer times for the simulation with competition, than for the simulation without competition of other precipitate compositions. This causes the AlN precipitates to keep growing at a higher rate, leading to larger precipitates.

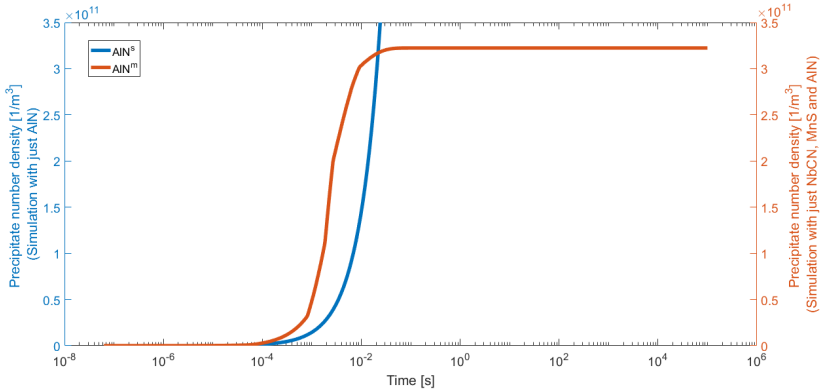

Figure 10.9: The results of the simulation for AlN precipitation with (red line) and without (blue line) competition of other precipitate compositions, using the same y-axis for both results.

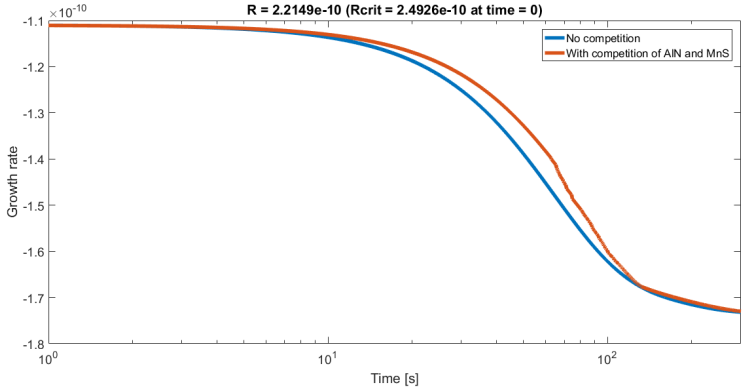

Figure 10.10: The growth rate of AlN precipitates with radius 2.2149×10^{-10} m, which is smaller than the critical radius at the starting time. The simulation with (red line) and without (blue line) competition of other precipitate compositions on dislocations are compared.

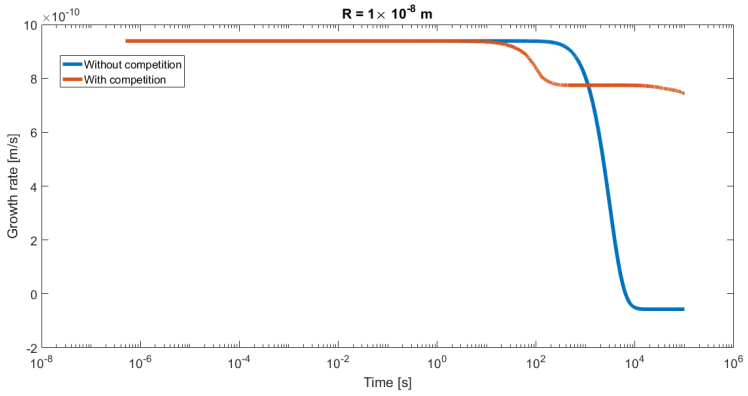

Figure 11: The growth rate of AlN precipitates for a precipitate with radius 1×10^{-8} m, which is larger than the critical radius at the starting time. The simulation with (red line) and without (blue line) competition of other precipitate compositions on dislocations are compared.

MnS

In Figure 10.14 the results for nucleation of the *MnS* precipitates are presented. In each plot, both the simulation with only nucleation of the *MnS* precipitates, as well as the simulation with nucleation of the three precipitates are presented. If we compare the simulation with and without the interaction with other precipitates, we note that when the *MnS* is influenced by the other two precipitates, the plateau in the precipitate number density decreases. This is caused by competition over nucleation positions, since the other precipitates (*AlN* and *NbCN*) nucleate on the same nucleation sites, namely on dislocations. Furthermore we find that nucleation starts earlier when competition is taken into account as we also saw for *AlN* precipitates. Again this is caused by slower dissolving precipitates due to a less negative growth rate for precipitates with a radius smaller than the critical radius (Figure 10.12). Both the equilibrium level of the saturation and the volume fraction are reached at roughly the same time, since the *MnS* experiences no competition for elements from *NbCN* and *AlN*.

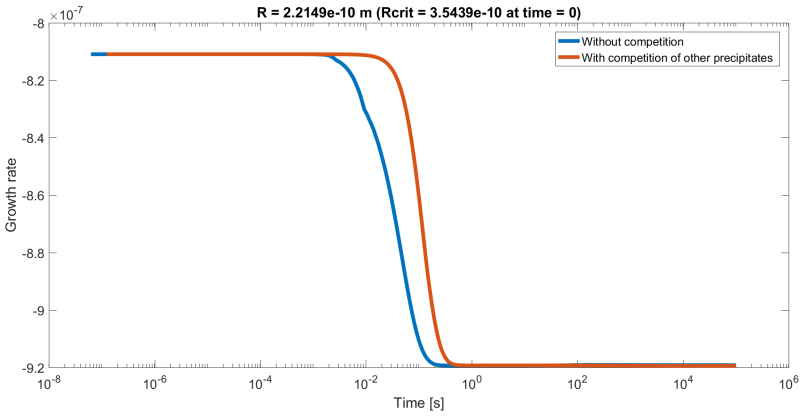

Figure 10.12: The growth rate of *MnS* precipitates with radius 2.2149×10^{-10} m, which is smaller than the critical radius at the starting time. The simulation with (red line) and without (blue line) competition of other precipitate compositions on dislocations are compared.

NbCN

In Figure 10.15 the results for nucleation of the *NbCN* precipitates are presented. In each plot, both the simulation with just nucleation of the *NbCN* precipitates, as well as the simulation of the *NbCN* precipitates in combination with the nucleation of the *AlN* and *MnS* precipitates are presented. We note that when the *NbCN* is influenced by the other two precipitates, the plateau in the precipitate number density decreases, mainly caused by competition for the *N* atoms. The order of magnitude, however, is comparable. Next to the direct competition between the *NbCN* and the *AlN* precipitates for the *N* atoms, also competition over the available nucleation positions exists, as the other precipitates (*AlN* and *MnS*) nucleate at the same nucleation site. The precipitates that do exist are slightly larger, than those that exist for the simulation without influence of the other two precipitate compositions. Less precipitates, but larger in size, leads to a similar volume fraction as confirmed by the figure. Also the saturation plots are similar for both with and without competition of the other precipitate compositions.

Combination of precipitate compositions

To be able to compare the nucleation of the three precipitates at one nucleation site, we plot the properties of each precipitate in one figure. This results in Figure 10.16. The precipitate number density of the three precipitate compositions shows that the three precipitates start to nucleated around the same time (10^{-4} s). Furthermore we see that the *NbCN* precipitate is more stable than the *AlN* precipitate. This effect is seen in the number density, but even more in the volume fraction. Also, when the *MnS* precipitates start to coarsen (number density decreases, and mean diameter increases), the newly available sites are than occupied by the *NbCN* precipitates, leading to a temporarily increase in the number density of *NbCN*. The increase is only temporarily, since the volume fraction of *NbCN* had already reached an equilibrium and the *AlN* precipitates start to grow. The number density of the *AlN* precipitates is the lowest of the three precipitate compositions taken into account, but the precipitates that do exist are of a greater size than those of the other two precipitate compositions, which is mainly caused by the high effective diffusion coefficient of *Al* for nucleation on dislocations.

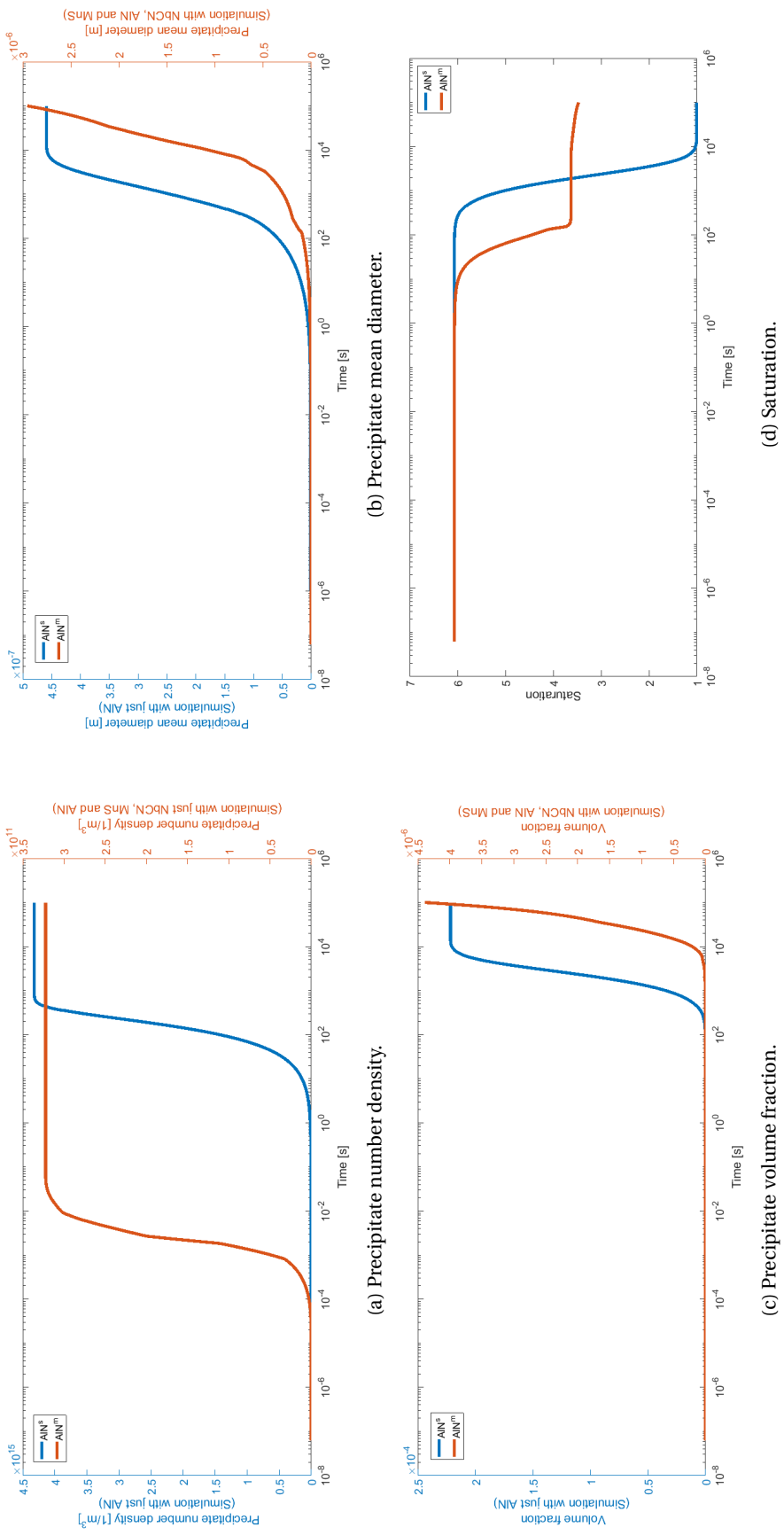

(a) Precipitate number density.

(b) Precipitate mean diameter.

(c) Precipitate volume fraction.

(d) Saturation.

Figure 10.13: The results of the simulation for *AlN* precipitation with only nucleation of the *AlN* precipitate, indicated with a *s* (single-precipitate, blue line) and the simulation for the *AlN* precipitates influenced by the nucleation of the *NbCN* and *MnS* precipitates, indicated with a *m* (multi-precipitate, red line). Note the different order of magnitude, when two y-axes are used.

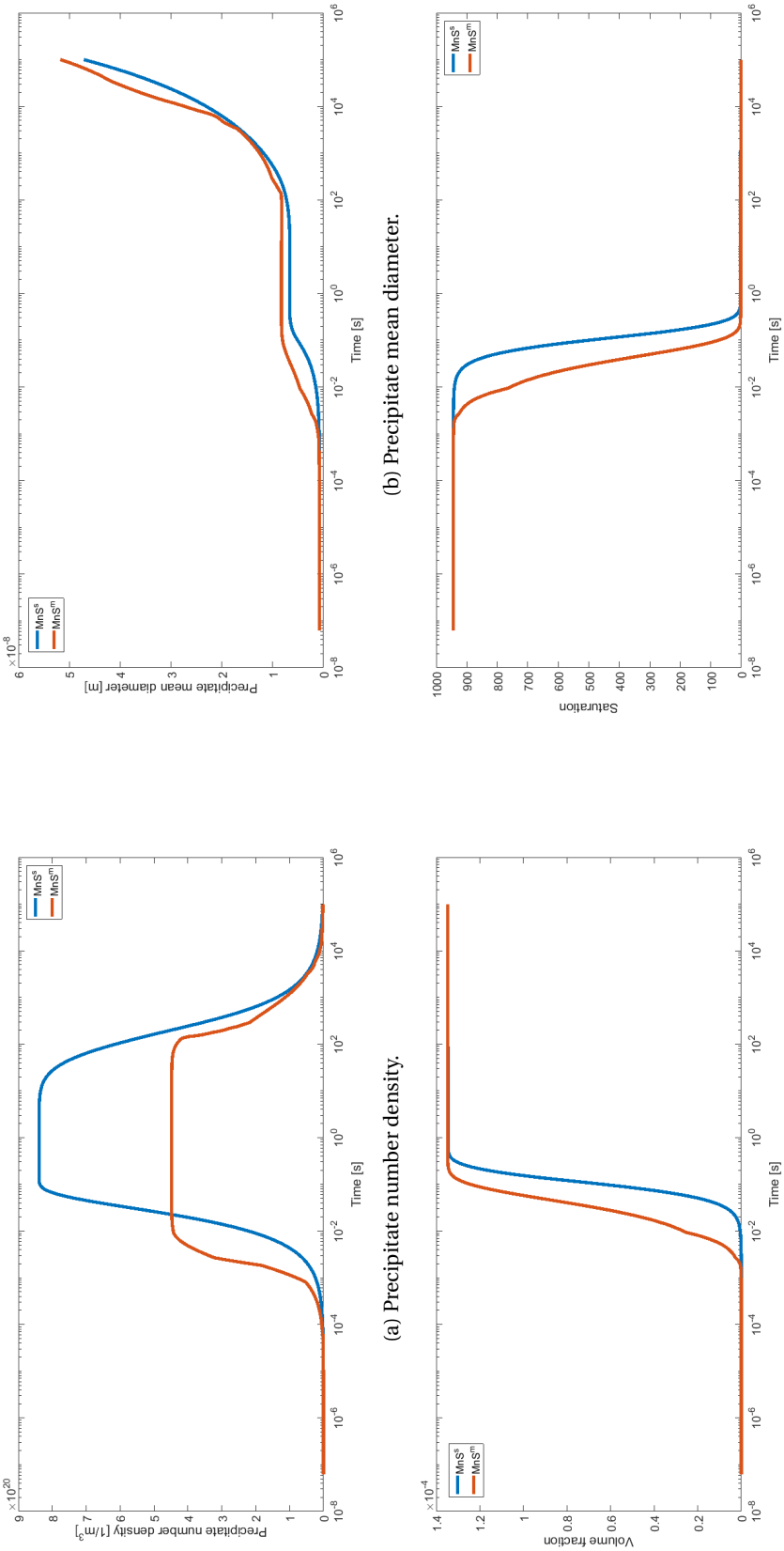

(a) Precipitate number density.

(b) Precipitate mean diameter.

(c) Precipitate volume fraction.

(d) Saturation.

Figure 10.14: The results of the simulation for MnS precipitation with only nucleation of the MnS precipitate, indicated with a s (single-precipitate, blue line) and the simulation for the MnS precipitates influenced by the nucleation of the $NbCN$ and AlN precipitates, indicated with a m (multi-precipitate, red line).

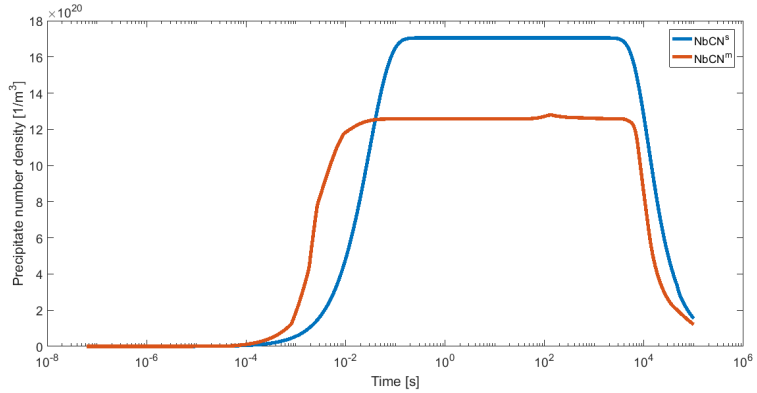

(a) Precipitate number density.

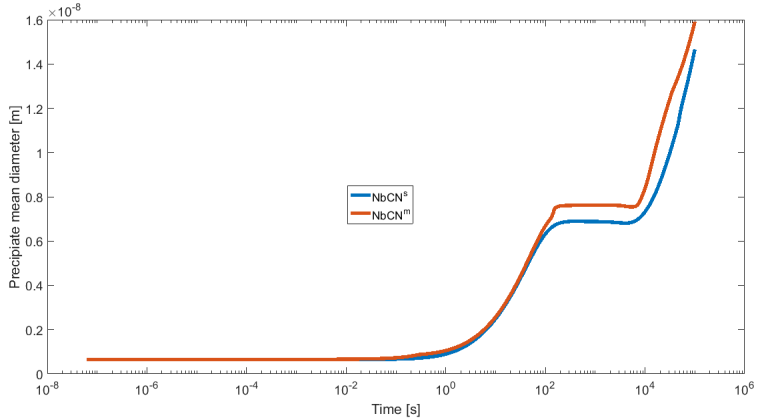

(b) Precipitate mean diameter.

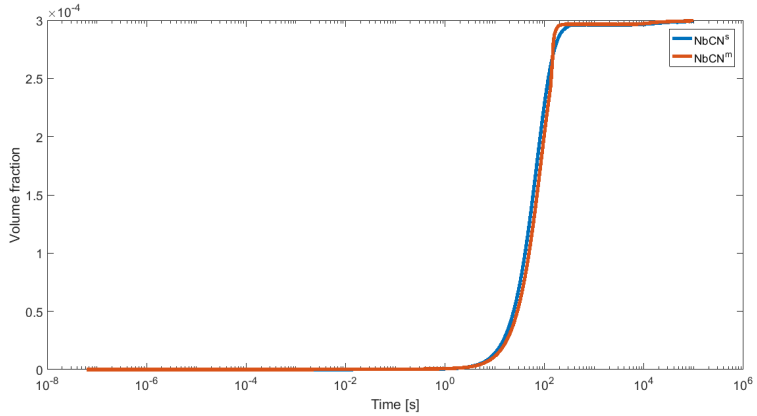

(c) Precipitate volume fraction.

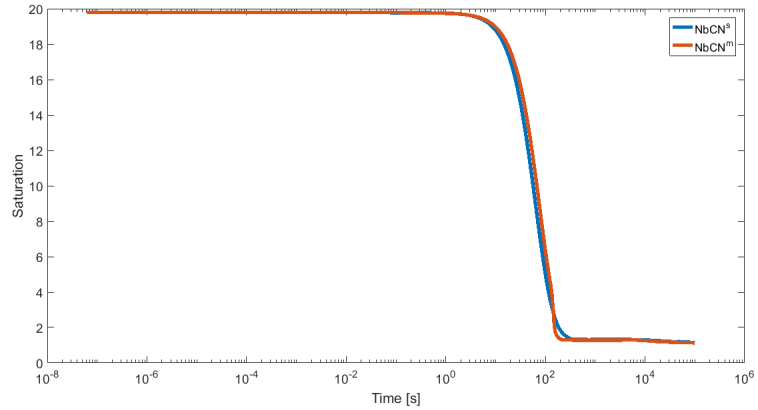

(d) Saturation.

Figure 10.15: The results of the simulation for $NbCN$ precipitation with only nucleation of the $NbCN$ precipitate, indicated with a s (single-precipitate, blue line) and the simulation for the $NbCN$ precipitates influenced by the nucleation of the AlN and MnS precipitates, indicated with a m (multi-precipitate, red line).

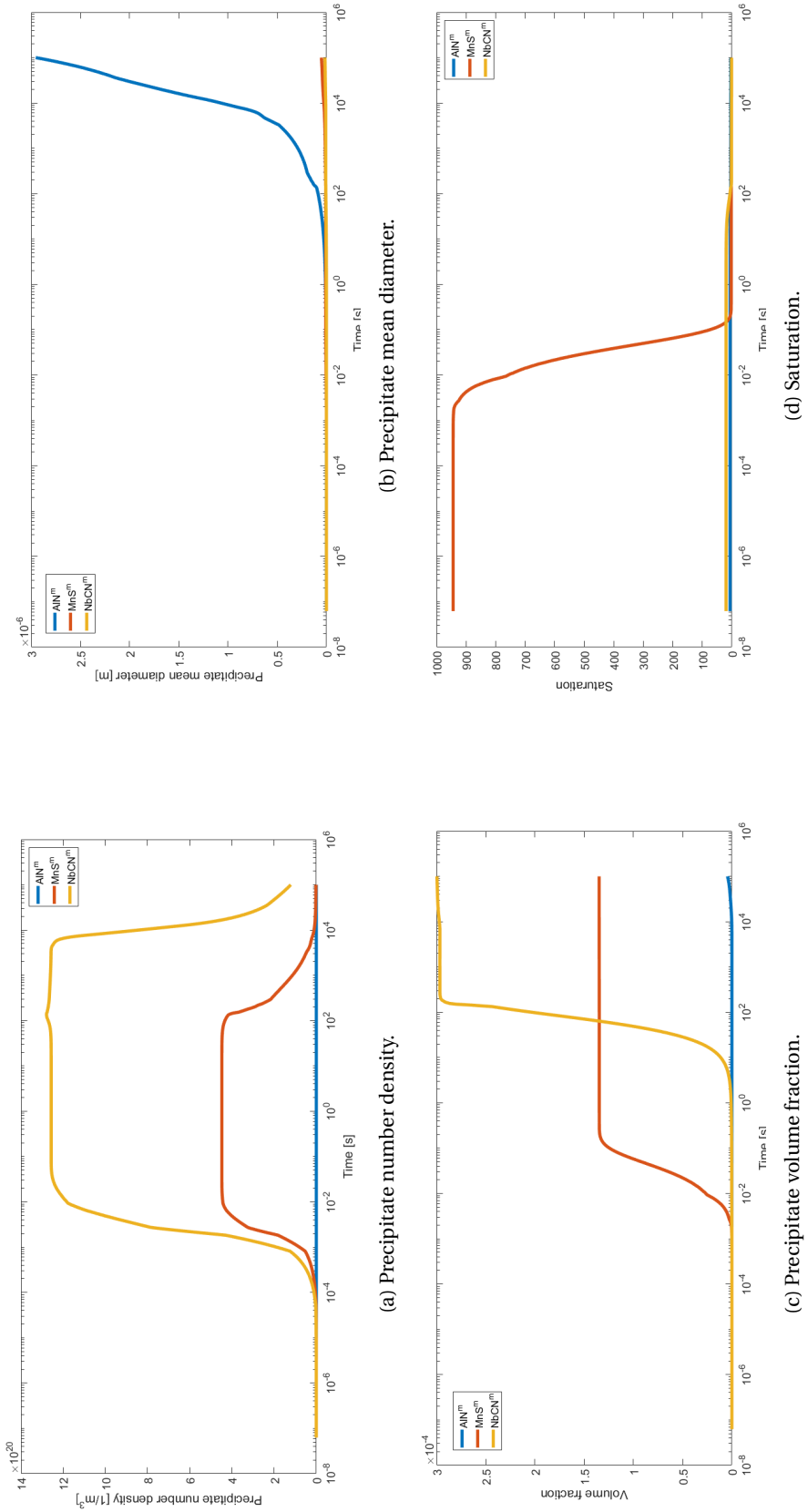

(a) Precipitate number density.

(b) Precipitate mean diameter.

(c) Precipitate volume fraction.

(d) Saturation.

Figure 10.16: The results of the simulation of the *AlN* (blue line), *MnS* (red line) and *NbCN* (yellow line) precipitates with interaction between the precipitates, indicated with a m (multi-precipitate), at one nucleation site, namely dislocations.

10.3. Various nucleation sites

Besides the interaction between various precipitate compositions, also the nucleation on one nucleation site influences the nucleation on other nucleation sites. We will illustrate the interaction between different nucleation sites, by first simulating one of the precipitates, $NbCN$, at each site separately, and thereafter at the three nucleation sites, on dislocations, on grain boundaries and in the matrix, simultaneously. We choose only one precipitate, since it is just to illustrate the influence of multiple nucleation sites and the capabilities of the model. Other combinations of nucleation site and precipitate composition can also be used. We use the initial and numerical values from Chapter 8 for the simulations.

10.3.1. Simulation

For the simulation we use a temperature of 850 °C, a dislocation density (ρ) of 3.27×10^{14} $1/\text{m}^2$, the radius of a grain (R_{grain}) of 10^{-6} m and a grain thickness (δ_{gb})of $3a$, where a is the lattice constant of austenite. The results of the simulation are found in Figures 10.17b to 10.21. Since the saturation is a property of the matrix, as it describes the ratio of the matrix and the equilibrium concentrations, it is equal for all nucleation sites.

Machine precision

In the first simulations which included the interaction with other nucleation sites, we found a strange behavior in for example the mean diameter of the precipitates at dislocations (Figure 10.17a). However, when we look at the volume fraction of the precipitates at dislocations on a double-logarithmic scale (both the x- and y-axes), we find that the volume fraction becomes so small (below the machine precision, see Figure 10.17b) that the mean radius does not matter anymore. For this reason we omit the results in the plots, where the volume fraction is below the machine precision. This also holds for other nucleation sites.

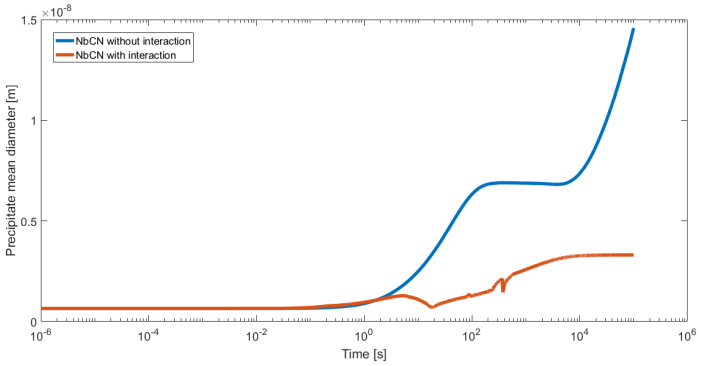

(a) Mean diameter of $NbCN$ precipitates at dislocations.

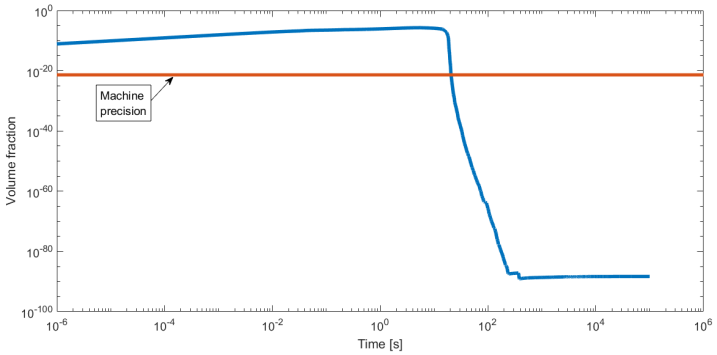

(b) Volume fraction of $NbCN$ precipitates at dislocations on a double-logarithmic scale, together with the machine precision.

Figure 10.17: Simulations of the $NbCN$ precipitates at dislocations.

Dislocations

In Figure 10.18 the results for nucleation on dislocations are presented. In each plot, both the simulation with only nucleation on dislocations, as well as the simulation with nucleation on the three nucleation sites are presented. The implementation used for only nucleation on dislocation originates from Chapter 4, and the implementation used for nucleation at the other two sites is given in Section 5.2.
The number density of the $NbCN$ precipitates on dislocations reaches the same maximum plateau for both simulations, with and without competition of other sites. However, when competition of other sites is taken into account, we find a steep decrease in the number density a lot earlier than for the simulation without competition. A first thought could be that coarsening is taking place a lot earlier, but the mean diameter speaks against this. Also the volume fraction shows that it is not coarsening, but the precipitates actually start to dissolve. From the volume fraction we furthermore see that the precipitation starts earlier when competition is taken into account. This is the same effect as we saw for the competition between precipitate compositions in Section 10.2.

Grain boundaries

In Figure 10.19 the results for nucleation on grain boundaries are presented. In each plot, both the simulation with only nucleation on grain boundaries, as well as the simulation with nucleation on the three nucleation sites are presented. The implementation used for just nucleation on grain boundaries and nucleation at the three sites originates from Section 5.2.
The number density of the $NbCN$ on grain boundaries reaches the same maximum plateau for both simulations, with and without competition of other sites. However, when competition of other sites is taken into account, we find a steep decrease in the number density takes place at much earlier times than for the simulation without competition. For nucleation on dislocations we saw a comparable result (Figure 10.18a), which was caused by the dissolving of precipitates. For nucleation on grain boundaries we find that it is actually early coarsening, since the mean diameter increases. Also the volume fraction reaches the equilibrium level earlier, meaning that the nucleation on grain boundaries is accelerated when competition of other nucleation sites is added to the system.

Homogeneous nucleation

In Figure 10.20 the results for homogeneous nucleation are presented. In each plot, both the simulation with just nucleation on dislocations, as well as the simulation with nucleation on the three nucleation sites are presented. The implementation used for homogeneous nucleation and nucleation at the three sites originates from Section 5.2.
The number density of the $NbCN$ for homogeneous nucleation shows a strange behavior. It seems as if the values for precipitate number density and volume fraction at early times for the simulation with competition is much higher than the value at early times for the simulation without competition. However, the order of magnitude shown on the axes, says the opposite. This same effect was seen in the results of the AlN precipitation (Figure 10.13). The number density of the precipitates is of such a small order of magnitude, that we can state that homogeneous nucleation is negligible, when precipitates can also nucleate at other sites. The volume fraction stresses this even more, since it is of an even smaller order of magnitude ($\sim 10^{-14}$).

Combination of nucleation sites

To be able to compare the nucleation of the $NbCN$ precipitate at the various nucleation sites, we plot the properties of the precipitation evolution at each site in one figure. This results in Figure 10.21. We find that nucleation on dislocations and nucleation on grain boundaries both reach their maximum plateau, and the precipitate number density of homogeneous nucleation is a lot smaller. However, when we look at the mean diameter of all three nucleation sites, we find that the precipitates on grain boundaries grow a lot further than those at the other two nucleation sites. For longer time, nucleation on grain boundaries is clearly favoured over the other two nucleation sites. When we look at the individual volume fractions, we find that for both homogeneous nucleation and nucleation on dislocations, the volume fraction is lowered by competition. The precipitate number density and volume fraction, for nucleation on dislocations, are mostly hindered by the competition at longer times. The determining factor for this is the activation energy, which is lower for grain boundaries than for dislocations and homogeneous nucleation for longer times. One can conclude that for longer times, precipitation on grain boundaries wins over the other two nucleation sites. As explained before, the saturation is a property of the matrix and is therefore equal for all nucleation sites when simulated together (Figure 10.21).

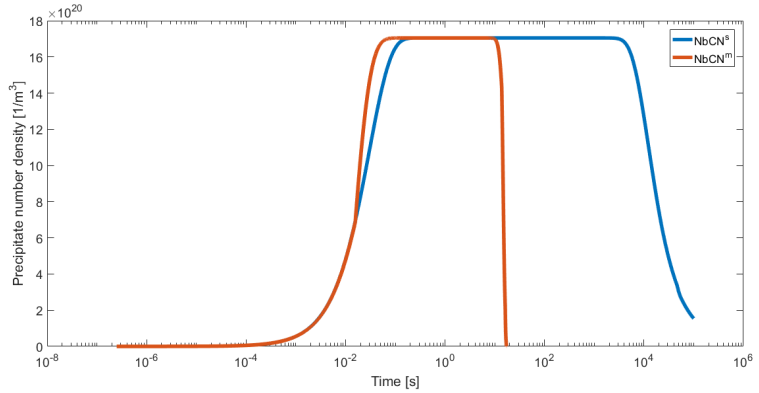

(a) Precipitate number density.

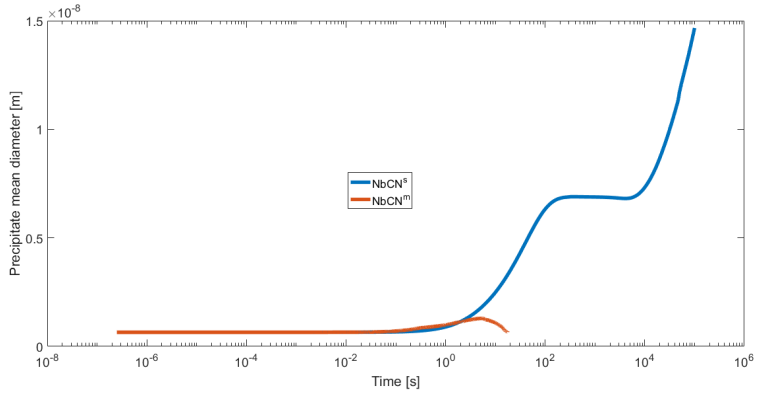

(b) Precipitate mean diameter.

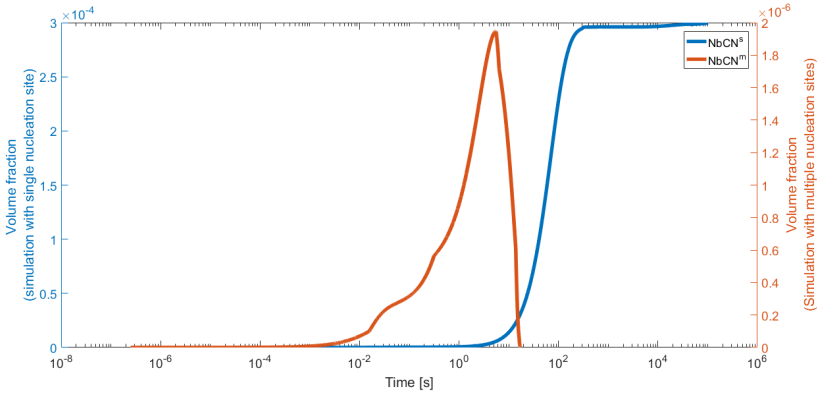

(c) Precipitate volume fraction.

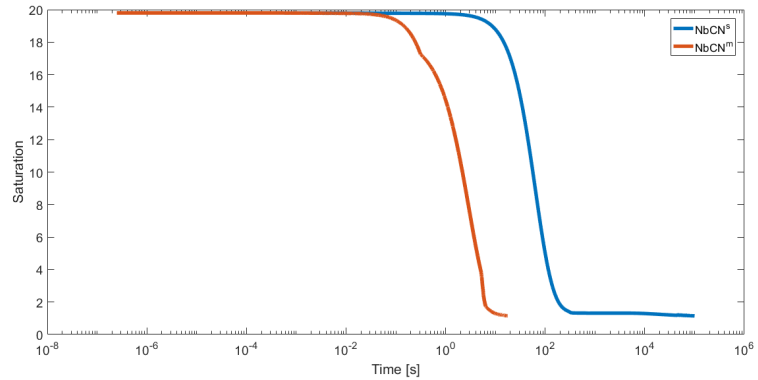

(d) Saturation.

Figure 10.18: The results of the simulation for the $NbCN$ precipitates with only nucleation on dislocations, indicated with a s (single-precipitate, blue line) and the simulation for the $NbCN$ precipitates on all three sites (on dislocations, on grain boundaries and homogeneous nucleation), indicated with a m (multi-precipitate, red line). Note the different order of magnitude, when two y-axes are used.

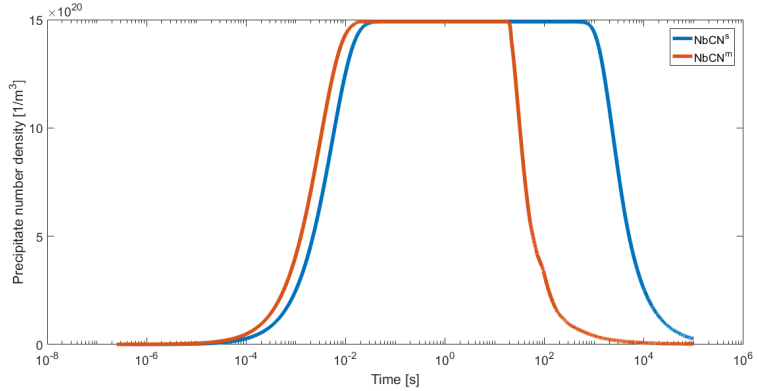

(a) Precipitate number density.

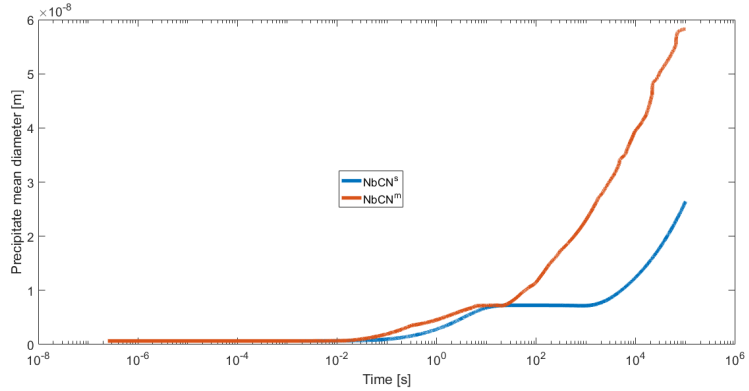

(b) Precipitate mean diameter.

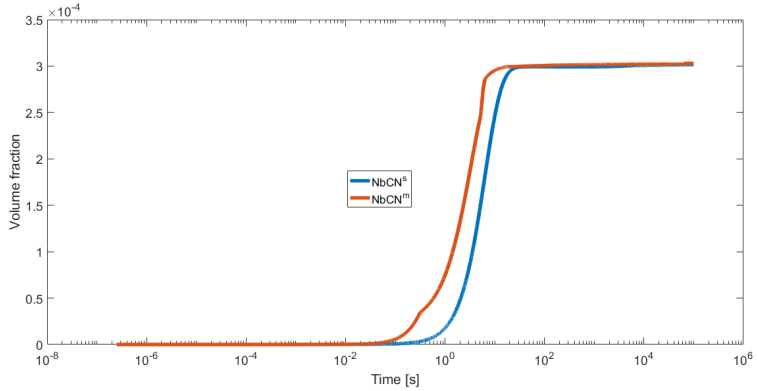

(c) Precipitate volume fraction.

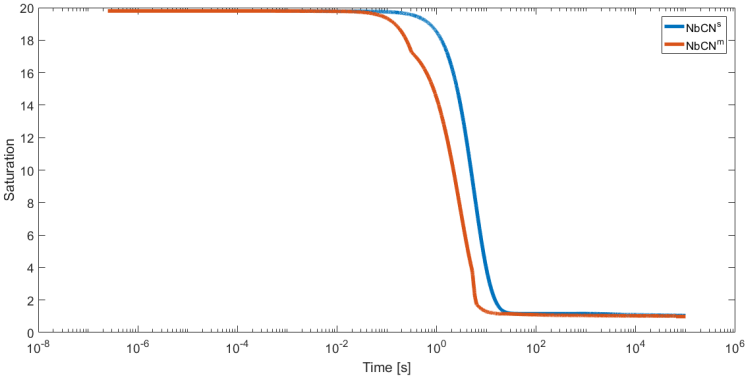

(d) Saturation.

Figure 10.19: The results of the simulation for the $NbCN$ precipitates with only nucleation on grain boundaries, indicated with a s (single-precipitate, blue line) and the simulation for the $NbCN$ precipitates on all three sites (on dislocations, on grain boundaries and homogeneous nucleation), indicated with a m (multi-precipitate, red line).

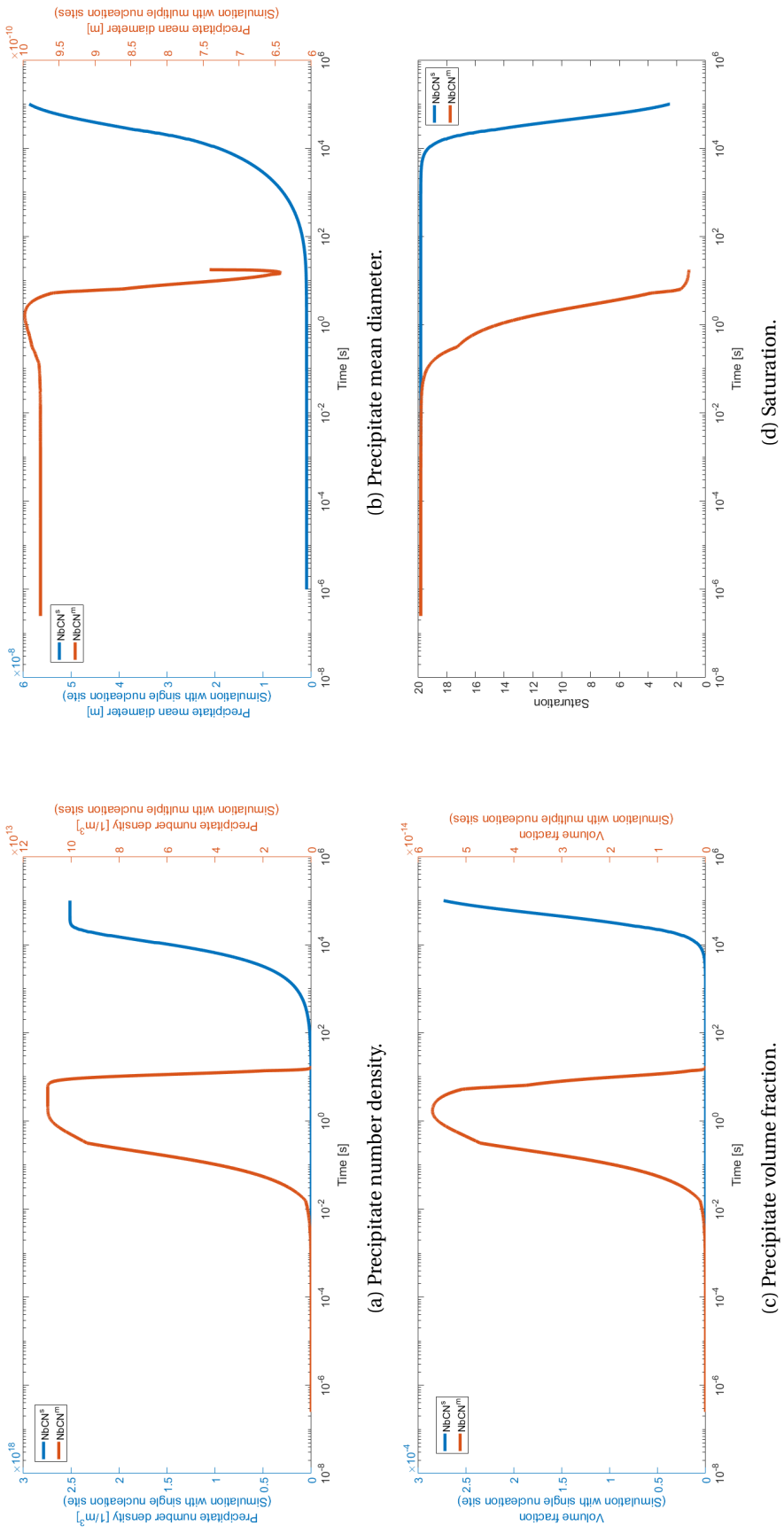

(a) Precipitate number density.

(b) Precipitate mean diameter.

(c) Precipitate volume fraction.

(d) Saturation.

Figure 10.20: The results of the simulation for the *NbCN* precipitates with just homogeneous nucleation, indicated with a *s* (single-precipitate, blue line) and the simulation for the *NbCN* precipitates on all three sites (on dislocations, on grain boundaries and homogeneous nucleation), indicated with a *m* (multi-precipitate, red line). Note the different order of magnitude, when two y-axes are used.

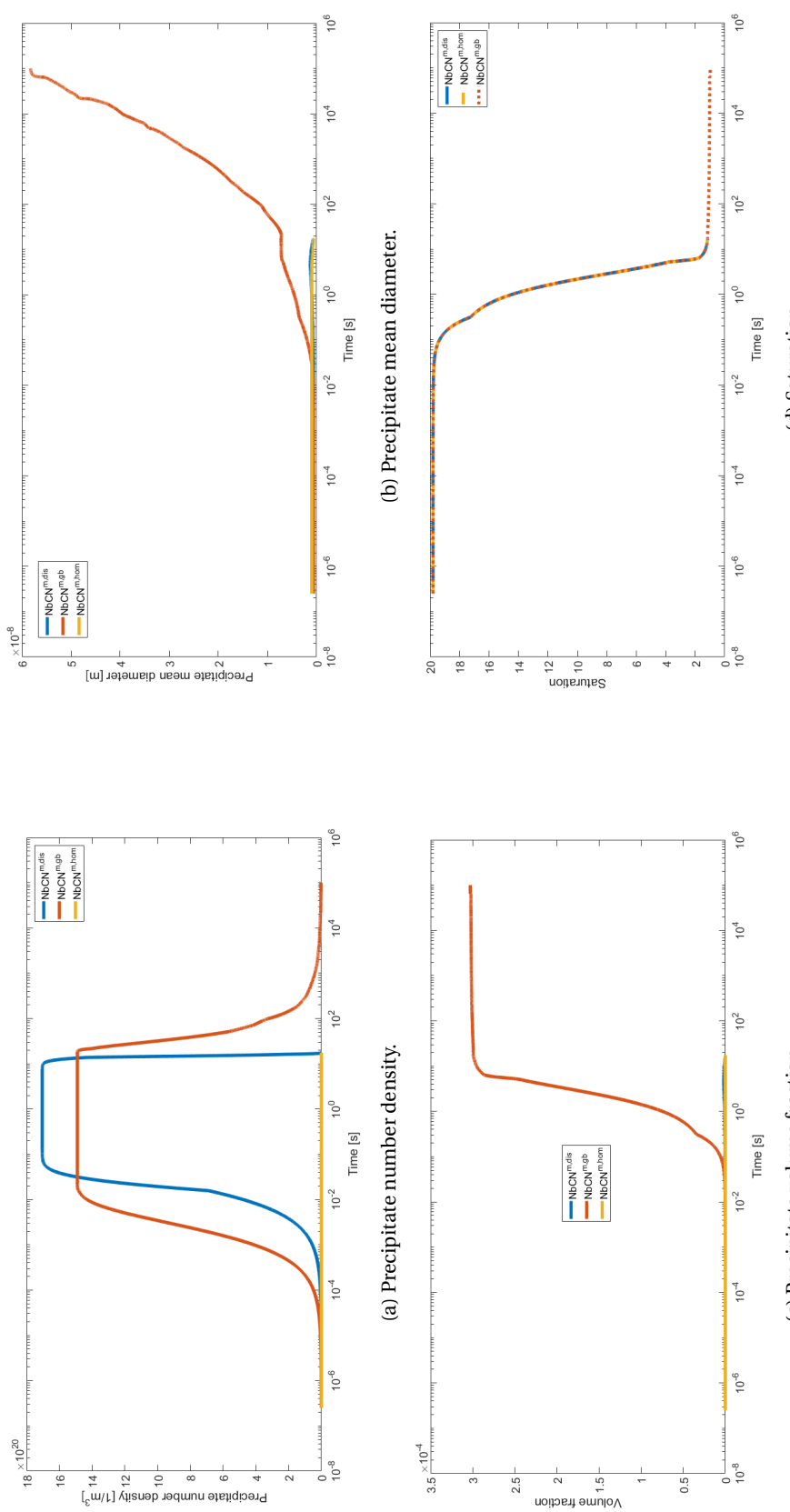

(a) Precipitate number density.

(b) Precipitate mean diameter.

(c) Precipitate volume fraction.

(d) Saturation.

Figure 10.21: The results of the simulation for the *NbCN* precipitates with nucleation on all three sites (on dislocations (blue line), on grain boundaries (red line) and homogeneous nucleation (yellow line)), indicated with a m (multi-precipitate) and the site.

10.4. Various precipitate compositions and various nucleation sites

Now that we have illustrated the interaction of different precipitates and the interaction of different nucleation sites, we would like to combine both implementations. However, when simulating the three precipitates, $NbCN$, AlN and MnS at the three nucleation sites, the computation time is drastically increased to such a level that it would take more than two weeks of computation time. The MnS precipitate is causing most of the time increase, since the calculation of the growth rate for this precipitate is more time consuming than that of the other two precipitates. The difference is caused by the molar volume of MnS, which is twice the molar volume of $NbCN$ or AlN. This causes the model to demand a higher accuracy, leading to a higher computation time. Also the ratio of the diffusion coefficients of Mn and S is much lower than for Nb and C and N, which also influences the growth rate. When we compare the growth rates at time is zero, for each precipitate without competition between precipitates with nucleation only on dislocations, we find Figure 10.22. The growth rate of MnS is three orders of magnitude larger than that of AlN, and even six orders of magnitude larger than that of $NbCN$. Also the bend in the growth rate is more strict for MnS, leading to a harder division between the (slowly) growing precipitates and (fast) dissolving precipitates, which requires the higher accuracy.

Since the simulation has a more illustrative character, we choose to only simulate the two precipitates, $NbCN$ and AlN, using Section 5.1 but at all three nucleation sites (dislocations, grain boundaries, homogeneous nucleation) using Section 5.2. For future work it would be recommended to do further research on the computation time increase caused by MnS and potential solutions, since latest research shows that MnS may play a role in grain refinement and precipitation hardening (Rodionova et al. (2016)), potentially leading to lower costs in steel production.

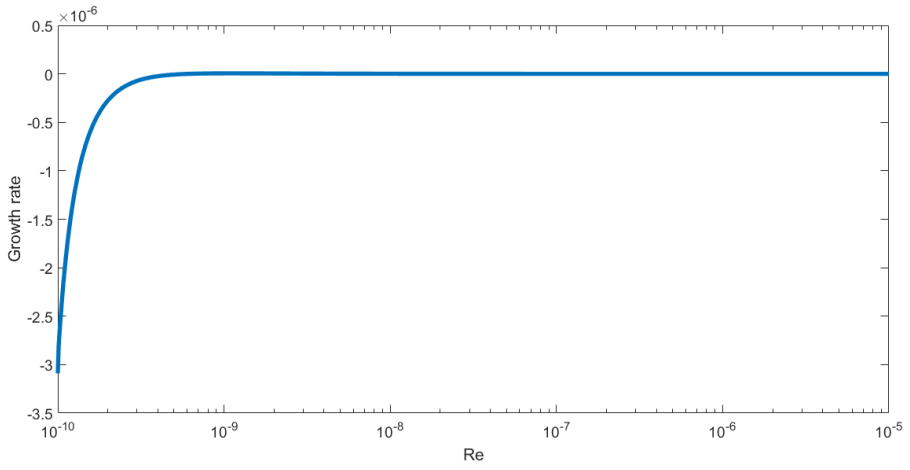

(a) AlN

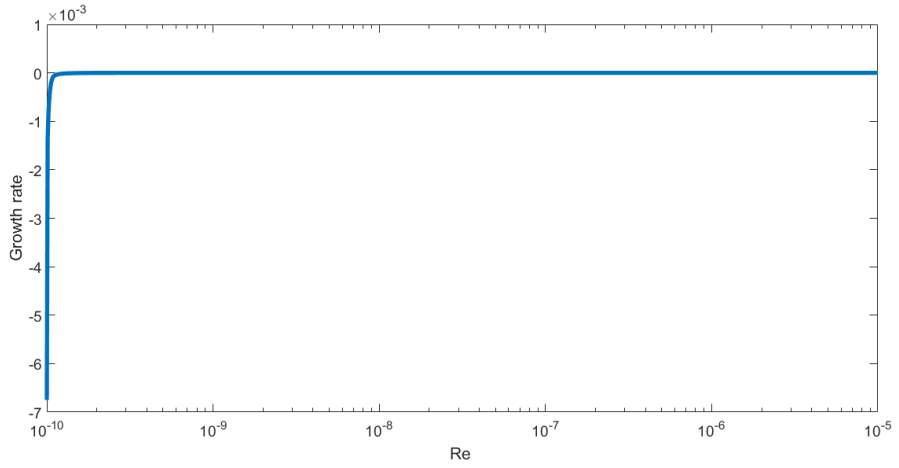

(b) MnS

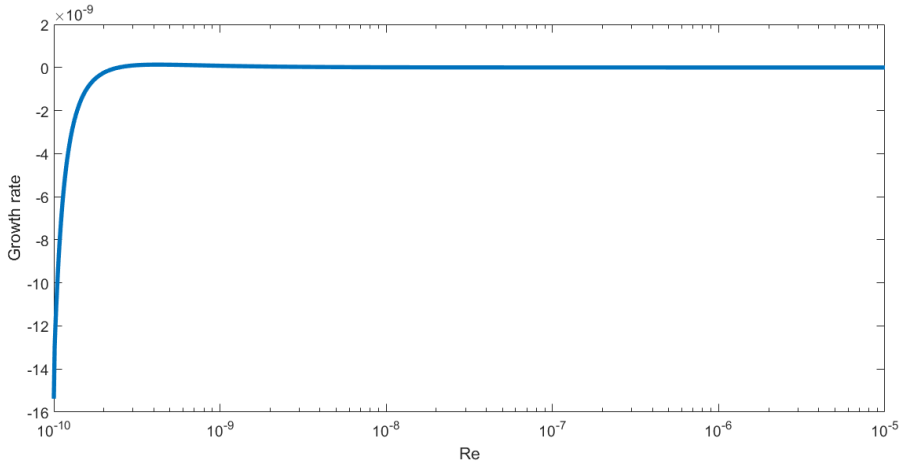

(c) $NbCN$

Figure 10.22: Growth rates of individual precipitates at dislocations at time is zero, plotted at the cell edges.

10.4.1. Simulation

For the simulation we use a temperature of 850 °C, a dislocation density (ρ) of 3.27×10^{14} 1/m^2, the radius of a grain (R_{grain}) of 10^{-6} m and a grain thickness (δ_{gb})of $3a$, where a is the lattice constant of austenite. We use the initial and numerical values given in Chapter 8. Furthermore, the implementation used for just nucleation on grain boundaries and nucleation at the three sites originates from Section 5.2 and for nucleation on dislocations from Chapter 4. The results of the simulations at the three nucleation sites are given in Figures 10.23 and 10.24 for AlN, in Figure 10.25 for $NbCN$, and in Figure 10.26 for both $NbCN$ and AlN. The simulation had a computation time of around 21 hours[1] for 1×10^5 simulation seconds.

AlN

In Figure 10.23 the results for AlN precipitation at the three nucleation sites are presented. In each plot, both the simulation with only nucleation on one site, as well as the simulation with nucleation on the three nucleation sites are presented.
We find that the precipitate number density of AlN is reduced by the competition with $NbCN$ and other nucleation sites. The precipitate number density for the simulation with competition are not even visible. When plotting the densities separately for each site, we find Figure 10.24a. For the single simulation, with only AlN, we find that nucleation at grain boundaries results in the highest number density. When competition is added, the precipitate number density is largely decreased for all nucleation sites. Also the volume fraction is much lower when competition between sites and precipitate competition is added. In one figure the volume fraction of the simulations with competition are not even visible. As we did for the precipitate number density, we plot the results separately for each site in Figure 10.24b. Again, for each nucleation site the volume fraction is largely decreased when competition is added. The large decrease in number density and volume fraction is caused by the direct competition with $NbCN$ for the N atoms. This effect is larger than we saw in Section 10.2, since the $NbCN$ can now also grow on grain boundaries, leading to a higher competition for the available nucleation positions, and therefore taking up even more elements.

Looking at the size of the precipitates in Figure 10.23b, we find the precipitates grow faster when competition is added to the system, caused by the indirect competition from the multi-component property of the model. As we saw earlier, the growth rate stays at a higher level for longer times when competition is added. The precipitates at dislocations are the largest, for both the simulation with and without competition. This is caused by the high effective diffusion coefficient of Al for nucleation on dislocations. When comparing the diffusion coefficient for nucleation on dislocations in Figure 5.2, we find that the pipe diffusion coefficient of Al is orders of magnitude larger than grain boundary and bulk diffusion coefficients. Using an effective diffusion coefficient, as described in Section 5.2.2, should damp this effect, but comparing the effective diffusion coefficients in Table 10.3 shows this damping effect is not enough. As stated in Section 5.2.2 it is an

[1] For the simulation we use MATLAB 2016b on Windows®.

essential point for future research to find correct values for the diffusion coefficients. This simulation shows furthermore that the damping effect of the effective diffusion coefficient in this case is not enough and further investigation of the diffusion coefficients is necessary to see whether a different definition of the effective diffusion coefficient should be used.

Nucleation site	Effective diffusion coefficient in m^2/s
Dislocations	3.4718×10^{-14}
Grain boundaries	1.2153×10^{-15}
Bulk	4.1050×10^{-16}

Table 10.3: Effective diffusion coefficient of Al at 850 °C for various nucleation sites.

The saturation shows that when competition is added, the saturation drops earlier, but does not reach the equilibrium level of one within the chosen time range.

NbCN

In Figure 10.25 the results for $NbCN$ precipitation at the three nucleation sites are presented. In each plot, both the simulation with only nucleation on one site, as well as the simulation with nucleation on the three nucleation sites are presented.
We find that the precipitate number density of $NbCN$ is influenced in various ways (Figure 10.25a. The maximum level for nucleation on dislocations and grain boundaries is still reached, but homogeneous nucleation is almost zero. This agrees with the results we found when just observing competition due to various nucleation sites. The nucleation on dislocations and on grain boundaries is slightly delayed, when compared with the simulation without interaction between precipitates. This is actually in contrast to the results we found in Section 10.3. This is due to the competition with AlN, that was not present in that section. The mean diameter is also influenced by the competition. The precipitates that are formed are much smaller than without competition when compared at the same time. Only for nucleation on grain boundaries we clearly see a mean diameter above zero, around 0.5×10^{-8} m. The volume fraction gives similar results, and shows that the grain boundaries are favoured over the dislocations and over homogeneous nucleation when competition of other precipitate compositions is present.

AlN and *NbCN*

In Figure 10.26 the results for both AlN and $NbCN$ precipitation with competition between the precipitates and nucleation sites are presented.
When combining the plots for $NbCN$ and AlN with competition, we find that $NbCN$ precipitates on dislocations and on grain boundaries are favoured. AlN precipitates do start to nucleate later on in the simulation, but its volume of fraction is orders of magnitude smaller than that of $NbCN$. Furthermore we find that the $NbCN$ precipitates reach their equilibrium saturation within the used simulation time, while the AlN precipitates do not reach their equilibrium saturation within the used simulation time due to competition.

10.4.2. Result interpretation

The results in this section (Figure 10.23 - Figure 10.26) should be mainly interpreted qualitatively, since accurate quantitative results not only depend on the composition and temperature, but also on accurate values of the fitting parameters in Table 10.1 and the diffusion coefficients in Section 5.2.2. It is not expected that the fitting parameters found when fitting experimental data to the model will differ much in order of magnitude. However, the diffusion coefficients and effective diffusion coefficient can have large influences on the results, as already seen for AlN precipitates. From the results and literature, we find that homogeneous precipitation is dominated by precipitation on dislocations and on grain boundaries. Therefore, experimental data for validating and improving the models, should concentrate on these nucleation sites.

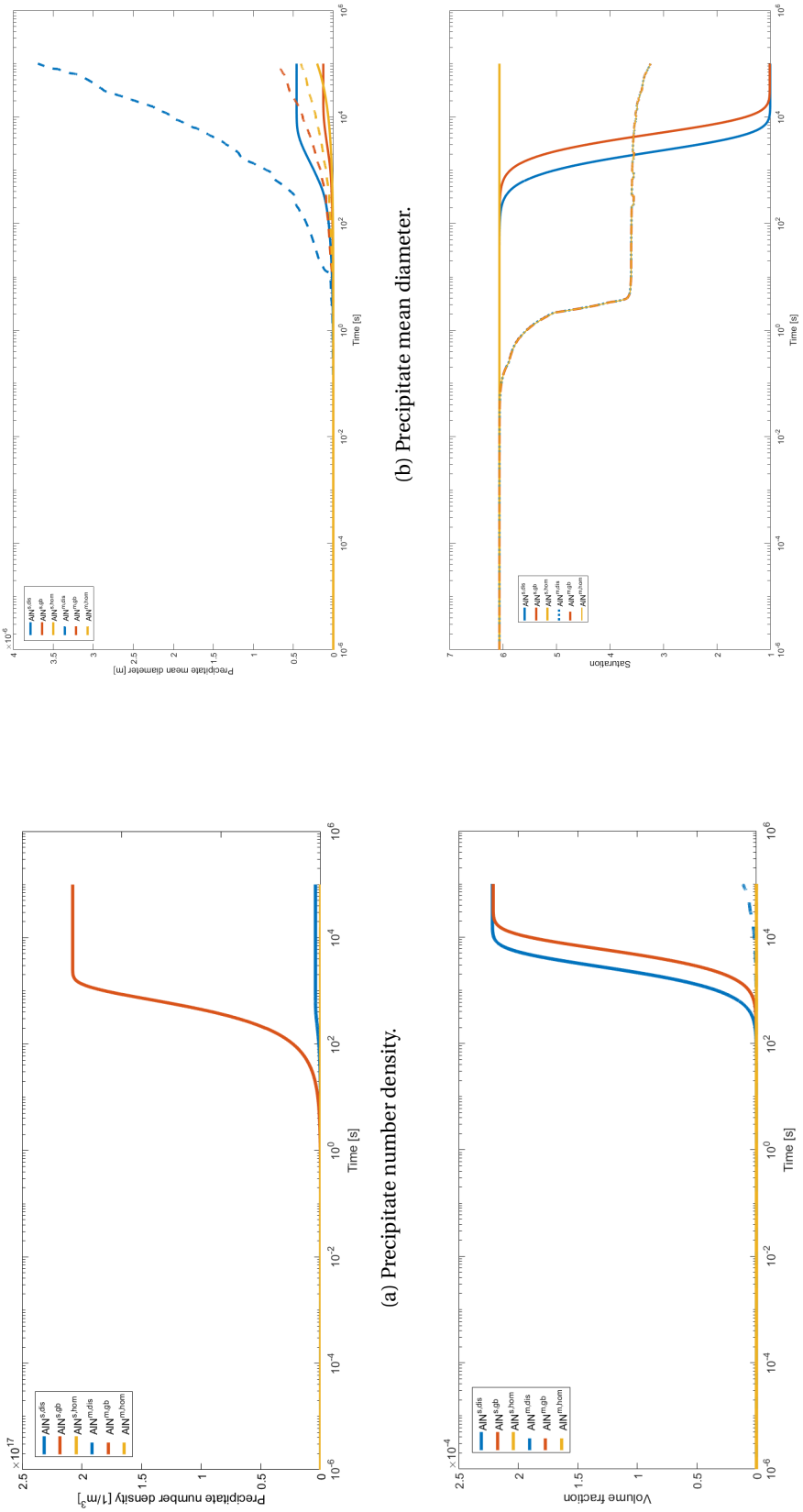

(a) Precipitate number density.

(b) Precipitate mean diameter.

(c) Precipitate volume fraction.

(d) Saturation.

Figure 10.23: The results of the simulation for the *AlN* precipitates with only nucleation of the *AlN* precipitate and at only one nucleation site, indicated with a *s* (single-precipitate, solid line) and the simulation for the *AlN* precipitates influenced by the nucleation of the *NbCN* precipitates and at multiple nucleation sites, indicated with a *m* (multi-precipitate, striped or dashed line), and separated per nucleation site. A blue line is used for nucleation on dislocations, a red line for nucleation on grain boundaries and a yellow line for homogeneous nucleation.

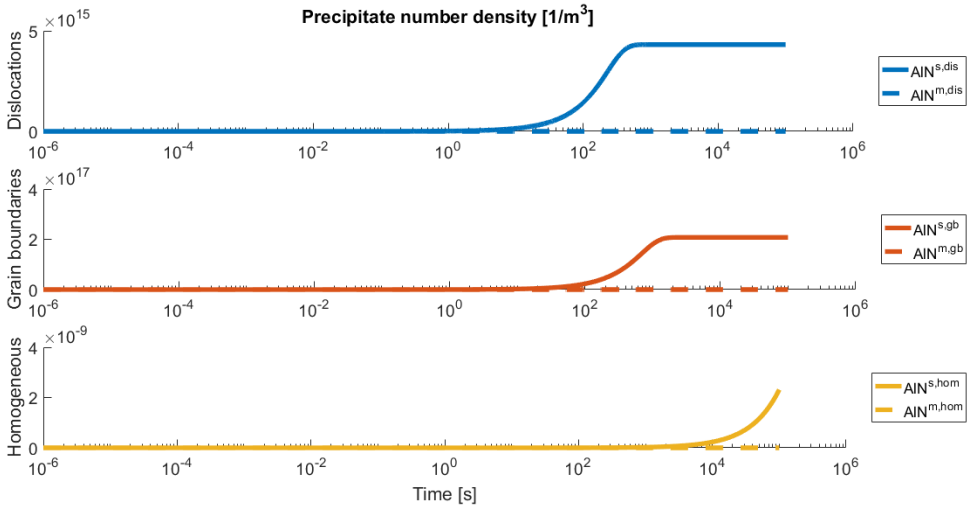

(a) Precipitate number density.

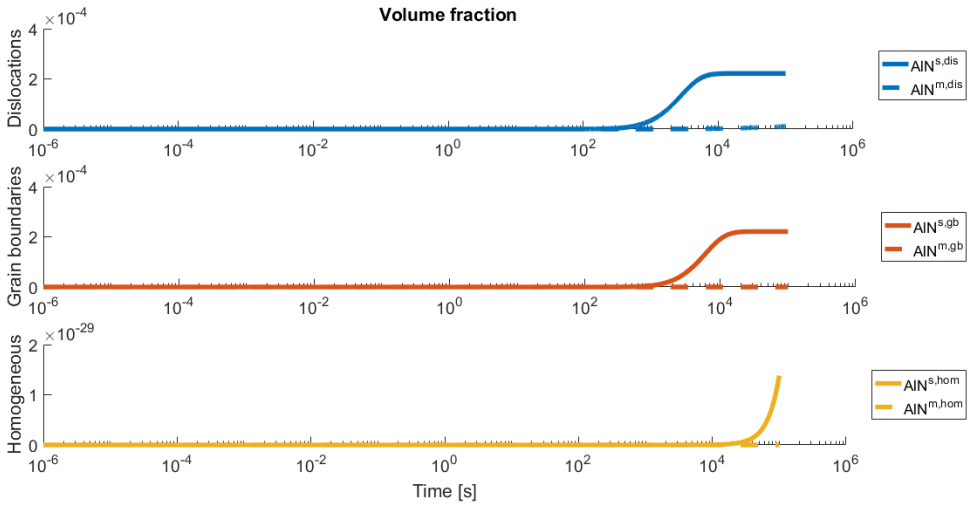

(b) Precipitate volume fraction.

Figure 10.24: The results of the simulation for the AlN precipitates with and without interaction with other precipitate with a different composition and various nucleation sites, plotted at each nucleation site individually.

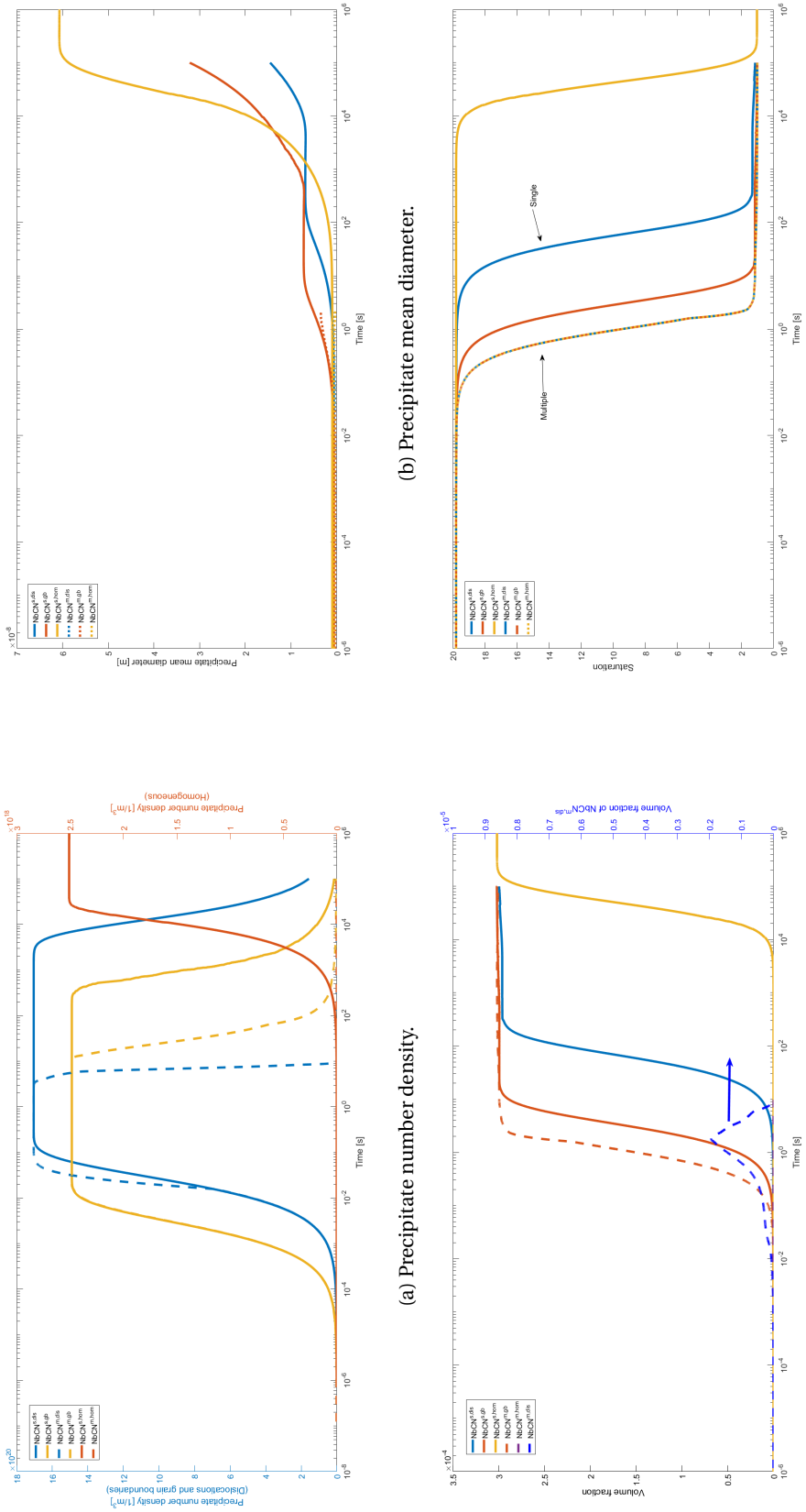

(a) Precipitate number density. (b) Precipitate mean diameter.

(c) Precipitate volume fraction. (d) Saturation.

Figure 10.25: The results of the simulation for the *NbCN* precipitates with only nucleation of the *NbCN* precipitate and at only one nucleation site, indicated with a *s* (single-precipitate, solid line) and the simulation for the *NbCN* precipitates influenced by the nucleation of the *AlN* precipitates and at multiple nucleation sites, indicated with a *m* (multi-precipitate, striped or dashed line), and separated per nucleation site. A blue line is used for nucleation on dislocations, a yellow line for nucleation on grain boundaries and a red line for homogeneous nucleation. For the volume fraction a slightly different line style is used, as indicated in the legend.

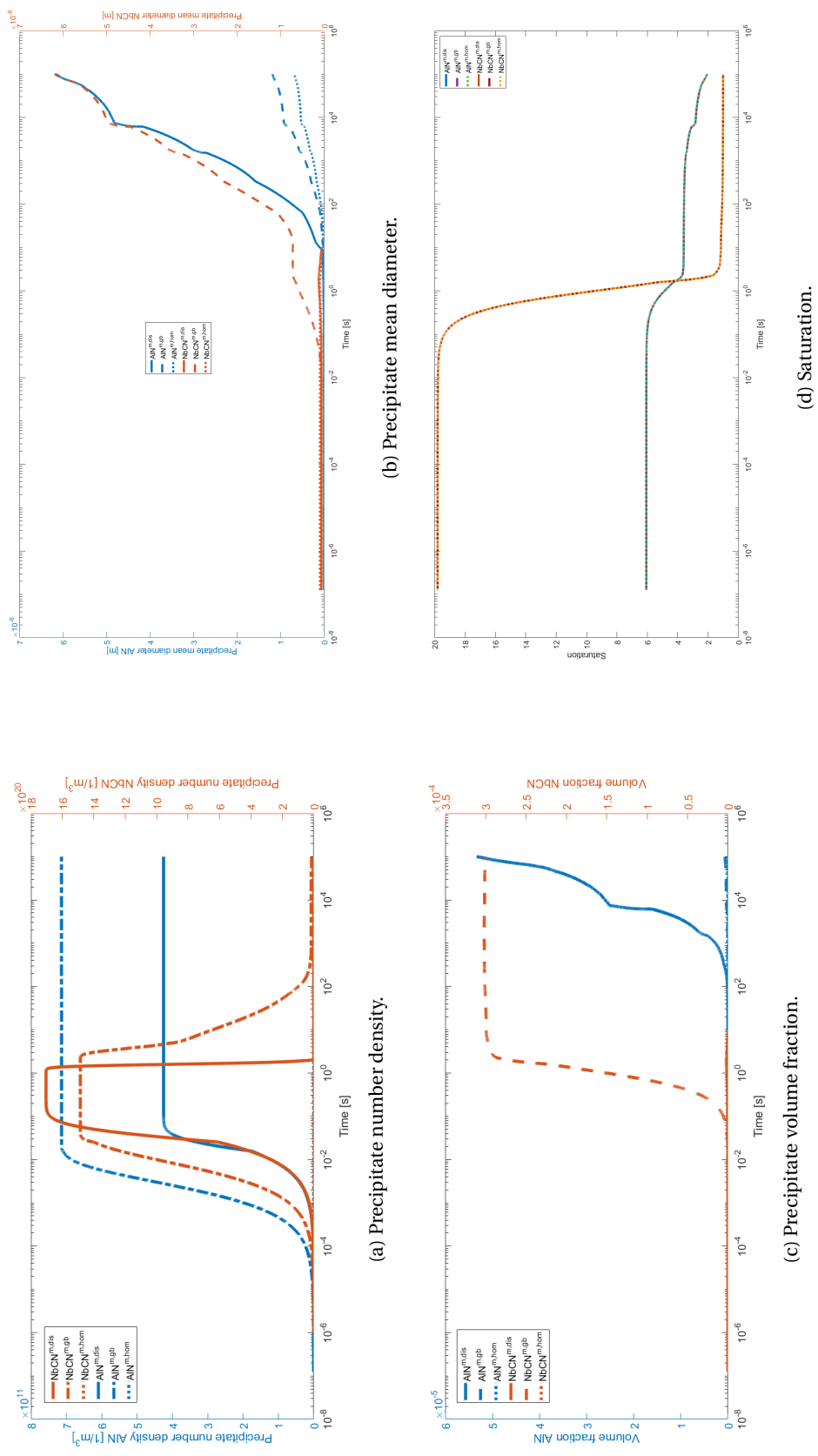

(a) Precipitate number density.

(b) Precipitate mean diameter.

(c) Precipitate volume fraction.

(d) Saturation.

Figure 10.26: The results of the simulation for both the *NbCN* (red lines) and *AlN* (blue lines) precipitates influenced by the nucleation of each other and at multiple nucleation sites, indicated with a *m* (multi-precipitate), and separated per nucleation site. A solid line is used for nucleation on dislocations, a striped-dashed line for nucleation on grain boundaries and a dashed line for homogeneous nucleation.

10.5. Simulation of a non-isothermal case

In the production of steel, the temperature is of great importance. To show the capabilities of the model and the effect on the final results, we enter two time-dependent temperature schemes into the model. There is one main restriction on the temperature scheme we choose, since we the model is currently only developed for austenite (see Figure 2.4 for the range of temperatures). We choose two different temperature schemes, where the first temperature scheme stays below the solvus temperature (Section 10.5.1) and the second temperature scheme increase to above the solvus temperature (Section 10.5.2).

10.5.1. Simulation temperature scheme I

The first temperature scheme is a linear temperature increase as shown in Figure 10.27. It starts at 850 °C and linearly increases to 1000 °C in 140 minutes (=8400 s), where after the temperature stays at a constant 1000 °C. As stated before, the maximum temperature in this temperature scheme is below the solvus temperatures of all precipitates considered in this thesis, see Table 10.2.

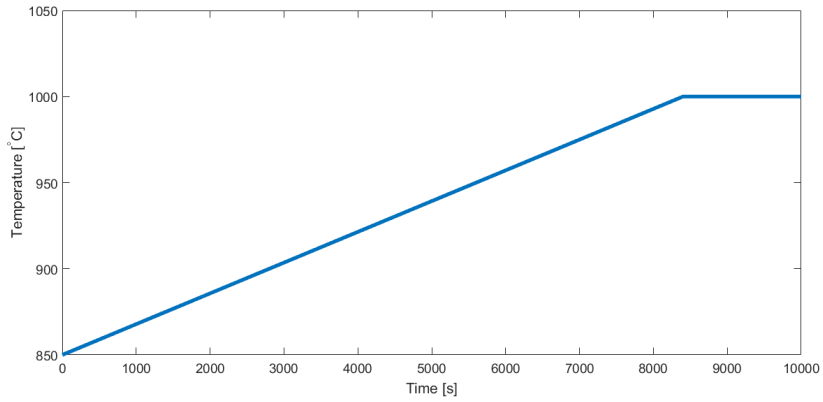

Figure 10.27: Lineair temperature increase I.

For the simulation we use two precipitates, $NbCN$ and AlN, at all three nucleation sites discussed in this thesis: on dislocations, on grain boundaries and homogeneous nucleation. We use a a dislocation density (ρ) of 3.27×10^{14} 1/m^2, the radius of a grain (R_{grain}) of 10^{-6} m and a grain boundary thickness (δ_{gb})of $3a$, where a is the lattice constant of austenite. We use the initial and numerical values given in Chapter 8. Furthermore, the implementation used for just nucleation on grain boundaries and nucleation at the three sites originates from Section 5.2 and for nucleation on dislocations from Chapter 4. The results of the individual precipitate compositions with and without temperature increase are given in Figures 10.28 (for AlN) and 10.29 (for $NbCN$). The combined results are given in Figure 10.30. For the interpretation of the simulation results, the solvus temperatures of the precipitates involved for the chosen alloy N1 (Table 8.3), are given in Table 10.2.

AlN

In Figure 10.28 the results for AlN precipitation at the three nucleation sites with a temperature increase are presented. In each plot, both the simulation with a constant temperature of 850 °C, as well as the simulation with a temperature increase are presented.

Due to the temperature increase, the decrease in precipitate number density is advanced. This leads to a faster decreasing saturation, which even reaches the equilibrium level. However, the volume fraction and the precipitate mean diameter decrease after time, in contrast to the results for a constant temperature. The influence of the temperature increase shows is equal for the different sites, except for the precipitate number density for homogeneous nucleation. However, due to the low nucleation density of 10^{-15} this is not relevant.

NbCN

In Figure 10.29 the results for $NbCN$ precipitation at the three nucleation sites with a temperature increase are presented. In each plot, both the simulation with a constant temperature, as well as the simulation with a temperature increase are presented.

Whereas the results of AlN are equally influenced by the temperature increase for all nucleation sites, the results of $NbCN$ are not. The results for $NbCN$ for homogeneous nucleation and nucleation on dislocations show no difference between the isothermal and non-isothermal scheme. In contrast, the results for nucleation on grain boundaries show differences between the isothermal and non-isothermal scheme. The coarsening stage is slightly delayed, but the growth in the precipitate mean diameter is slowed down. This leads to a decreasing volume fraction due to the dissolution of precipitates. After the dissolution the volume fraction is increasing again.

AlN and $NbCN$

In Figure 10.30 the results for both AlN and $NbCN$ precipitation at the three nucleation sites with a temperature increase are presented.
The interaction between the precipitates is not influenced by the temperature increase. The results are comparable to the results found in Section 10.4 till short before 10^4 seconds. At that moment the temperature increases to such a level that the kinetics slightly change, as can for example be seen in the mean diameter of the AlN precipitates (Figure 10.30b) and the volume fraction (Figure 10.30c). The site with the largest volume fraction differs per precipitate. For AlN precipitates nucleation on grain dislocations gives the highest volume fraction, whereas for $NbCN$ precipitates nucleation on dislocations gives the highest volume fraction. For $NbCN$ precipitation we saw the same behavior in Section 10.3, where nucleation on grain boundaries gave the highest volume fraction when competition between nucleation sites is added. This is mainly caused by the size of the precipitates, which is higher when competition is added.

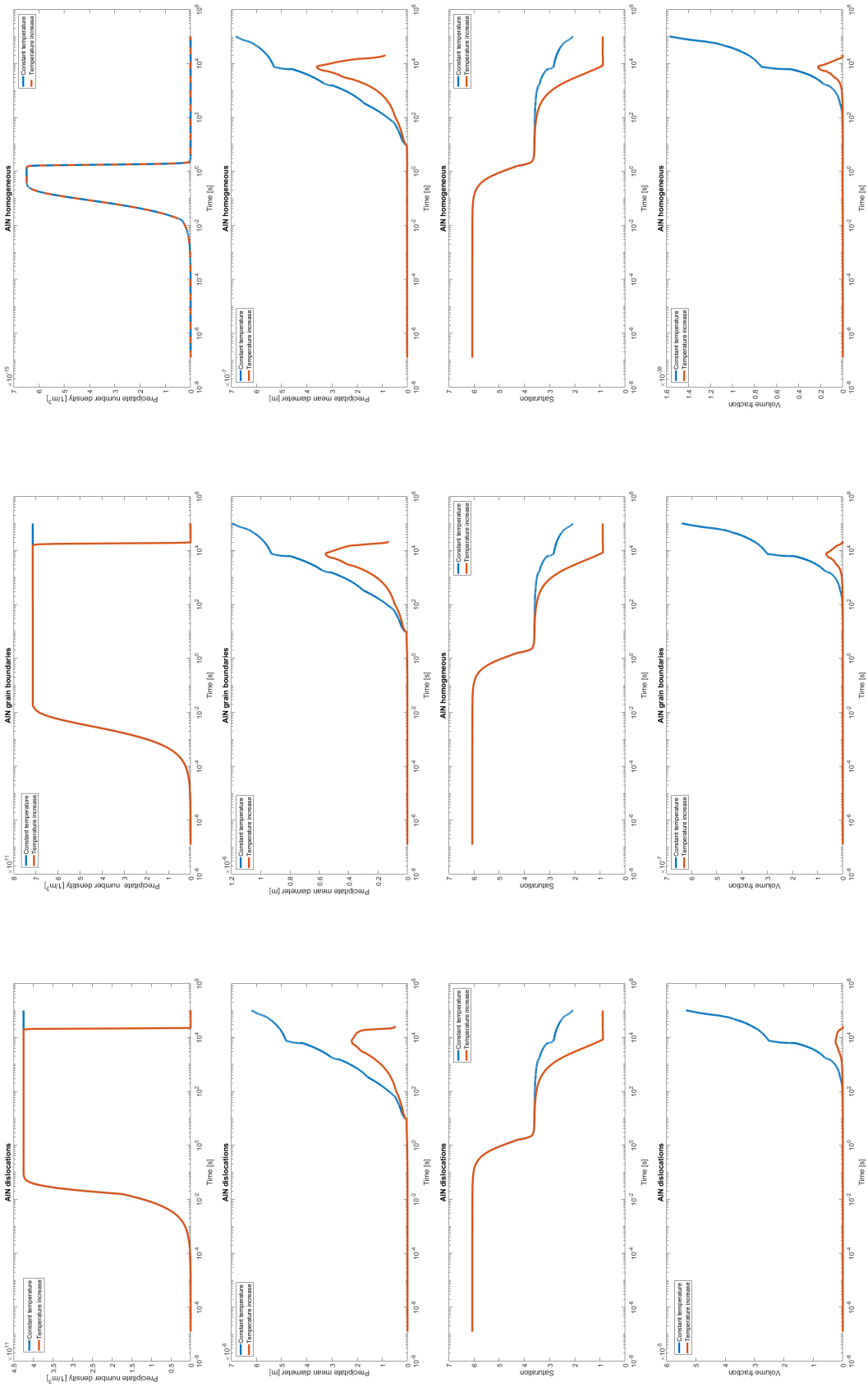

Figure 10.28: The results of simulation for *AlN* with competition and a with a constant temperature of 850 °C (blue lines) and with competition and a linear temperature increase (red lines). The top row is the precipitate number density, the second row the precipitate mean diameter, the third row the saturation and the fourth row the precipitate volume fraction.

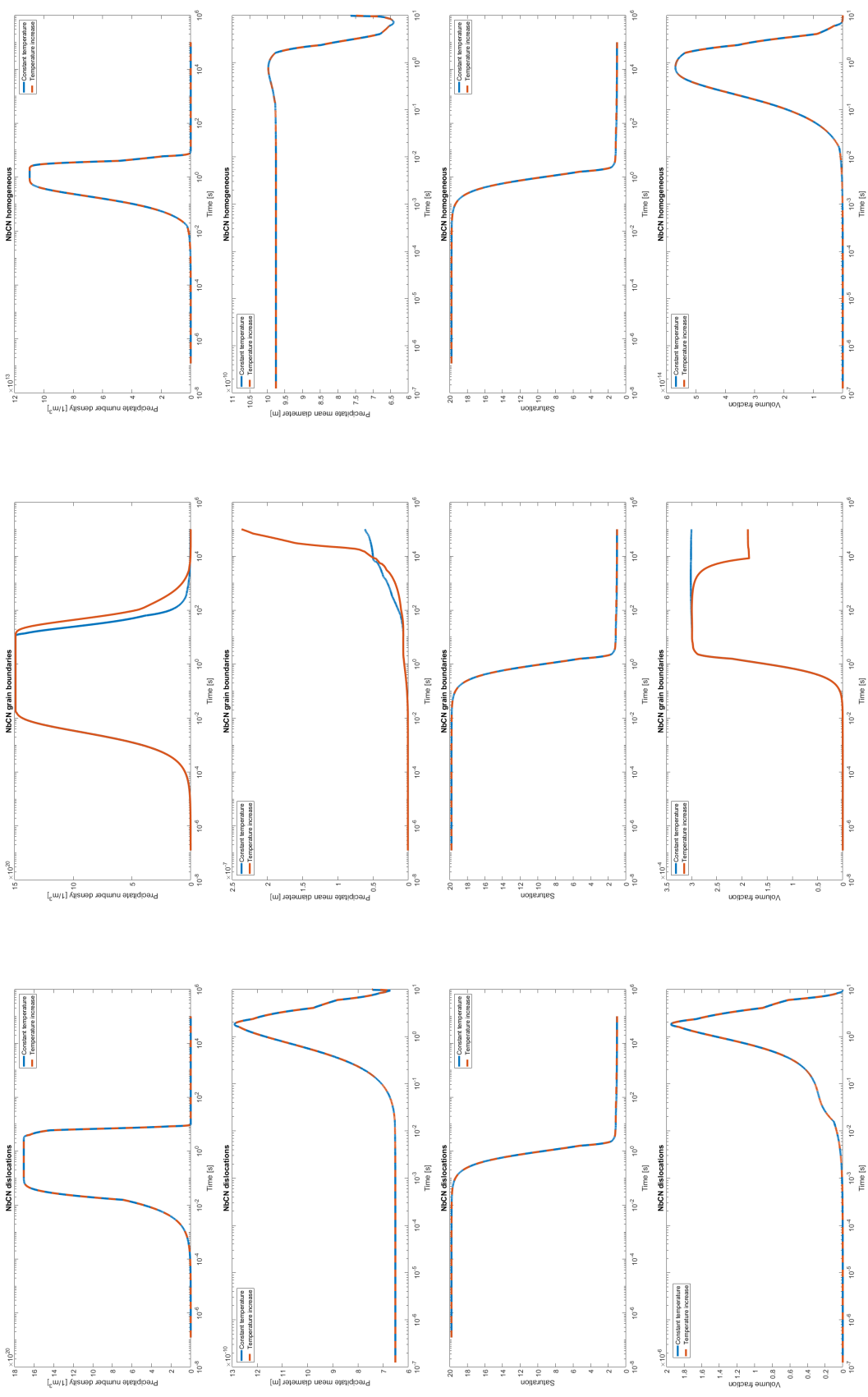

Figure 10.29: The results of simulation for *NbCN* with competition and a with a constant temperature of 850 °C (blue lines) and with competition and a linear temperature increase (red lines). The top row is the precipitate number density, the second row the precipitate mean diameter, the third row the saturation and the fourth row the precipitate volume fraction.

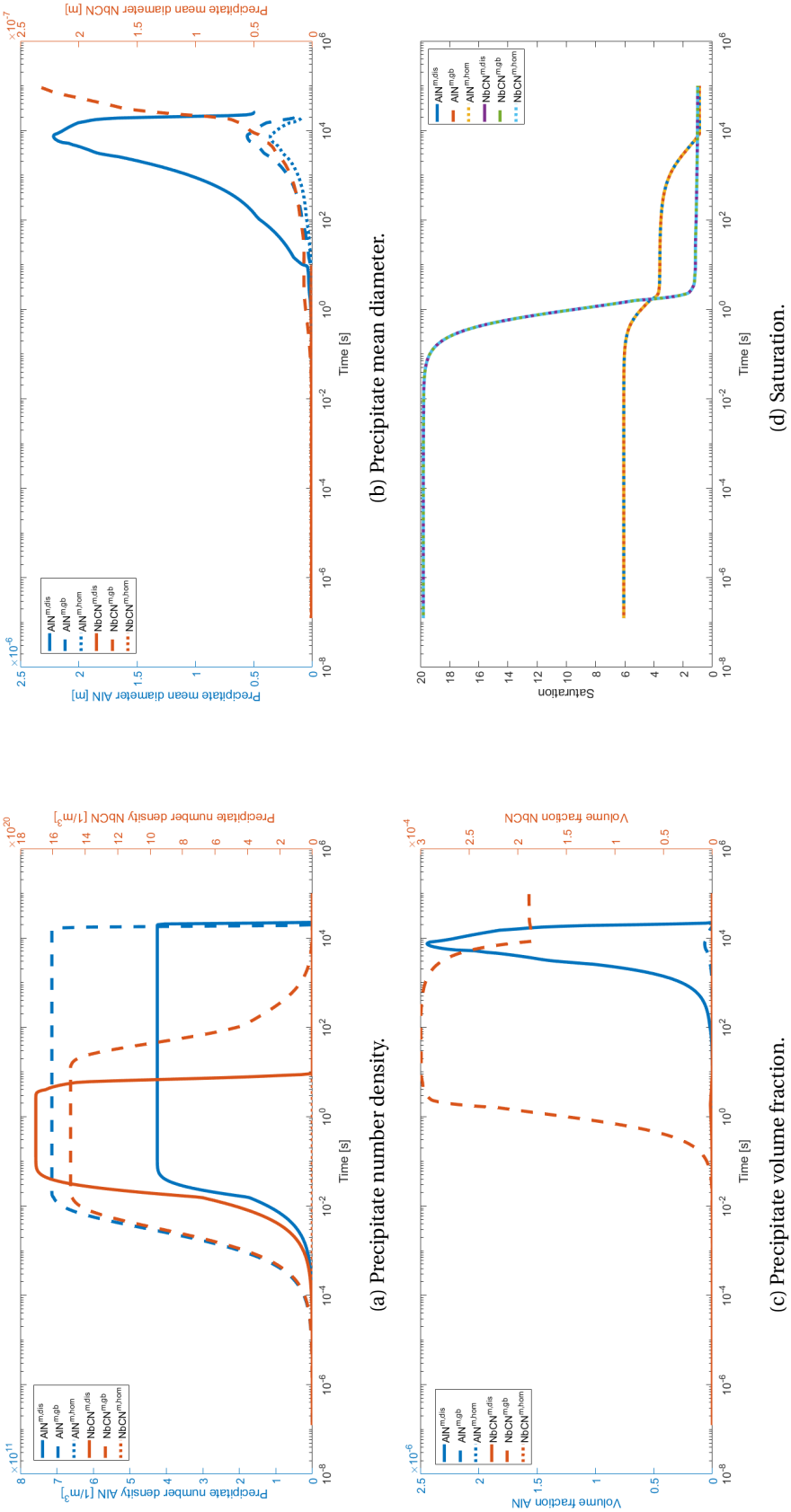

(a) Precipitate number density.

(b) Precipitate mean diameter.

(c) Precipitate volume fraction.

(d) Saturation.

Figure 10.30: The results of the simulation for the *AlN* (blue lines) and *NbCN* (red lines) precipitates, where we use a linear temperature increase at all three nucleation sites (on dislocations, on grain boundaries and homogeneous nucleation). Solid lines are used for nucleation on dislocations, striped lines for nucleation on grain boundaries and dashed lines for homogeneous nucleation.

10.5.2. Simulation temperature scheme II

The second temperature scheme is again a linear temperature increase as shown in Figure 10.31. It starts at from 850 °C and linearly increases to 1350 °C in 30 seconds, where after the temperature stays at a constant 1350 °C. The end temperature of this temperature scheme is above the solvus temperature of all precipitates, see Table 10.2. As described in Chapter 2, precipitation takes place at the hot rolling mill amongst others. When preheating steel slabs, precipitates (especially Nb, V and Ti precipitates) should dissolve as much as possible. The second temperature scheme simulates this progress, where first precipitates are formed and thereafter precipitates should dissolve.

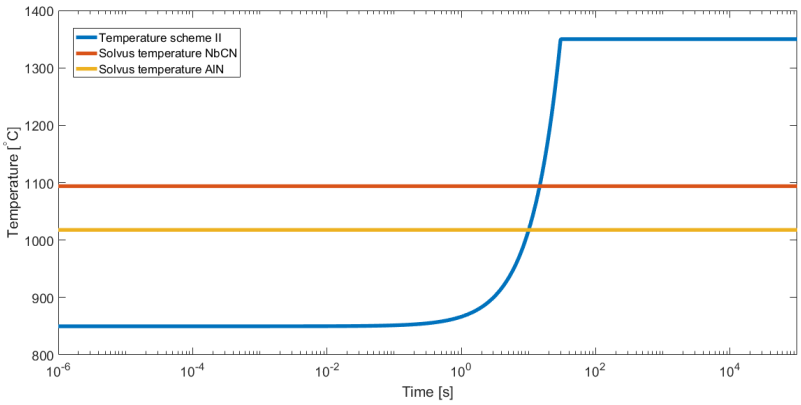

Figure 10.31: Lineair temperature increase II.

For the simulation we use two precipitates, $NbCN$ and AlN, at only one nucleation site, namely on dislocations. The solvus temperatures of these precipitates are illustrated in the temperature scheme in Figure 10.31. We use a a dislocation density (ρ) of 3.27×10^{14} $1/\text{m}^2$ and the initial and numerical values given in Chapter 8. Furthermore, the implementation for nucleation on dislocations originates from Chapter 4. The results of the individual precipitate compositions with and without temperature increase are given in Figures 10.35 (for AlN) and 10.36 (for $NbCN$). The combined results are given in Figure 10.37.

AlN

In Figure 10.35 the results for AlN precipitation on dislocations with a temperature increase are presented. In each plot, both the simulation with a constant temperature of 850 °C, as well as the simulation with a temperature increase are presented.
From Figure 10.31 we find that the temperature will increase to above the solvus temperature of AlN after around 10 seconds. Looking at the results in Figure 10.35 this is exactly the moment where the precipitate number density, the volume fraction and the mean diameter show a strong decrease. This is caused by the dissolving of precipitates at a temperature above the solvus temperature. Indicating the separation between formation of precipitates and dissolving of precipitates gives Figure 10.32.

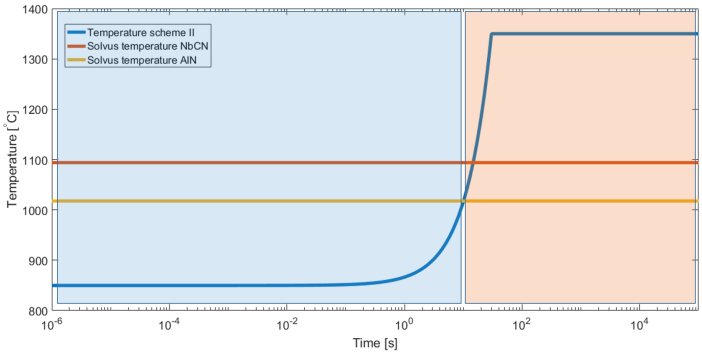

Figure 10.32: Linear temperature increase II, with indication of the precipitate formation time range (blue) and the precipitate dissolving time range (red) of AlN precipitates.

The saturation is the ratio of the matrix product and the solubility product. For higher temperatures the solubility product increases faster, see Figure 10.33, and faster than the matrix product, leading to a faster decrease in saturation than for a constant temperature of 850 °C. For temperatures high above the solvus temperature the precipitates are not stable and the term saturation does not apply.

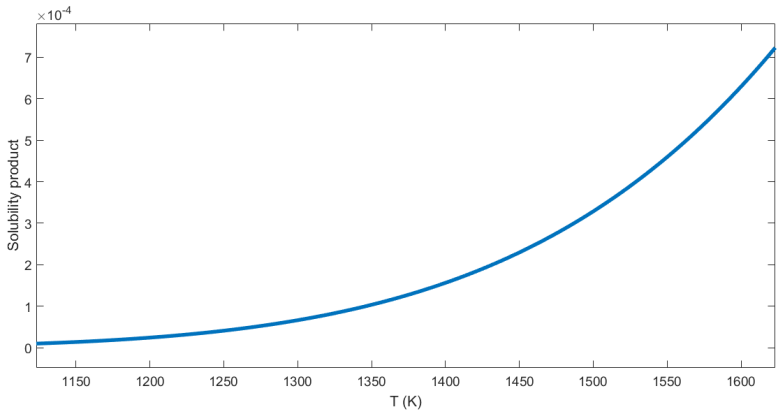

Figure 10.33: The solubility product of AlN for different temperatures between 1120 K (≈ 850 °C) and 1620 (≈ 1350 °C).

$NbCN$

In Figure 10.36 the results for $NbCN$ precipitation on dislocations with a temperature increase are presented. In each plot, both the simulation with a constant temperature of 850 °C, as well as the simulation with a temperature increase are presented.
From Figure 10.31 we find that the temperature will increase to above the solvus temperature of $NbCN$ after around 10 seconds. Looking at the results in Figure 10.36 this is exactly the moment where the precipitate number density, the volume fraction and the mean diameter show a strong decrease, caused by the dissolving of precipitates at a temperature near the solvus temperature. For higher temperatures the solubility product increases faster, see Figure 10.34, and faster than the matrix product. This leads to a faster decrease in the saturation, when comparing it to a simulation with a constant temperature of 850 °C.

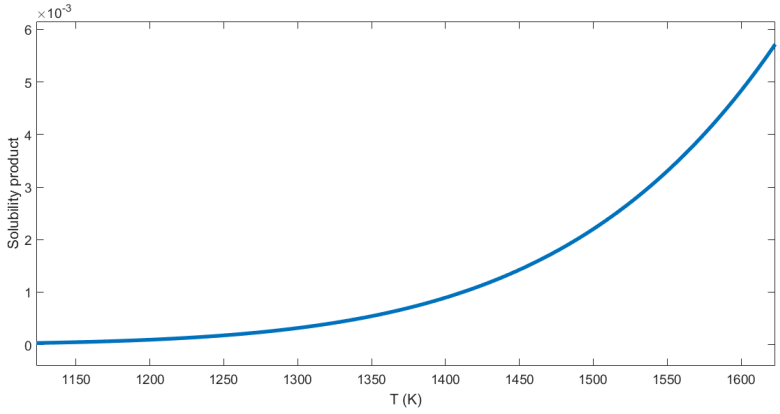

Figure 10.34: The solubility product of $NbCN$ for different temperatures between 1120 K (≈ 850 °C) and 1620 (≈ 1350 °C).

AlN and $NbCN$

As we also saw for the first temperature scheme (Section 10.5.1), the interaction between the precipitates is not hindered by the temperature increase. The results are similar to those found in earlier simulations.
The precipitate number density and volume fraction of both precipitates drop to zero when the temperature increases to above the solvus temperature. The mean diameter also shows a large decrease, but also a little

bump for the $NbCN$ precipitates. This is caused by the large decrease in AlN leading to a short growth of the $NbCN$ precipitates. This effect is only temporarily, since the $NbCN$ precipitates also dissolve, because of the increasing temperature.

When comparing the moment of the large decrease in the precipitate number density, mean diameter, and volume fraction in Figures 10.37a, 10.37b and 10.37c respectively, we find that the drop for the $NbCN$ precipitates comes slightly later than that for the AlN precipitates. This is caused by the moment when the temperature increases to above the solvus temperature. From Figure 10.31 we find that the solvus temperature of AlN is reached earlier than that of $NbCN$.

The decrease in saturation, i.e. ratio of the matrix product and solubility product, is advanced by the temperature increase, as can be seen for both precipitates. This is caused by the fast increasing solubility product for increasing temperature, see Figures 10.33 and 10.34. From Figure 10.37d we find that the moment that the saturation drops below one corresponds to the moment when the temperature increases to above the solvus temperature.

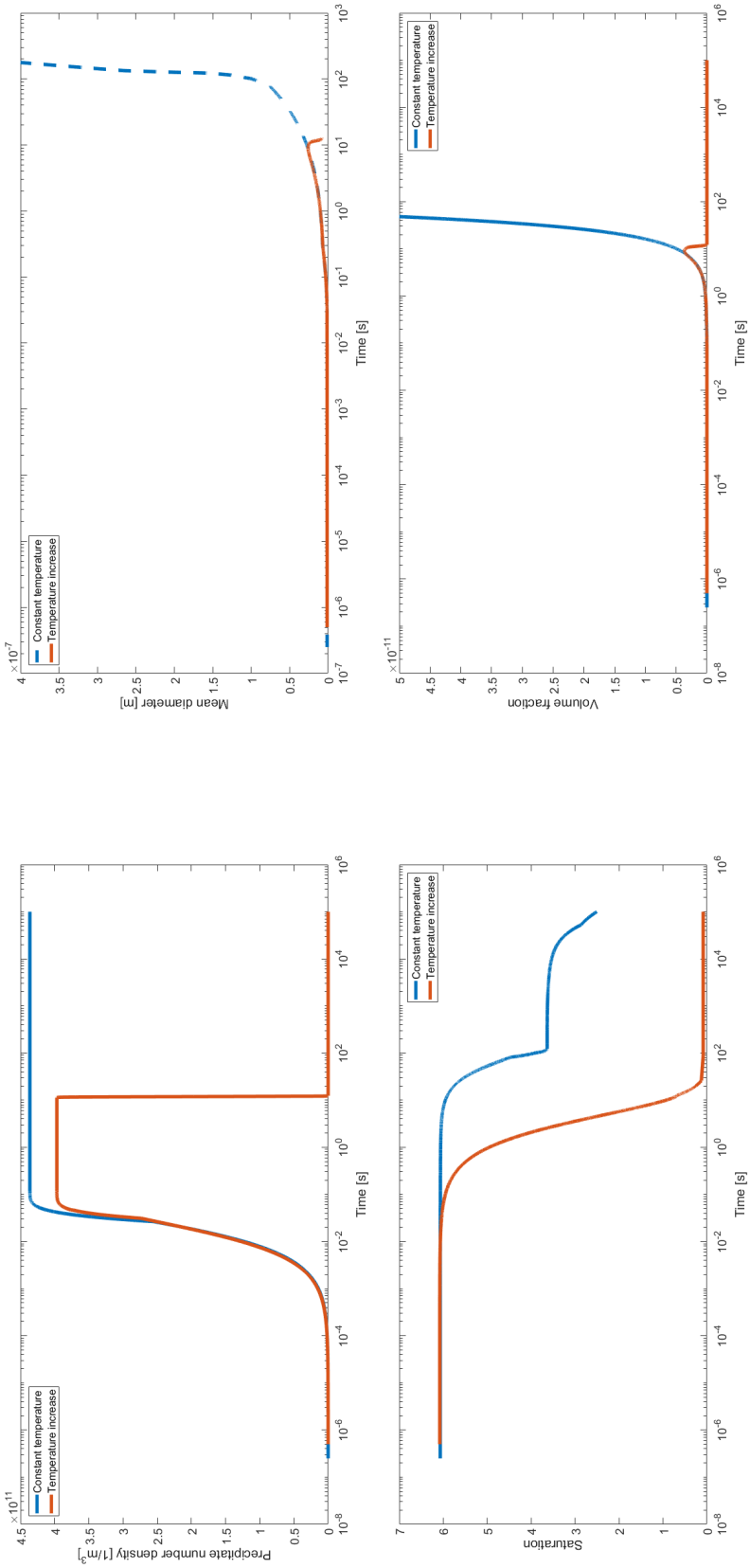

Figure 10.35: The results of simulation for AlN with competition and a with a constant temperature (blue lines) and with competition and a linear temperature increase (red lines), at one nucleation site, namely on dislocations. The plots for the mean diameter and volume fraction have adjusted axes to show the influence of the temperature increase in contrast to a constant temperature.

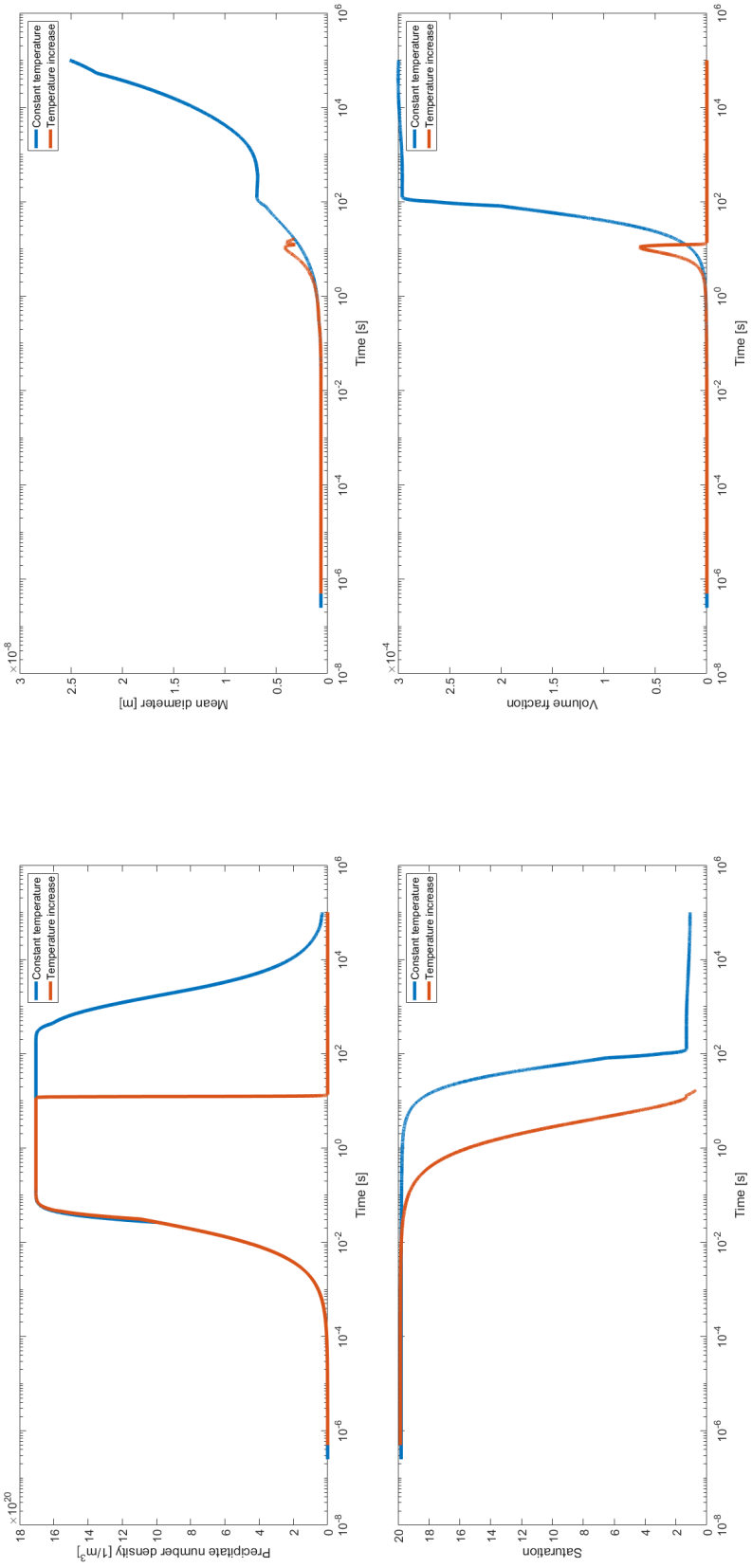

Figure 10.36: The results of simulation for $NbCN$ with competition and with a constant temperature and linear temperature increase, at one nucleation site, namely on dislocations.

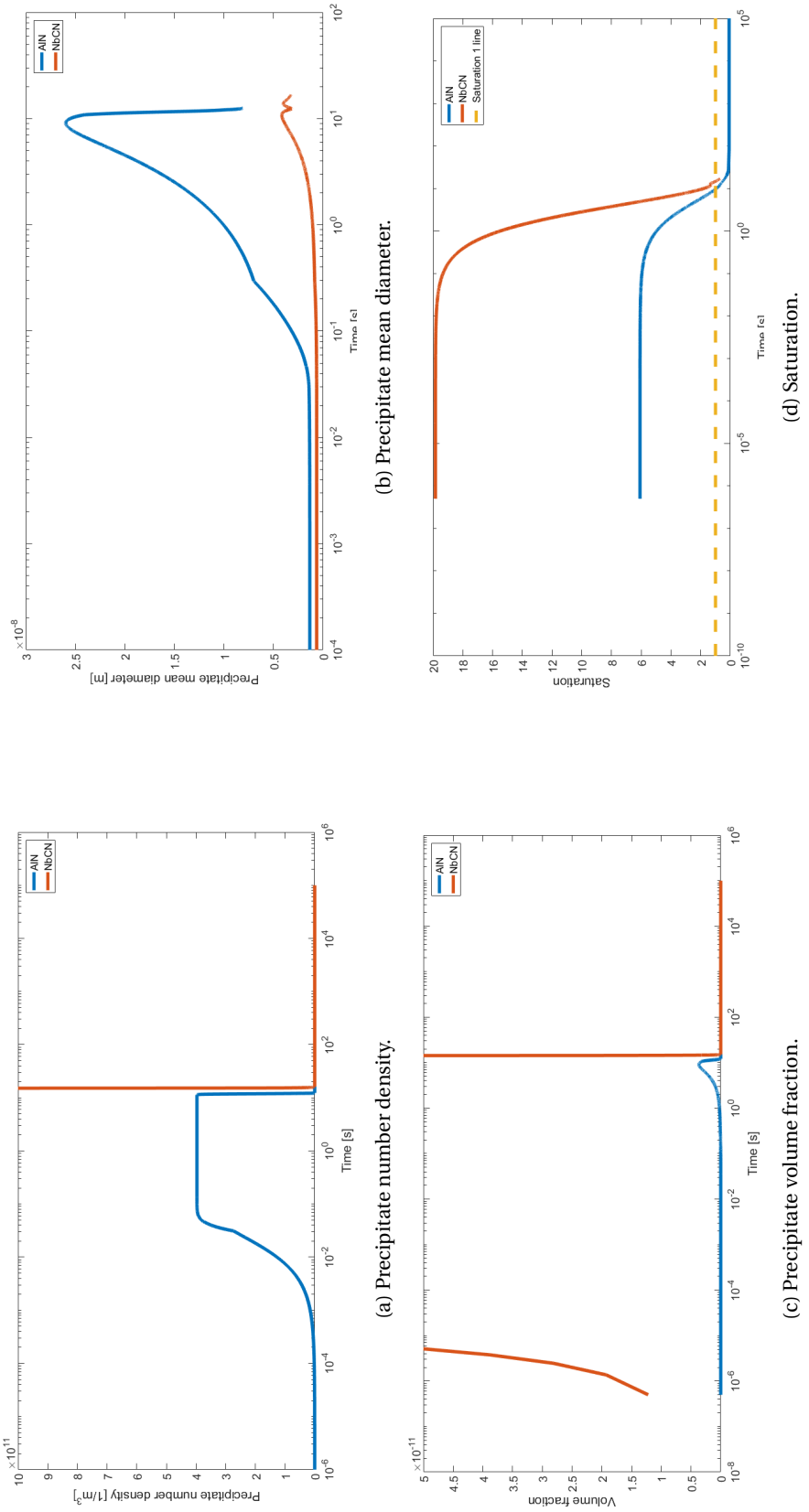

(a) Precipitate number density. (b) Precipitate mean diameter.

(c) Precipitate volume fraction. (d) Saturation.

Figure 10.37: The results of the simulation for the *NbCN* and *AlN* precipitates with competition and with a linear temperature increase, at one nucleation site, namely on dislocations. The axes of some results are altered to correctly compare the timing of the precipitation kinetics.

10.6. Dynamical dislocation density

The model described in this thesis is based on the model by Robson (2014) and Den Ouden (2015). However, the model development started at the model of Zurob et al. (2002). The definition of the nucleation rate and growth rate for example originate from Zurob et al. (2002). Zurob et al. (2002) introduced a model which did not only describe the kinetics of precipitation on dislocations, but also linked it to a recrystallisation and recovery model. Adding these recrystallisation and recovery to the current model would complete the model, but also make the implementation a lot more extensive and beyond the scope of this thesis.

To get an impression of the effect of a dynamical dislocation density, we enter a (user defined) time dependent dislocation density into the model and analyse the effects. We choose two types of dynamic (time-dependent) dislocation densities. The first type is an increasing step-by-step dynamic dislocation density and the second type is a more realistic, decreasing dynamical dislocation density.

The dislocation density ρ occurs twice in the precipitation model.

1. In the maximum number of potential nucleation sites N_{total}, which is defined by (Equation (3.4))

$$N_{total} = \frac{F\rho}{b}.$$

2. In the effective diffusion coefficient D_{eff}, which is defined by (Equation (3.20))

$$D_{eff} = D_{pipe}\pi b^2\rho + D_{bulk}(1-\pi b^2\rho).$$

For the simulation we use two precipitate compositions $NbCN$, and AlN, and at only one nucleation site, namely dislocations.

10.6.1. Simulation step-by-step dislocation density

For the simulation we use a temperature of 850 °C and the initial and numerical values given in Chapter 8. Furthermore, the implementation originates from Chapter 4.
The step-by-step dislocation density as we used in our simulation is given in Figure 10.38.

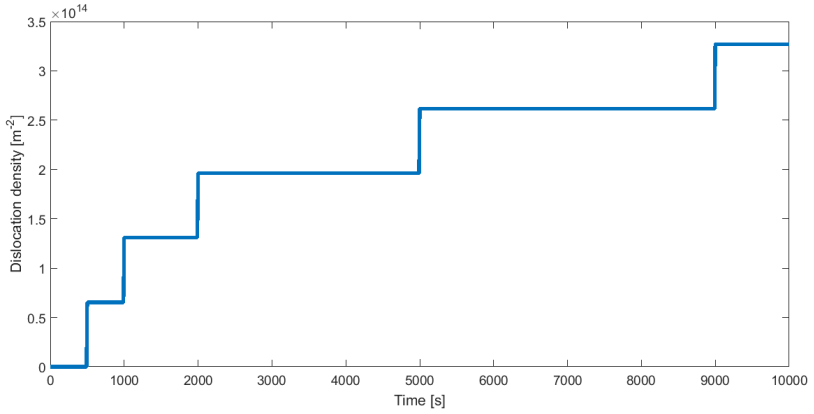

Figure 10.38: Time dependent step-by-step (increasing) dislocation density .

The maximum level of the dislocation density is 3.27×10^{14} 1/m^2, which is equal to the constant dislocation density we have chosen in earlier simulations. We started the simulation with a matrix free of precipitates. Since the step-by-step dislocation density is zero at the beginning of the simulation for a short time period and we only consider precipitation on dislocations, no precipitates can nucleate in this first time interval. In this way we postpone the nucleation of the $NbCN$ precipitates. The results for the step-by-step dislocation density are found in Figure 10.39.

AlN

We find that nucleation only starts when the dislocation density is larger than zero, as expected, since we only consider nucleation on dislocations. The precipitate number density has a large increase at the moment when the dislocation density is larger than zero and nucleation starts, and stays at a stable level after that. The precipitate mean diameter keeps increasing, even when the precipitate number density has stabilised, meaning coarsening is not yet active, and pure growth takes place. Looking at the volume fraction and the saturation, the equilibrium levels are not yet reached within the given time range. Postponing the nucleation by using a step-by-step increasing dislocation density instead of a constant dislocation density of 3.27×10^{14} $1/\mathrm{m}^2$, does not have big effects on the results for larger times. This is caused by the relatively long time intervals that are chosen for the step-by-step dislocation density. Choosing smaller time intervals for each step could increase the visibility of the effects of the step-by-step dislocation density increase.

NbCN

As for the *AlN* precipitates, nucleation only starts when the dislocation density is larger than zero. In contrast to the *AlN* precipitates, coarsening does take place, since the precipitate number density decreases, where the precipitate mean diameter increases. Looking at the volume fraction and the saturation of *NbCN* we see that the equilibrium levels are reached within the given time range, agreeing with the fact that coarsening takes place and no nucleation exists anymore. Postponing the nucleation by using a step-by-step increasing dislocation density causes a very fast nucleation, no pure growth, but a similar coarsening behavior to that found using a constant dislocation density.

AlN and *NbCN*

The precipitate number density of *NbCN* is orders larger than that of *AlN*, agreeing with earlier results. Even though the dislocation density is low in the beginning, the *NbCN* precipitates still reach the equilibrium saturation level of one, in contrast to the *AlN* precipitates, which do not reach their equilibrium saturation level within the given time range.

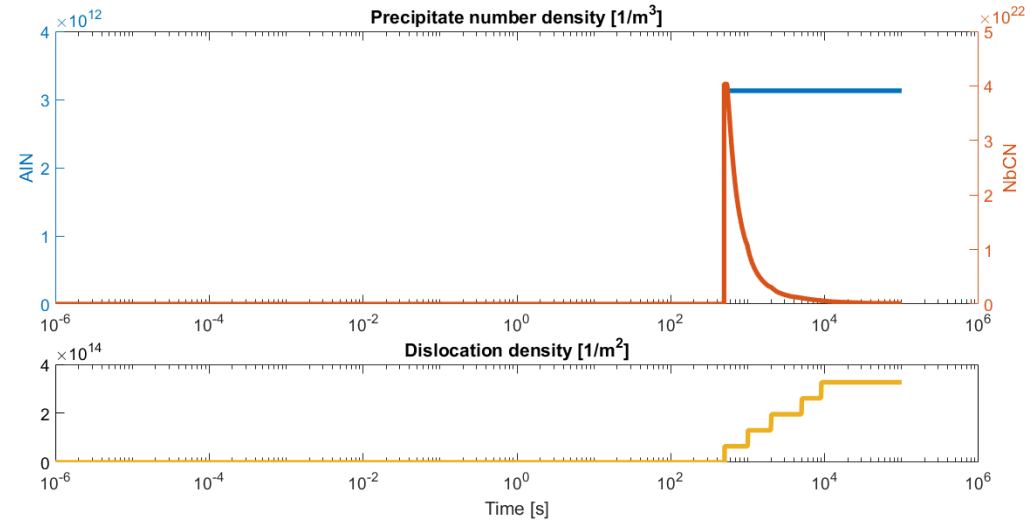

(a) Precipitate number density.

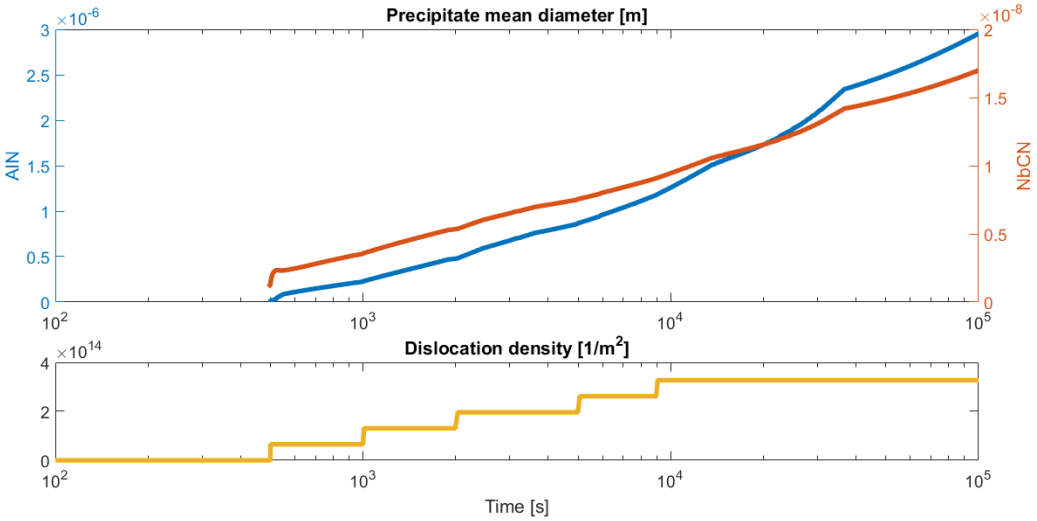

(b) Precipitate mean diameter.

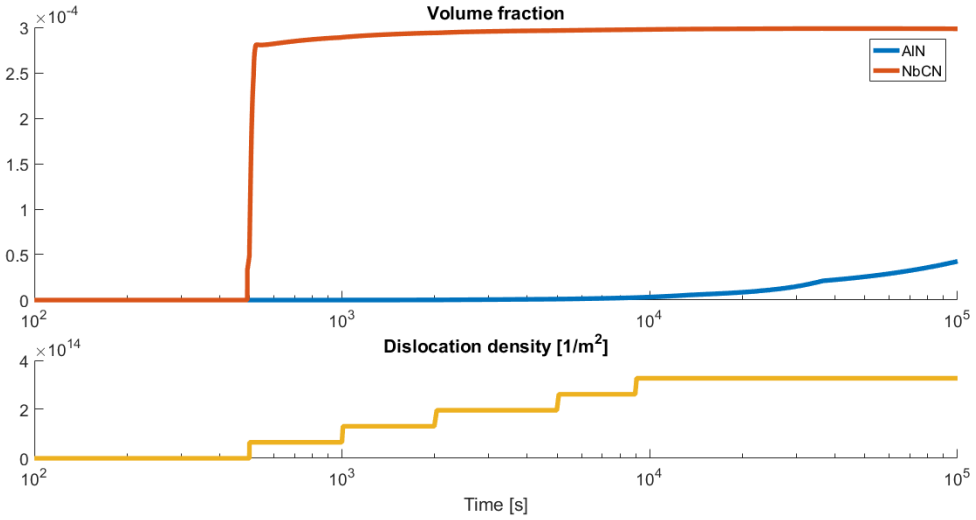

(c) Precipitate volume fraction. (The x-axis is narrowed, to show more detail where the volume fraction is away from zero.)

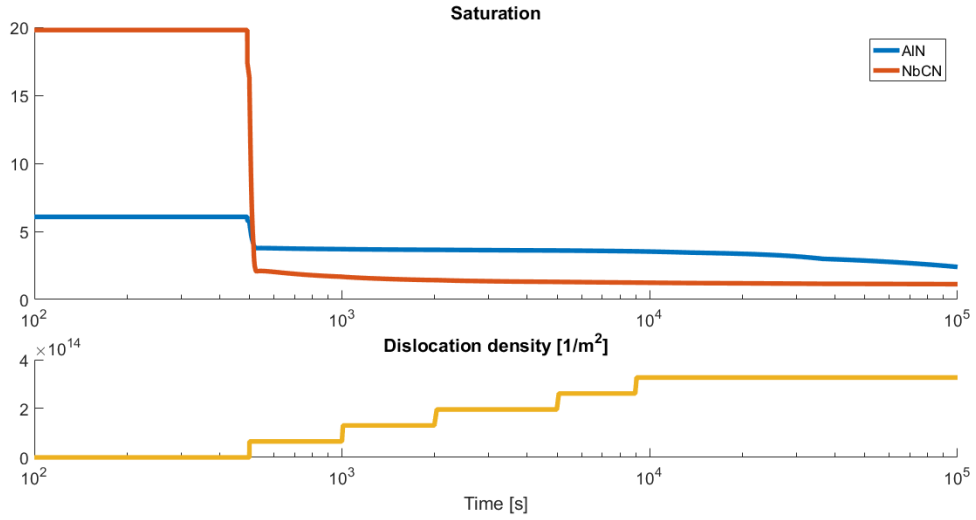

(d) Saturation. (The x-axis is narrowed, to show more detail where the saturation is away from its starting level.)

Figure 10.39: The results of the simulation for the AlN (blue line) and $NbCN$ (red line) precipitates, where we use a step-by-step time dependent dislocation density and simulate only at one nucleation site: on dislocations.

10.6.2. Simulation realistic dislocation density

Besides the step-by-step time dependent dislocation density, we introduce a second type dynamical dislocation density. This dynamical dislocation density was obtained using the model by Zurob et al. (2002), thus, including the coupling between precipitation and recrystallisation and recover. The simulation and corresponding results from this model are found by Kranendonk (2005). In the current model, coupling to recovery and recrystallisation is yet absent: this dislocation density is only used to demonstrate the possibilities of the model. Next to the fact that the simulations in this section are multi-precipitate, it should be emphasised that the results of Kranendonk (2005) do include the coupling of the kinetics of dislocations and precipitation, and therefore can not be compared to the results found in this thesis. The dislocation density as function of the time is given in Figure 10.40.

For the simulation we use a temperature of 850 °C and the initial and numerical values given in Chapter 8. Furthermore, the implementation originates from Chapter 4. The results for the realistic dislocation density are found in Figure 10.42.

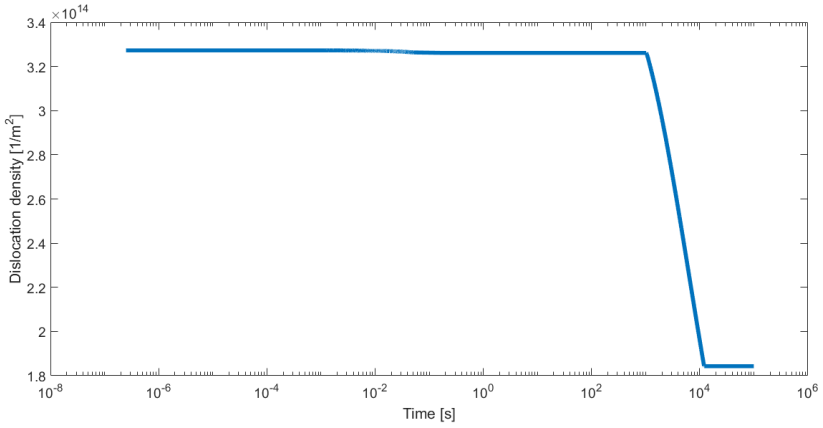

Figure 10.40: Time dependent dislocation density based on data by Kranendonk (2005) (decreasing).

The results in 10.42 are very similar to the results found in Section 10.2 for the individual precipitate compositions and the interaction between them. We find that the nucleation, growth and coarsening stages are not hindered by the decreasing dislocation density at the end of the simulation. The decrease in the dislocation density is too little and comes too late to have a large influence. When using a faster decreasing dislocation density, as given in Figure 10.41[1], the effect is better visible, as shown in Figures 10.43 and 10.44.

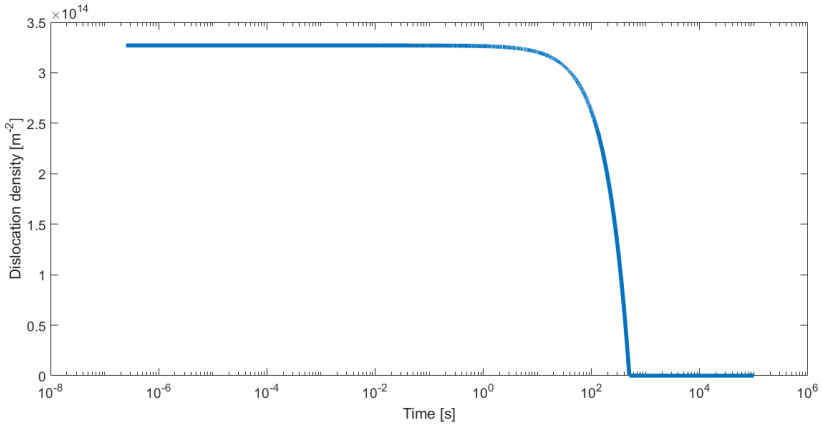

Figure 10.41: Fast decreasing, time dependent dislocation density.

[1] Note that the y-axes of Figures 10.40 and 10.41 are different. The minimum value of Figure 10.40 is 1.8×10^{14}, while the minimum value of Figure 10.41 is 0.

Since the goal of this section is to show the effects of a dynamic dislocation density, we will further elaborate on the results of the simulation using the fast decreasing dislocation density presented in Figures 10.43 and 10.44.

AlN

In Figure 10.43 the results for AlN precipitation on dislocations with a decreasing dislocation density are presented. In each plot, both the simulation with a constant dislocation density of 3.27×10^{14} $1/\text{m}^2$, as well as the simulation with a decreasing dislocation density are presented.
Due to the decreasing dislocation density, we find that the precipitates that nucleate have a smaller diameter. This agrees with the volume fraction that is orders smaller when a decreasing dislocation density is chosen. Also the saturation is influenced, since the drop in saturation at the end of the time range is not present anymore caused by the decreasing dislocation density. The precipitate number density is not influenced by the dislocation density.

NbCN

In Figure 10.44 the results for $NbCN$ precipitation on dislocations with a decreasing dislocation density are presented. In each plot, both the simulation with a constant dislocation density of 3.27×10^{14} $1/\text{m}^2$, as well as the simulation with a decreasing dislocation density are presented.
The precipitate number density of $NbCN$ is influenced by the decreasing dislocation density. The precipitate number density stays longer at the constant maximum level, and coarsening is delayed, also causing smaller precipitates within the same time range. This does not influence the volume fraction and the saturation, which still reach their equilibrium levels.

AlN and *NbCN*

The precipitate mean diameters of both precipitates are lower, caused by delayed coarsening kinetics. The AlN precipitates are the most hindered by the decreasing dislocation density, as shown by its volume fraction and saturation.

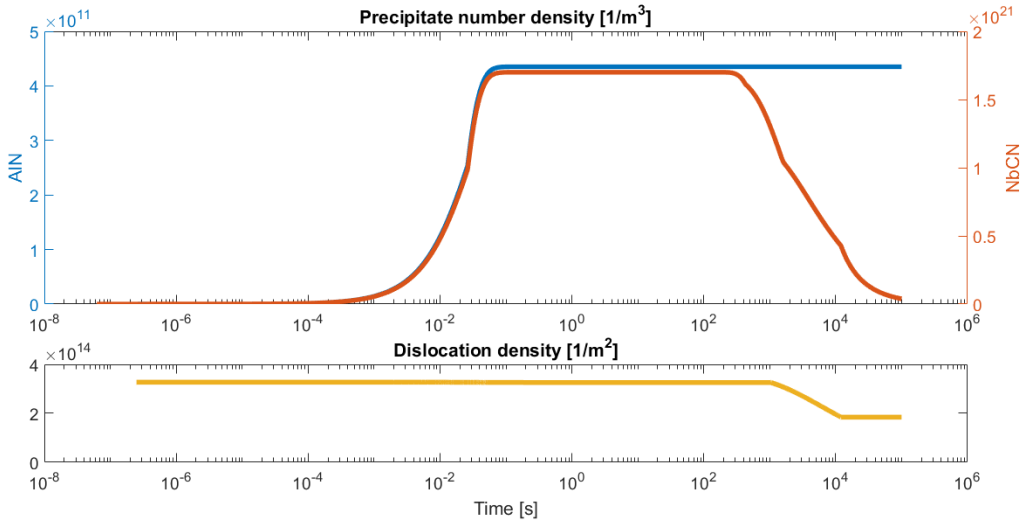

(a) Precipitate number density.

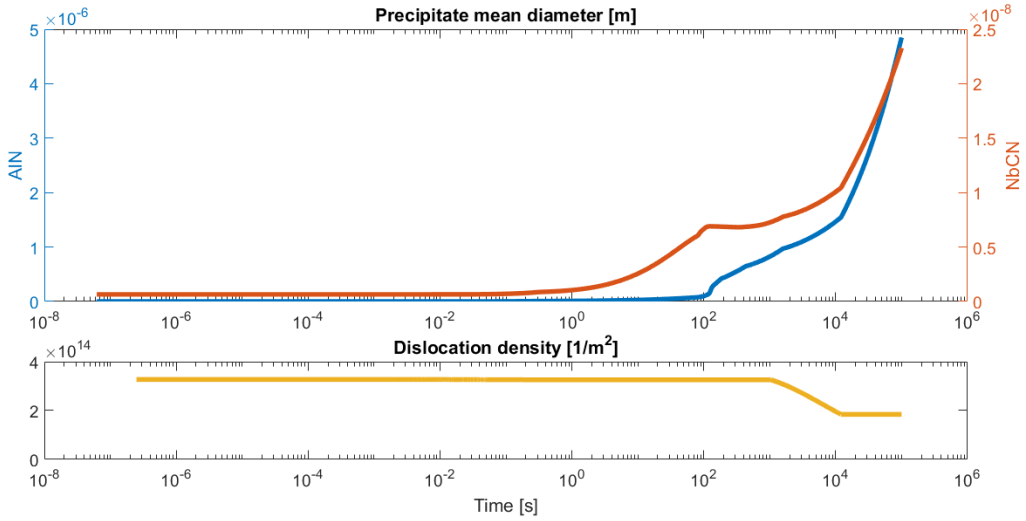

(b) Precipitate mean diameter.

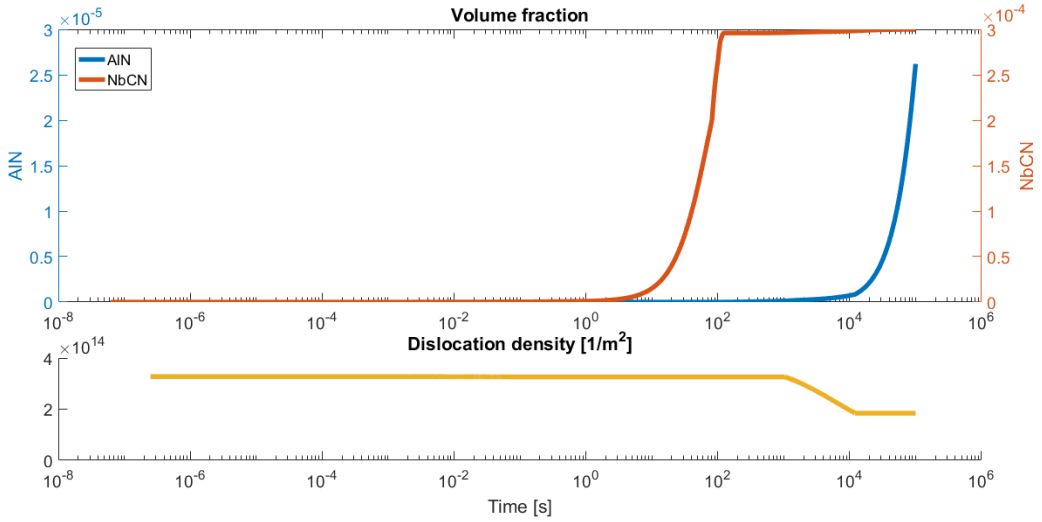

(c) Precipitate volume fraction.

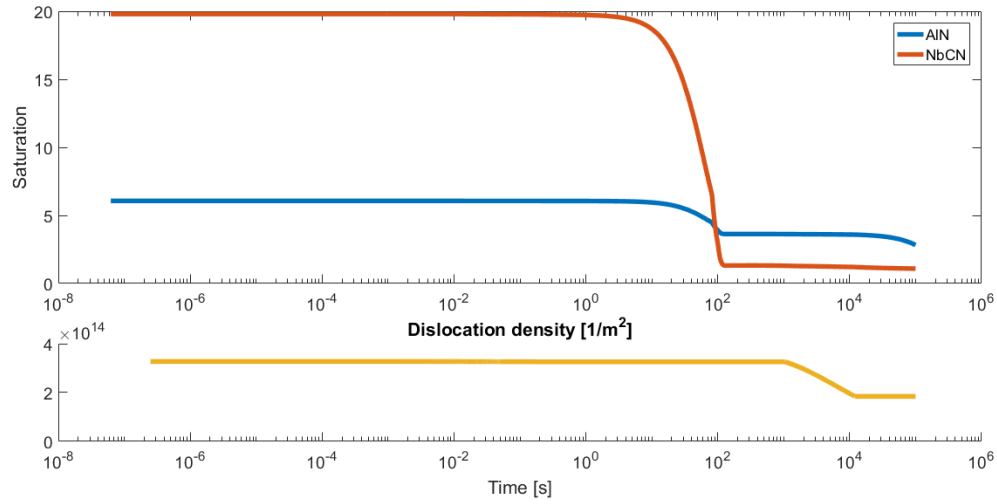

(d) Saturation.

Figure 10.42: The results of the simulation for the AlN (blue line) and $NbCN$ (red line) precipitates, where we use a time dependent dislocation density based on results found by Kranendonk (2005) and a constant dislocation density. We simulate only at one nucleation site: on dislocations.

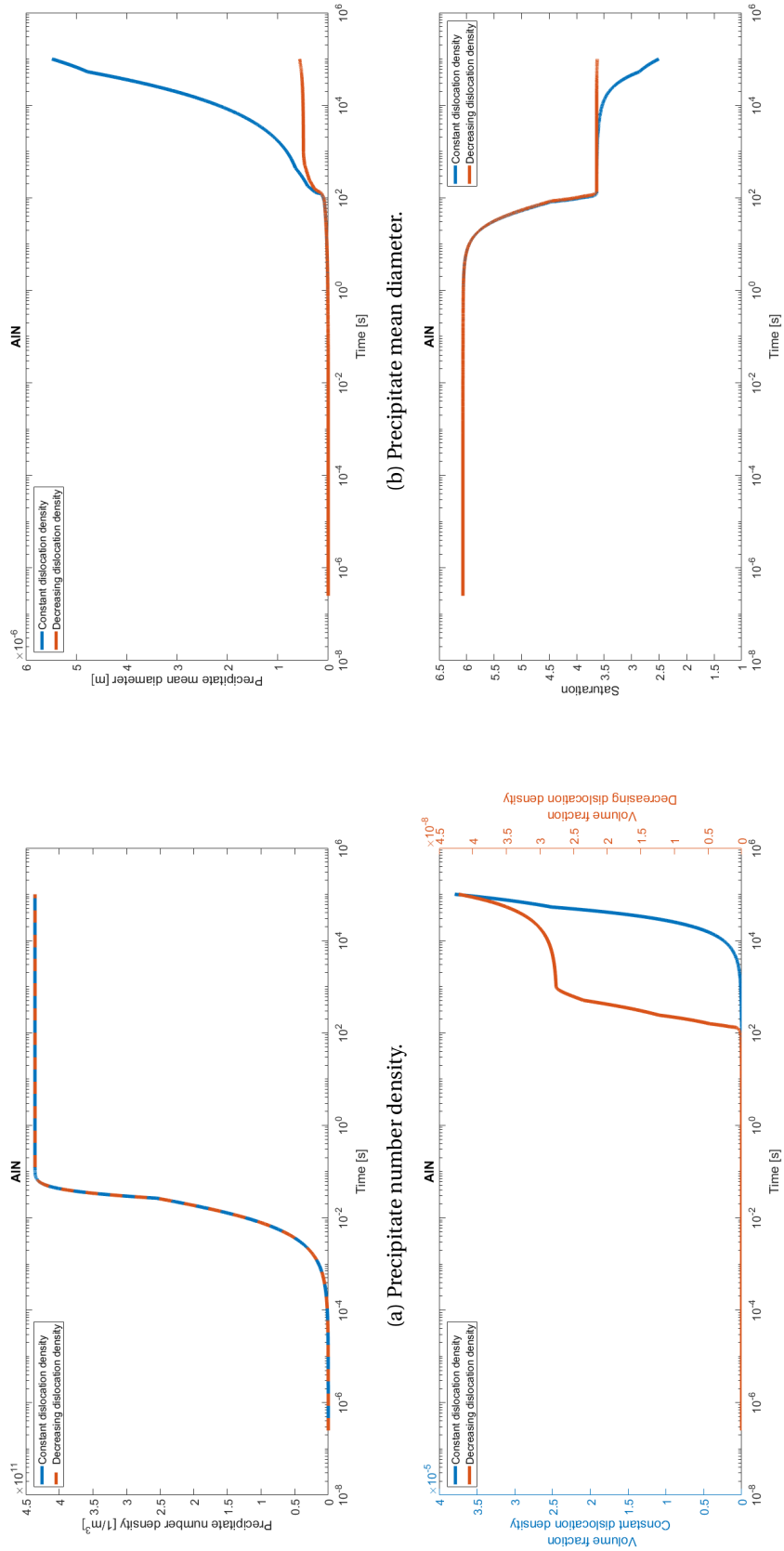

(a) Precipitate number density.

(b) Precipitate mean diameter.

(c) Volume fraction.

(d) Saturation.

Figure 10.43: The results of the simulation for the *AlN* precipitates, where we use a time dependent decreasing dislocation density (red line) and a constant dislocation density (blue line). We simulate only at one nucleation site: on dislocations.

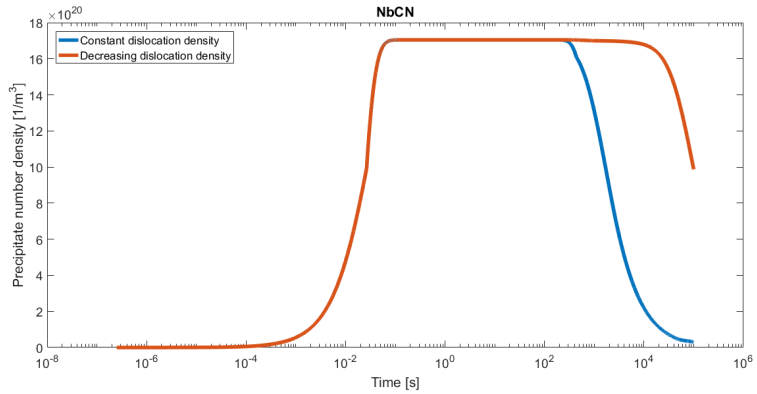

(a) Precipitate number density.

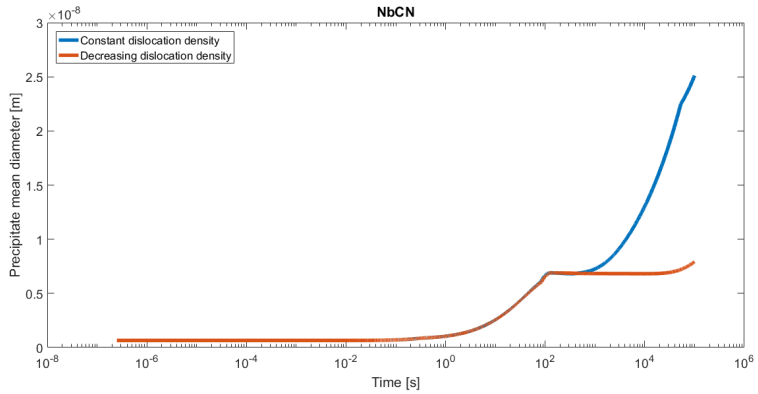

(b) Precipitate mean diameter.

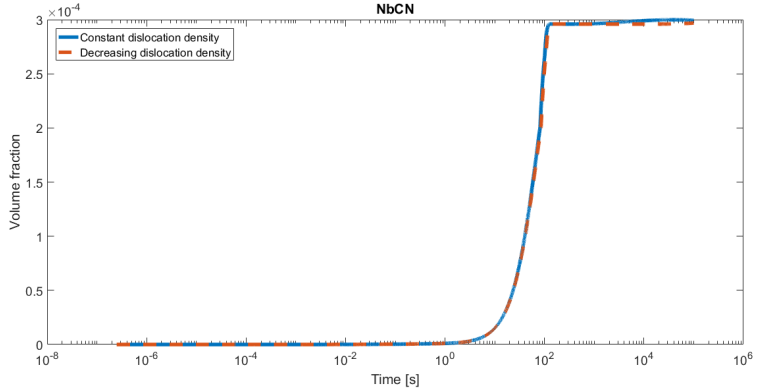

(c) Volume fraction.

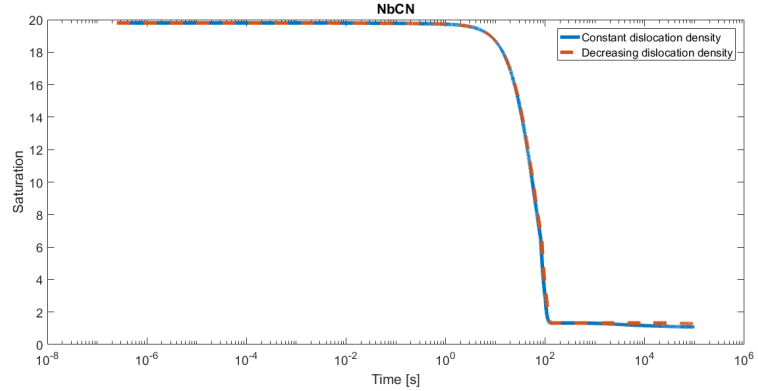

(d) Saturation.

Figure 10.44: The results of the simulation for the $NbCN$ precipitates, where we use a time dependent decreasing dislocation density (red line) and a constant dislocation density (blue line). We simulate only at one nucleation site: on dislocations.

11

Concluding remarks

In the literature study by Vonk (2016) a precipitation model by Zurob et al. (2002) was implemented and analysed. From this study it became clear that the Zurob model needed a number of improvements and extensions for applications to modern steel grades. The mean radius approach used in this model was the most limiting element of this model. In this master thesis a distribution model was developed, based on the KWN model by Robson (2014) and Den Ouden et al. (2013), to describe the precipitation without the limitation of a mean radius approach.

The distribution model contains the following partial differential equation, describing the time evolution of a newly introduced function ϕ,

$$\frac{\partial \phi}{\partial t} = -\frac{\partial [v\phi]}{\partial R} + S, \tag{3.1}$$

in which $\phi \equiv \phi(R,t)$ in m^{-4} denotes the number density distribution of precipitates with radius R and at time t. v is the growth rate describing the growing and dissolving of precipitates, while S is a source function describing the nucleating of precipitates.

While the mathematical approach has changed, the physical model is the same as the model by Zurob et al. (2002): the nucleation and growth rate were adopted from this model, with modifications to remove some drawbacks of the model. Some of these drawbacks were eliminated by extending the model and some improvements are recommended for future work. The two main drawbacks that were eliminated from the model in this thesis were the lack of influence of all elements in the system and the lack of competition between different nucleation sites and between different precipitate compositions. The complexity belonging to the first drawback was captured by introducing a multi-component model. In this extension all elements in the system influence the nucleation and growth of the precipitates, even when the elements do not participate in the precipitate. This effect was also not taken into account in the basic KWN model described by Robson (2014).

The complexity belonging to the second drawback, was captured by introducing a multi-precipitate model. This multi-precipitate model consists of two parts: competition between different precipitate compositions and competition between different nucleation sites. Competition between different precipitate compositions exists because most steel alloys contain many alloying elements, and therefore different precipitates can occur simultaneously, for instance, $Nb(C,N)$, AlN and MnS. Also precipitates may nucleate at various nucleation sites. In this thesis, we limit ourselves to nucleation on dislocations, on grain boundaries and homogeneous nucleation. Nucleation on other precipitates or inclusions is not considered here, because the area available for nucleation is much lower than the grain boundary area. Interphase nucleation during austenite to ferrite transformation requires the introduction of special models and is recommended for future work.
For the multi-precipitate extension we get an additional partial differential equation for each complexity (precipitate composition or side) that is added. The additional PDEs are of exactly the same form, but (sometimes) with different parameters. Since the partial differential equation (PDE) is non-linear in ϕ, we have to find an approximation of the solution using a numerical method. We introduced multiple PDE solvers, and

described why we choose the finite volume method combined with the Backward Euler method and Picard's fixed point iteration. Thereafter, we gave an analysis of the resulting (discretised) system and an overview of the various algorithms used. During the implementation computational issues arose, but after adjustments in the implementation these issues were solved. Also, increasing the speed of the computation.

Various combinations of precipitate compositions and nucleation sites have been simulated to see the effect on the results and the performance of the implementation. Temperature curves and dynamic dislocation densities were introduced to show the flexibility of the model. All results of the simulations could be qualitatively interpreted. Also, the model is quite robust, but the computation time can increase drastically when more complexities are introduced (like a changing temperature, multiple precipitate compositions or multiple nucleation sites). This is mainly because of the non-linear equations in the model, like the critical radius and the growth rate, that have to be solved in every time step during the simulation. To get correct results, the accuracy of the model had to be increased, leading to an even higher computation time.

12

Future work

For this work a lot of useful knowledge was gathered on the nucleation and growth of precipitates on dislocations and other nucleation sites. Using this knowledge a model was developed and tested. The work that was done in this thesis was a step in the right direction, but there is still a lot of work ahead to develop a real-time model including all aspects of precipitation. In this chapter, some concrete examples are given of improvements to the model given in this thesis. Not just by improving the current model, but also by extending it in various ways.

12.1. Improvements current model

As described in Chapter 3 and in the literature study prior to this thesis (Vonk (2016)), the precipitation model by Zurob et al. (2002) needed improvement on multiple aspects. The most essential improvement was done in this thesis: the introduction of the distribution approach over the mean radius approach. However, some other improvements still need to be performed.

As stated before, the nucleation and growth rate were adopted from the model by Zurob et al. (2002). Zurob et al. (2002) used approximations for various parameters in the nucleation rate in the mean radius approach, like the Zeldovich factor Z and the maximum number of available sites N_{total}. The approximations in nucleation rate which were used by Zurob et al. (2002), were also applied in the first version of our model:

$$I(t) = (N_{total} - N)\left(\frac{D_{pipe,Nb} x^M_{Nb}}{a^2}\right)\exp\left(\frac{-\Delta G^*}{k_B T}\right) \tag{3.8}$$

One of the approximations in this nucleation rate was improved in Chapter 4: the Zeldovich factor. It was changed to a multi-component and nucleation site dependent parameter. However, introduction of these extensions did not lead to large differences with the model without these extensions. Other approximations were not yet analysed and/ or improved, of which some examples of these approximations are given below.

- First, N_{total}, is the maximum number of available sites, and it involves an adjustable factor F which has no direct physical meaning. Kranendonk (2005) found a value for F of about three orders of magnitude lower than the expected value of around 1, if only dislocations are considered as nucleation sites. For nucleation at other sites we have also incorporated a fitting parameter for the maximum number of available nucleation sites. To find the correct values for the fitting parameters for nucleation at other sites, we need enough (and correct) experimental data, which is not yet available.
- A second approximation is that of the chemical driving force Δg_v in the activation energy ΔG^*. This approximation influences the value of the fitting parameter F, but there is still a scientific debate around the correct formulation of the chemical driving force. A different way of describing this chemical driving force was used by Den Ouden et al. (2013). The approximation for the free energy release due to the reduction of the elastic energy associated with precipitation on dislocations in the activation energy is also questioned, since in the approximation in the present model, it is assumed that the precipitate on dislocation is spherical, whereas studies show a more spheroidal or needle like shape of the precipitate on this site.

There also exists several descriptions of the nucleation rate. Robson (2014) for example, assumes a different time-dependent nucleation rate, which includes an incubation time for precipitation. All above approximations and the choice of nucleation rate could influence the final results. Fitting the results to experimental data could then lead to a different value of the fitting parameter, but it is yet unknown in what order and trend it might change. Further research on this subject is therefore needed.

As stated in the concluding remarks the computation time can increase drastically when more complexities are introduced. For simulations with simple time-temperature schemes and without dislocation dynamics, this might not be a large problem. However, when one would like to use this model as a real-time simulation of what is happening during the steel making process, lowering the computation time becomes an increasing necessity. Since the calculation of the growth rate is the most time-consuming, this would be a good focus point to start with.

12.2. Extensions current model

The current model could be further improved, but also a wide range of extensions to the model is possible, of which the most important are given below.

- Since nucleation on dislocations is of great importance, it is necessary to take the evolution of the dislocation density also into account. In this thesis, we investigated the influence of a user-defined dynamic dislocation density, but a more realistic time evolution of the dislocation density is described by the recrystallisation and recovery models by Zurob et al. (2002). These recrystallisation and recovery models have to be coupled to the (distribution based) precipitation model.

- A serious assumption in both the mean radius as well in the distribution approach is the spherical shape of the precipitates. Since the precipitates grow at different nucleation sites, one would expect the shape of the precipitate to adjust to the site. For precipitates at dislocations for example, we expect spheroidal shaped precipitates. Developing algorithms for the dynamics of non-spherical precipitate evolution, which keeps the computation time within reasonable values, is a nice challenge.

- The simulations in this thesis are done in austenite, but some applications ask for simulations in ferrite. The model as described in this thesis is, in principle, applicable to both phases, and therefore this extension will only require the adjustment of some parameters. A more complex extension is the implementation of phase-transformations. In this way a more realistic temperature curve can be used, which for example, involves a phase-transformation from ferrite to austenite or vice versa (interphase precipitation).

- The model described in this thesis incorporated various precipitates compositions, of which one was a complex precipitate ($Nb(C,N)$). However, the kinetics of this complex precipitate were specified for this specific precipitate only. A good extension would be to develop a more generic description of the kinetics of complex precipitates, which can then be incorporated in the current model. This generic description of the kinetics of complex precipitates could than be extended with a temperature dependent stoichiometric ratio.

- Besides the three nucleation sites discussed in this thesis, nucleation on dislocations, nucleation on grain boundaries and homogeneous nucleation, precipitates can also nucleate at other (larger) precipitates and inclusions. Even though, we believe the three that were chosen are the most important sites where nucleation takes place, it would be nice to complete the model with even more nucleation sites, like nucleation on other precipitates and/or inclusions, and interphase nucleation.

12.3. Parameters and model validation

The model developed during this thesis is a good and solid basis for the simulation of precipitation at various nucleation sites. However, to use this model as a predictor or even real-time simulator, the model needs validation with experimental data. The experimental data currently available is very limited. Without proper fitting of the model to experimental data, it is hard to verify and use the obtained results for prediction.
The results obtained are greatly influenced by the choice of the fitting parameter F, which can only be correctly chosen when fitted to experimental data. Using a part of newly generated experimental data to fit the

model using this fitting parameter and using a second part to verify the forecasts of the model, would make the model more reliable and good to use.
Also other parameters in the model were approximated or based on very little experimental data. The best examples of this are the diffusion coefficients, for which we found very little information in the literature. Executing experiments on this subject would largely increase the reliability of the model and its simulations.

A

Derivation of the Zeldovich factor

As a definition for the Zeldovich factor we use that of Russell (1980):

$$Z = \sqrt{\frac{-1}{2\pi k_B T}\left(\frac{d^2}{dN^2}(\Delta G)\right)\Big|_{R^*}}. \tag{A.1}$$

We start with the derivative to the number density N:

$$\frac{d^2}{dN^2} = \left(\frac{d}{dR}\frac{dR}{dN}\right)^2, \tag{A.2}$$

where the derivative of the mean radius R to the number density N is found using the volume of the precipitate. In general, the volume of a precipitate is defined as

$$V = \frac{4}{3}\pi R^3, \tag{A.3}$$

or using the atomic volume of the precipitate as

$$V = v_{at} N. \tag{A.4}$$

Combining these definitions gives

$$R = \left(\frac{3}{4\pi} v_{at} N\right)^{1/3} \tag{A.5}$$

Starting with the first derivative to N, we find

$$\frac{d}{dN} = \frac{d}{dR}\cdot\frac{dR}{dN}, \tag{A.6}$$

$$= \frac{d}{dR}\cdot\frac{d}{dN}\left(\frac{3}{4\pi} v_{at} N\right)^{1/3}, \tag{A.7}$$

$$= \frac{d}{dR}\cdot\frac{1}{3}\left(\frac{3}{4\pi} v_{at} N\right)^{-2/3}\frac{3 v_{at}}{4\pi}, \tag{A.8}$$

$$= \frac{d}{dR}\cdot\left(\frac{3}{4\pi} v_{at} N\right)^{-2/3}\frac{v_{at}}{4\pi}. \tag{A.9}$$

Now substituting Equations (A.4) and (A.3) in this equation yields

$$\frac{d}{dN} = \frac{d}{dR}\cdot\left(\frac{3}{4\pi}\frac{4\pi}{3}R^3\right)^{-2/3}\frac{v_{at}}{4\pi}, \tag{A.10}$$

$$= \frac{d}{dR}\cdot R^{-2}\frac{v_{at}}{4\pi}, \tag{A.11}$$

which means for the second derivative to N we find

$$\frac{d^2}{dN^2} = \left(\frac{d}{dR}\cdot R^{-2}\frac{v_{at}}{4\pi}\right)^2, \tag{A.12}$$

$$= R^{-4}\frac{v_{at}^2}{16\pi^2}\frac{d^2}{dR^2}. \tag{A.13}$$

Substituting this result into the definition of the Zeldovich factor gives

$$Z = \sqrt{\frac{-1}{2\pi k_B T}\frac{v_{at}^2}{16\pi^2(R^*)^4}\left(\frac{d^2}{dR^2}(\Delta G)\right)\Big|_{R^*}}, \tag{A.14}$$

$$= \frac{v_{at}}{4\pi\sqrt{k_B T}}\sqrt{\frac{-1}{2\pi}\left(\frac{d^2}{dR^2}(\Delta G)\right)\Big|_{R^*}}\left(\frac{1}{R^*}\right)^2, \tag{A.15}$$

as a more generic and more applicable definition of the Zeldovich factor.

For each nucleation site we will use this definition to find the correct equation for the Zeldovich factor.

A.1. Dislocations

$$Z = \sqrt{\frac{-1}{2\pi k_B T}\left(\frac{d^2}{dN^2}(\Delta G)\right)\Big|_{R^*}}, \tag{A.16a}$$

$$= \frac{v_{at}}{4\pi\sqrt{k_B T}}\sqrt{\frac{-1}{2\pi}\left(\frac{d^2}{dR^2}(\Delta G)\right)\Big|_{R^*}}\left(\frac{1}{R^*}\right)^2, \tag{A.16b}$$

$$= \frac{v_{at}}{4\pi\sqrt{k_B T}}\sqrt{\frac{-1}{2\pi}\left(8\pi R^*\Delta g_v + 8\pi\gamma - \frac{\mu b^2}{2\pi(1-\nu)R^*}\right)}\left(\frac{1}{R^*}\right)^2, \tag{A.16c}$$

$$= \frac{v_{at}}{2\pi\sqrt{k_B T}}\sqrt{-R^*\Delta g_v - \gamma + \frac{\mu b^2}{16\pi^2(1-\nu)R^*}}\left(\frac{1}{R^*}\right)^2. \tag{A.16d}$$

A.2. Grain boundaries

$$Z = \sqrt{\frac{-1}{2\pi k_B T}\left(\frac{d^2}{dN^2}(\Delta G)\right)\Big|_{R^*}}, \tag{A.17a}$$

$$= \frac{v_{at}}{4\pi\sqrt{k_B T}}\sqrt{\frac{-1}{2\pi}\left(\frac{d^2}{dR^2}(\Delta G)\right)\Big|_{R^*}}\left(\frac{1}{R^*}\right)^2, \tag{A.17b}$$

$$= \frac{v_{at}}{4\pi\sqrt{k_B T}}\sqrt{\frac{-1}{2\pi}(8\pi R^*\Delta g_v + 8\pi\gamma - 2\pi\gamma_{gb})}\left(\frac{1}{R^*}\right)^2, \tag{A.17c}$$

$$= \frac{v_{at}}{4\pi\sqrt{k_B T}}\sqrt{\gamma_{gb} - 4\gamma - 4R^*\Delta g_v}\left(\frac{1}{R^*}\right)^2, \tag{A.17d}$$

$$= \frac{v_{at}}{2\pi\sqrt{k_B T}}\sqrt{\frac{1}{4}\gamma_{gb} - \gamma - R^*\Delta g_v}\left(\frac{1}{R^*}\right)^2, \tag{A.17e}$$

$$= \frac{v_{at}}{2\pi\sqrt{k_B T}}\sqrt{\gamma - \frac{1}{4}\gamma_{gb}}\left(\frac{1}{R^*}\right)^2. \tag{A.17f}$$

A.3. Homogeneous

$$Z = \sqrt{\frac{-1}{2\pi k_B T}\left(\frac{d^2}{dN^2}(\Delta G)\right)\Big|_{R^*}}, \tag{A.18a}$$

$$= \frac{v_{at}}{4\pi\sqrt{k_B T}}\sqrt{\frac{-1}{2\pi}\left(\frac{d^2}{dR^2}(\Delta G)\right)\Big|_{R^*}}\left(\frac{1}{R^*}\right)^2, \tag{A.18b}$$

$$= \frac{v_{at}}{4\pi\sqrt{k_B T}}\sqrt{\frac{-1}{2\pi}(-8\pi\gamma)}\left(\frac{1}{R^*}\right)^2, \tag{A.18c}$$

$$= \frac{v_{at}}{4\pi\sqrt{k_B T}}\sqrt{4\gamma}\left(\frac{1}{R^*}\right)^2, \tag{A.18d}$$

$$= \frac{v_{at}}{2\pi\sqrt{k_B T}}\sqrt{\gamma}\left(\frac{1}{R^*}\right)^2. \tag{A.18e}$$

B

Standard settings as used in the simulation for *NbCN* precipitates

Solubility products

$$K(NbC) = 10^{3.42-\frac{7900}{T}}$$
$$K(NbN) = 10^{2.80-\frac{8500}{T}}$$

Mass densities

$$\rho_{NbCN} = \frac{M_{Nb} + xM_C + (1-x)M_N}{v_{m,NbCN}} \quad \mathrm{g/m^3}$$
$$\rho_{aus} = (8283.8 - 0.5785 \cdot T) \cdot 1000 \quad \mathrm{g/m^3}$$

Lattice constant

$$a = (0.36306 + 0.078x_c)(1 + (24.9 - 50x_c)(T - 1000) \times 10^{-6}) \times 10^{-9} \quad \mathrm{m}$$

Molar volumes

$$v_{m,NbCN} = xv_{m,NbC} + (1-x)v_{m,NbN} \quad \mathrm{m^3/mol}$$
$$v_{m,aus} = \frac{1}{4}N_a a^3 \quad \mathrm{m^3/mol}$$

Interface energy

$$\gamma = 2.5 \times 10^{-5}(T_{sol} - T)^{1.5} + 0.375 \quad \mathrm{J/m^2}$$

Shear modulus

$$\mu = 81 \times 10^9 \left(1 - 0.91\frac{T - 300}{1810}\right) \quad \mathrm{Pa}$$

Diffusion coefficients

$$D_{pipe} = 4.1 \times 10^{-4} \exp\left(\frac{-172500}{R_g T}\right) \quad \mathrm{m^2/sec}$$
$$D_{bulk} = 0.83 \times 10^{-4} \exp\left(\frac{-266500}{R_g T}\right) \quad \mathrm{m^2/sec}$$

In the mean radius approach, we use the following coarsening function[1]:

$$F_c = 1 - \mathrm{erf}\left(4\left(\frac{R}{R_0}\ln\left(\frac{C_{Nb}^M}{C_{Nb}^{Eq}}\right) - 1\right)\right) \quad \text{(with restrictions from Kranendonk (2005)).}$$

[1] For more details on the coarsening function we refer to Vonk (2016).

Bibliography

Academic Resource Center. Materials Deformation, 2015. URL https://web.iit.edu/sites/web/files/departments/academic-affairs/Academic%20Resource%20Center/pdfs/Material_Deformations_Workshop.pdf. Presentation, Last accessed 4 February 2016.

Cdan. Images - Material Science, own work, 2015. URL https://commons.wikimedia.org/wiki/User:Cdang/Gallerie_d%27images/Materials_sciences?uselang=nl. Last accessed 4 February 2016.

L.M.L. Cheng. *Study of the kinetics of precipitation, dissolution and coarsening of aluminium nitride in low carbon steels*. PhD thesis, The University of British Columbia, 2003.

D. Den Ouden. *Mathematical Modelling of Nucleating and Growing Precipitates*. PhD thesis, Delft University of Technology, 2015.

D. Den Ouden, L. Zhao, J. Sietsma, and F.J. Vermolen. Modelling precipitate nucleation and growth with multiple precipitate species under isothermal conditions: Formulation and analysis. *Computation Materials Science*, 79:933–943, 2013.

A. Deschamps and Y. Brechet. Influence of predeformation and ageing of an Al-Zn-Mg alloy - II. Modeling of precipitation kinetics and yield stress. *Acta Materialia*, 47:293–305, 1999. Pergamon.

R.C. Hudd, A. Jones, and M.N. Kale. A method for calculating the solubility and composition of carbonitride precipitates in steel with particular reference to niobium carbonitride. *Journal of The Iron and Steel Institute*, pages 121–125, February 1971.

D. Hull and D.J. Bacon. *Introduction to Dislocations*. Butterworth-Heinemann, Linacre House, Jordan Hill, Oxford OX2 8DP, England, 2001.

R. Kampmann and R. Wagner. *Materials Science and Technology - A Comprehensive Treatment*, volume 5. VCH, Weinheim, Germany, 1991.

I. Kaur, W. Gust, and L. Kozma. *Handbook of Grain and Interphase Boundary Diffusion Data*. Ziegler Press, University of Stuttgart, 1989.

W. Kranendonk. Modelling Strain Induced Precipitation: the Zurob Model, 2005. Tata Steel R&D, Reference Source number: 114496.

J. Kucera and K. Stransky. Diffusion in iron, iron solid solutions and steels. Review paper, 1981. Institute of Physical Metallurgy, Czechoslovak Academy of Sciences, Brno.

Learning Geology. Elementary concepts of thermodynamics, 2015. URL http://geologylearn.blogspot.nl/2015/11/elementary-concepts-of-thermodynamics.html. Last accessed 4 February 2016.

A.D. LeClaire and G. Neumann. *Diffusion in Solid Metals and Alloys*. SpringerMaterials, 1990.

R.J. Leveque. *Finite Volume Methods for Hyperbolic Problems*. Cambridge University Press, 32 Avenue of the Americas, New York NY 10013-2473, USA, 2007.

P Maugis and M. Gouné. Kinetics of vanadium carbonitride precipitation in steel: A computer model. *Elsevier Science*, 53(12):3359–3367, 2005.

G.E. Murch. Ferrite and Austenite: Diffusion, Bulk and Interfacial. *Elsevier Science*, pages 3009–3012, 2001.

Jitin Nair. What is an intuitive explanation of the iron-carbon phase diagram?, 2015. URL https://www.quora.com/What-is-an-intuitive-explanation-of-the-iron-carbon-phase-diagram. Last accessed 4 February 2016.

A.S. Pandit. *Theory of the Pearlite Transformation in Steels*. PhD thesis, University of Cambridge, 2011.

M. Perez, M. Dumont, and D. Acevedo-Reyes. Implementation of classical nucleation and growth theories for precipitation. *Acta Materialia*, 56:2119–2132, 2008.

D.A. Porter and K.E. Easterling. *Phase Transformations in Metals and Alloys*. Chapman & Hall, 2-6 Boundary Row, London SE1 8HN, England, 1981.

M. Rendy Yusman. Hot Working of Metals, 2011. URL http://sainsmechanical.blogspot.nl/2011/12/hot-working-of-metals.html. Last accessed 2 March 2016.

P. Rey. P. Rey's Teaching Portofolio, 2015. URL http://www.geosci.usyd.edu.au/users/prey/Teaching/Teach.html. Last accessed 4 February 2016.

J.D. Robson. Modelling the evolution of particle size distribution during nucleation, growth and coarsening. *Materials Science and Technology*, 20:441–448, 2014.

I.G. Rodionova, Kazankov A.Yu., M.V. Rodionova, and A.I. Kryukova. Evaluation of the possibility of retarding steel recrystallization during hot rolling with precipitation of manganese sulfide particles. *Metallurgist*, 59(11-12):1101–1105, 2016.

K.C. Russell. Nucleation in solids: The induction and steady state effects. *Advances in Colloid and Interface Science*, 13(3-4):205–318, 1980.

K.P. Shah. The Hand Book on Mechanical Maintenance - Crystallization, 2012. URL http://practicalmaintenance.net/. Last accessed 4 February 2016.

J. Van Kan, A. Segal, and F. Vermolen. *Numerical Methods in Scientific Computing*. VSSD, Leeghwaterstraat 42, 2628 CA Delft, The Netherlands, 2014.

S.M. Vonk. *Precipitates on Dislocations*. Literature study. Delft University of Technology, 2016.

C. Vuik, F. Vermolen, M.B. Van Gijzen, and M.J. Vuik. *Numerical methods for ordinary differential equations*. VSSD, Leeghwaterstraat 42, 2628 CA Delft, The Netherlands, 2015.

Wikipedia. Block matrix, 2015a. URL https://en.wikipedia.org/wiki/Block_matrix. Last accessed 6 April 2016.

Wikipedia. Ridders' method, 2015b. URL https://en.wikipedia.org/wiki/Ridders%27_method. Last accessed 17 May 2016.

Wikipedia. Steelmaking, 2015c. URL https://en.wikipedia.org/wiki/Steelmaking. Last accessed 17 December 2015.

Wikipedia. Burgers vector, 2016a. URL https://en.wikipedia.org/wiki/Burgers_vector. Last accessed 4 February 2016.

Wikipedia. Brent's method, 2016b. URL https://en.wikipedia.org/wiki/Brent%27s_method. Last accessed 17 May 2016.

Wikipedia. Allotropes of iron, 2016c. URL https://en.wikipedia.org/wiki/Allotropes_of_iron. Last accessed 4 February 2016.

Wikipedia. Partial differential equation, 2016d. URL https://en.wikipedia.org/wiki/Partial_differential_equation. Last accessed 22 June 2016.

Wikipedia. Basic oxygen steelmaking, 2016e. URL https://en.wikipedia.org/wiki/Basic_oxygen_steelmaking. Last accessed 4 February 2016.

H.S. Zurob. *Effects op precipitation, recovery and recrystallization on the microstructural evolution of microalloyed austenite*. PhD thesis, McMaster University, 2003.

H.S. Zurob, C.R. Hutchinson, Y. Brechet, and G. Purdy. Modeling recrystallization of microalloyed austenite: effect of coupling recovery, precipitation and recrystallization. *Acta Materialia*, 50:3075–3092, 2002. Pergamon.

Nomenclature

Numerical symbols

α	Parameter used in the adaptive time step algorithm	
β	Parameter used in the adaptive time step algorithm	
ΔR_i	Size of radius cell i	m
Δt	Time step	s
Δt_{start}	Initial time step	s
ϕ_n	Short for $\phi(t_n)$	$1/m^4$
τ	Approximation of the truncation error	
A_n	Short for $A(\phi_n, t_n)$	
R_i	Center of radius cell i	m
Re_i	Edge of radius cell i	m
S_n	Short for $S(\phi_n, t_n)$	$1/^3s$
t_n	n-th discrete time	s
t_{end}	End time	s
t_{start}	Starting time	s
TOL	Tolerance level for the Picard iteration	

Precipitation related symbols

α_n	Numerical factor, accounting for the fact that nucleated precipitates can grow only if their radius is slightly larger than the nucleation radius	
β^*	Rate of atomic attachment to a growing precipitate	
ΔG	Free energy of precipitate formation	J
ΔG^*	Activation energy for the nucleation of a precipitate (on a dislocation)	J
ΔG_n	Free energy release due to nucleation on a specific site, like dislocations (ΔG_d) and grain boundaries (ΔG_{gb})	J
Δg_v	Driving force for precipitation	J/m^3
δ_{gb}	Thickness of a grain	m
γ	Interfacial energy between precipitate and matrix	J/m^2
γ_{gb}	Interfacial energy of the grain boundary	J/m^2
μ	Shear modulus of steel	Pa
ν	Poisson ratio	
$\phi(R,t)$	Number density distribution of precipitates with radius R and at time t	$1/m^4$

Ψ	Set of all elements in the system.	
ρ	Dislocation density	$1/m^2$
ρ_{aus}	Mass density of austenite	g/m^3
τ	Incubation time for heterogeneous nucleation	s
Θ	Set of all precipitate types in the system.	
a	Lattice constant of austenite	m
b	Burgers vector	m
C_X^0	Initial concentration of element X in the matrix	mol/m^3
C_X^M	Concentration of element X in the matrix	mol/m^3
C_X^P	Concentration of element X in precipitates	mol/m^3
C_X^R	Equilibrium concentration of element X with average radius R, also called interface concentration	mol/m^3
$C_X^{R27/23}$	Equilibrium concentration of element X with average radius $\frac{27}{23}R$	
C_X^{Eq}	Equilibrium concentration of element X in the matrix at infinite time	mol/m^3
D_0	Maximum diffusion coefficient (at infinite temperature)	m^2/s
$D_{bulk,X}$	Diffusion coefficient in the bulk of element X	m^2/s
$D_{eff,X}$	Effective diffusion coefficient of element X	m^2/s
$D_{pipe,X}$	Diffusion coefficient in the pipe of element X	m^2/s
f_v	Volume fraction	
F_{site}	Fitting parameter (smaller than 1) for a specific nucleation site	
$I(t)$	Nucleation rate	$1/m^3s$
k_B	Boltzmann constant	J/K
$K_p(T)$	Solubility product of precipitate type p at temperature T	
M_X	Molar weight of element X	g/mol
$N(t)$	Number density of precipitates as a function of time	$1/m^3$
N_{total}	Maximum number density of precipitation per unit volume	$1/m^3$
Q_d	Activation energy for diffusion	J/mol
$\tilde{R}$	Adjusted radius used to avoid numerical instabilities	m
$\bar{R}(t)$	Mean radius of precipitates over time	m
R^*	Critical precipitate nucleus radius for heterogeneous nucleation at a dislocation	m
R_h^*	Critical precipitate nucleus radius for homogeneous nucleation	m
R_g	Gas constant	J/(K mol)
R_{grain}	The radius of a grain	m
R_{k_BT}	Adjusted critical radius with a corresponding activation energy k_BT lower than the activation energy beloning to the real critical radius	m

$S(t)$	Source function describing the nucleation of precipitates	$1/^3$s
T	Temperature	K
t	Time	s
T_{sol}	Solvus temperature	K
v	Growth rate m/s	
v_{at}	Atomic volume of precipitate type p	m^3
$v_{m,p}$	Molar volume of precipitate type p	m^3/mol
$wt\%X^0$	Initial weight percentage of element X	
$wt\%X^M$	Weight percentage of element X in the matrix	
$wt\%X^{Eq}$	Equilibrium weight percentage of element X in the matrix at infinite time	
$wt\%X^R$	Equilibrium weight percentage of element X with average radius R, also called interface weight percentage	
x	Stoichiometric ratio of carbon and nitrogen in the precipitate niobiumcarbonitride (NbC_xN_{1-x}) at equilibrium	
x_X^M	Molar fraction of X in the matrix	
Z	Zeldovich factor	